1-1-2008

Fourier-Transform Microwave Spectroscopy Of Cyclopropylmethylgermane And Van Der Waals Complexes Of Fluorinated Methanes

Michal M. Serafin
Eastern Illinois University

FOURIER-TRANSFORM MICROWAVE SPECTROSCOPY OF CYCLOPROPYLMETHYLGERMANE AND VAN DER WAALS COMPLEXES OF FLUORINATED METHANES

SERAFIN

THESIS REPRODUCTION CERTIFICATE

TO: Graduate Degree Candidates (who have written formal theses)

SUBJECT: Permission to Reproduce Theses

The University Library is receiving a number of request from other institutions asking permission to reproduce dissertations for inclusion in their library holdings. Although no copyright laws are involved, we feel that professional courtesy demands that permission be obtained from the author before we allow these to be copied.

PLEASE SIGN ONE OF THE FOLLOWING STATEMENTS:

Booth Library of Eastern Illinois University has my permission to lend my thesis to a reputable college or university for the purpose of copying it for inclusion in that institution's library or research holdings.

Michael Scanlon 05-22-08

Author's Signature Date

I respectfully request Booth Library of Eastern Illinois University **NOT** allow my thesis to be reproduced because:

_____

_____

_____

_____ _____

Author's Signature Date

This form must be submitted in duplicate.

FOURIER-TRANSFORM MICROWAVE SPECTROSCOPY OF CYCLOPROPYLMETHYLGERMANE AND VAN DER WAALS COMPLEXES OF FLUORINATED METHANES

BY

Michal M. Serafin

This thesis has been read and approved by each of the committee members:

Sean A Peebles — 5/15/08

Dr. Sean A. Peebles — Date

Barbara Lawrence — 5-15-08

Dr. Barbara A. Lawrence — Date

Mark E. McGuire — 5-15-08

Dr. Mark E. McGuire — Date

[signature] — 5-15-08

Dr. Craig A. Wheeler — Date

FOURIER-TRANSFORM MICROWAVE SPECTROSCOPY OF CYCLOPROPYLMETHYLGERMANE AND VAN DER WAALS COMPLEXES OF FLUORINATED METHANES

Abstract

Background theory and instrumentation utilized in the Fourier–transform microwave spectroscopy technique is first introduced followed by the structural and dynamic determination of cyclopropylmethylgermane and two weakly bound van der Waals complexes (difluoromethane–OCS, and fluoromethane–OCS). The minimum energy configuration has been determined for cyclopropylmethylgermane molecule, which has been shown to be the *gauche* configuration. Internal rotation parameters have been obtained from the rotational spectra of cyclopropylmethylgermane. The rotational spectra have been acquired for difluoromethane–carbonyl sulfide and fluoromethane–carbonyl sulfide and experimental structures have been determined for these weakly bound complexes. Evidence for a very low barrier to internal rotation has been observed in the fluoromethane–carbonyl sulfide complex. A computational study of weakly bound complexes containing fluoromethanes bound to carbonyl sulfide or carbon dioxide, has been performed to determine a systematic improvability of theoretical models in the prediction of structural and dynamic parameters of four such complexes, namely; HCF_3-OCS, H_2CF_2-OCS, H_3CF-OCS, and HCF_3-CO_2. Variation of both level of theory (MP2 and CCD) and basis sets has been carried out to explore the structural parameters and energetics of the weakly bound complexes.

Dedicated to my parents Jerzy and Lilla Serafin

Acknowledgements

Research Advisor, Dr. Sean A. Peebles

Thesis Committee, Dr. Barbara A. Lawrence, Dr. Mark E. McGuire, and Dr. Kraig A. Wheeler

Sidney Steele Summer Research Support

Eastern Illinois University Chemistry Department Faculty

Table of Contents

List of Figures

List of Tables

Chapter 1

Introduction

1.1. Theory of Microwave Spectroscopy

Fourier-transform microwave (FTMW) spectroscopy[1] is a technique that examines the nature of molecules in the gas phase in a near collision-free environment and determines the rotational spectra of the species of interest. The radiation sources utilized in this technique are phase-coherent oscillators which provide very narrow frequency bands. These are tunable frequency bands that provide energy for the excitation of rotational transitions. The nature of the technique (discussed in detail in the Instrumentation chapter) allows for extremely high resolution in microwave spectra, with the additional benefit of a tunable source, essentially monochromatic, that allows for scanning of large frequency regions. The instrument employed is the Fourier-transform microwave spectrometer that has a vacuum chamber and utilizes a pulsed supersonic jet expansion to adiabatically cool the gas sample into a ground vibrational state and lower rotational levels. In the supersonic expansion weak van der Waals complexes can be generated and the rotational spectra analyzed to obtain the rotational constants. The experimental technique does require a theoretical component which is performed with *ab initio* calculations. *Ab initio* calculations provide lowest energy structures from which theoretical rotational constants are obtained. A rigid rotor model is then used to predict the rotational energy transitions for the system of interest and provides a theoretical spectrum from the *ab initio* calculations to guide the experimental search and assignment. Once the rotational spectrum is assigned, each rotational energy transition must fit to within the experimental uncertainty of 4 kHz with the correct set of spectroscopic parameters. Unambiguous determination of molecular geometry and physical parameters obtained from the fitted constants for weak van der Waals complexes is the main objective of the investigations described in this paper.

The microwave region of the electromagnetic spectrum ranges from 30 cm to 0.3 mm wavelengths, consequently existing in the 1-1000GHz frequency range (where a GHz = 10^9 Hz)[2]. The study of van der Waals complexes or very weakly hydrogen-bonded species requires the use of a supersonic jets to stabilize these chemical systems that would not exist at normal temperatures and pressures. The adiabatic cooling effect that stabilizes weakly bound complexes is caused by the expansion of a highly pressurized gas through a nozzle into a vacuum chamber where the sample is then probed by microwave radiation. The technique offers unambiguous determination of species and structure because the experiment is performed in a vacuum chamber, where the structural dynamics can be determined to a high precision without external perturbations to the molecules examined. In other techniques, such as matrix isolation spectroscopy, the molecules are isolated in a rare gas matrix and cooled to very low temperatures. The rare gas molecules have little interaction with the species of interest but the matrix does still slightly perturb structural parameters such as bond lengths or angles, which can be more accurately determined with microwave spectroscopy performed in the gas phase.

To probe any molecular system with microwave spectroscopy, it is necessary that the molecular species of interest have an overall dipole moment. Microwave radiation will exert a torque on the dipole moment, thereby exciting rotational transitions of the molecular system. The free rotation of any molecule or molecular system (and the excitation of rotational transitions) is quantized and described by the quantum number *J*. The quantized rotational energy levels are separated by ΔE that correspond to the microwave quanta $h\nu$, and transition frequencies occur when $h\nu = \Delta E$ (where ν is the frequency). Rotational angular momentum is changed as microwave radiation is absorbed. It is important to have an understanding of the classical expression for rotational motion of a rigid system of particles (rigid rotor model). The

moment of inertia (I) is a key parameter in rotational spectroscopy and is defined as shown in equation 1, where m is the mass of the atom, r is the perpendicular distance from the axis of rotation and the subscript i refers to each atom in the molecule.

(1) $$I = \sum m_i r_i^2$$

Rotational spectra are so sensitive to mass variations that the isotopic substitution of a single atom can dramatically shift the spectrum of the isotopomer from where the normal species exists. In fact, the further an isotopically substituted atom is from the center of mass, the more significant the spectral variations will be due to the mass dependence of the moment of inertia. Since we know the masses of the atoms, structural distances and angles can be very accurately determined for small molecular systems containing less than 15 non-hydrogen atoms. One drawback of this technique is that only small molecular systems can be studied. As the molecular systems get larger (than 15 non-hydrogen atoms) and more complex the spectra will fall outside of the spectral range accessible by our spectrometer (note: FTMW instrument range 4-18 GHz). The three dimensional coordinate system originates at the center of mass for any particular system. Thus, there are three moments of inertia (I_a, I_b, and I_c) - one about each of the a, b, and c principal axes (where any axis is perpendicular to another). The axes are labeled by convention such that:

$$I_a \leq I_b \leq I_c$$

The symmetry elements of a molecular system are also important for locating the principal axes. If all three principal moments of inertia are equal to one another, we classify this system as a spherical top (and I_a=I_b=I_c). When two of the principal moments of inertia are equal to one another, these are classified as symmetric tops. There are two types of symmetric tops, the first

is a prolate symmetric top (where $I_a \neq I_b = I_c$) with the *a*–axis as the symmetry axis; and the second is the oblate symmetric top ($I_a = I_b \neq I_c$) with the *c*–axis as the symmetry axis. If all three moments of inertia are unequal to each other ($I_a \neq I_b \neq I_c$) then the system is classified as an asymmetric top. Thus methane is a spherical top, methyl bromide and benzene are prolate and oblate symmetric tops respectively, and water is an asymmetric top. For any molecular system studied, the convention of lining up the *a*–axis through the center of mass and along the heaviest atoms is used. The structural parameters of most interest are the rotational constants (*A*, *B*, and *C*) which are inversely proportional to the moment of inertia as shown in equation 2, where *h* is Planck's constant, *c* is the speed of light, and *I* is the moment of inertia (*B* is designated as the rotational constant in equation 2)[3].

(2) $$B = \frac{h}{8\pi^2 c I_b}$$

The asymmetry parameter (κ), shown in equation 3 (with A, B, and C being the rotational constants) gives the degree of asymmetry between the limits +1 and –1 which correspond to the oblate and prolate asymmetric tops respectively. The further κ lies from +1 and –1 the more asymmetric the molecule, and the more complex the spectrum will be.

(3) $$\kappa = \frac{2B - A - C}{A - C}$$

Asymmetric tops have two energy levels that arise called the pseudo sublevels, and are designated as the +K and –K energy levels (which are degenerate for symmetric tops) with 2J + 1 distinct rotational sublevels. The King–Hainer–Cross notation[2] for an asymmetric top is as follows: $J_{K_{-1}K_{1}}$. The K_{-1} and K_{+1}, subscripts denote the energy sublevels that occur due to the effects of asymmetry. The changes in J rotational levels for dipole absorption of radiation are

$\Delta J = 0, \pm 1$. The $\Delta J = 0$ transitions are designated as Q–branch transitions, and $\Delta J = +1$ are designated as R–branch transitions. It is possible to observe $\Delta J = -1$ transitions (which are P–branch transitions); however the intensity of P–branch transitions is typically very weak. The restrictions on the pseudo quantum numbers (K_{-1} and K_{+1}) depend on the dipole moment components that lie on each principal axis. Transitions that are excited due to the μ_a dipole component are denoted as *a*–type ($\Delta K_{+1} = \pm 1$), the μ_b dipole component as *b*–type ($\Delta K_{-1}K_{+1} = \pm 1$), and the μ_c dipole component as *c*–type transitions ($\Delta K_{-1} = \pm 1$).

The primary goal of microwave spectroscopy is to assign rotational spectra and obtain physical information from them such as structures, dipole moments, etc. The assignment of linear and symmetric top molecules can be relatively easy compared to the complicated spectra of asymmetric top molecules due to a high degree of order in the former spectra. Since rotational transition intensity is dependent on the size of the dipole moment components theoretical predictions from *ab initio* calculations are used in order to predict spectra. This technique is useful in determining the type of rotational transitions and the regions of the spectrum where they will exist. Useful guides to assigning rotational spectra are spectral line patterns, spectral line intensities, Stark effects, quadrupole coupling, and the rigid rotor model (these will be discussed further below).

1.2. Nuclear Quadrupole Coupling

The high resolution of microwave spectroscopy is capable of distinguishing hyperfine structure arising from nuclear quadrupole coupling[4]. This type of interaction results from a nonspherical distribution of nuclear charge, which can interact with a nonspherical electronic distribution about the quadrupolar nucleus. Spherically symmetric nuclei will not display such

interactions, so the nuclear spin (total nuclear angular momentum) has to be $I > 1/2$. The interaction of the electron distribution puts a twisting torque on the nucleus which causes it to realign its spin moment in the direction of the electric field gradient, which comes from the nonspherical distribution of electronic charge about the nucleus. In gasses the field gradients are not in a fixed orientation, so the quadrupole interaction differs for various rotational states, and this gives rise to hyperfine splittings of rotational transitions. The nuclear spin (I) is coupled to the rotational angular momentum (J) of the species to obtain the resultant quantum number (F) where:

$$F = J + I, J + I - 1, J + I - 2, \ldots, |J - I| \tag{4}$$

and if there is only one coupling nucleus in the species of interest the selection rules followed in rotational spectra are as follows:

$$J \rightarrow J + 1, F \rightarrow F, F \rightarrow F \pm 1, I \rightarrow I \tag{5}$$

Figure 1.1 schematically depicts the selection rules in the energy level diagram with nuclear quadrupole hyperfine structure caused by ^{127}I in ICN for the $J = 8 \leftarrow 7$ rotational transition. The ^{127}I isotope contains a quadrupolar nucleus (I = 5/2), and the transitions relate to the rotational spectrum by following the selection rules in equation 5. However, there are quadrupole components that do not have sufficient intensity and only six F → F + 1 transitions have significant strength. The F → F – 1 transitions are resolvable, but a decrease of intensity for these transitions is observed at higher J rotational levels, and these components do not show up in the spectrum shown in Figure 1.1 because they are 1000 times weaker than the strongest component.

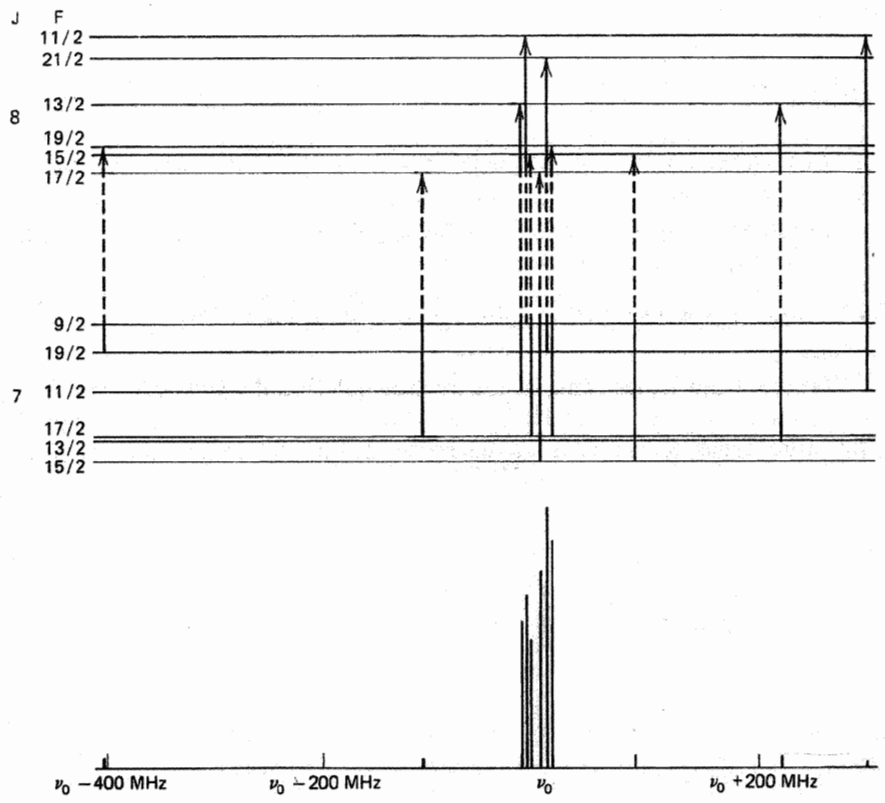

Figure 1.1: Energy level diagram of ^{127}ICN, a linear molecule with a single coupling nucleus. A calculated spectrum displaying quadrupole hyperfine structure for $J = 8 \leftarrow 7$ is displayed.

From the splitting pattern, it is possible to calculate quadrupole coupling constant (χ) utilizing the fact that the quadrupole coupling constant is equal to the product of the charge on a proton (e), the electric field gradient obtained at the coupling nucleus (q), and the electric quadrupole moment of the nucleus (Q). Equation 6 displays the form in which the nuclear quadrupole coupling constants are obtained. It should be noted that the intensity of several transitions due to quadrupole coupling may be too weak to be observed and some may not be fully resolved, but it is not necessary to obtain all quadrupole hyperfine components from rotational spectra in order to determine χ.

(6) $$\chi = eqQ$$

The values of Q have been tabulated for many nuclei determined by atomic beam resonance experiments, so this value can be considered a constant and the determination of q provides information about the electronic environment around the quadrupolar nucleus such as the character of chemical bonds and orbital overlap. While the dipole moment of a molecule depends on the charge distribution about the entire molecule, nuclear quadrupole coupling only depends on the charge distribution about the coupling nucleus, but both molecular parameters provide complementary data.

1.3. Internal Rotation

Other sources that may give rise to complicated spectra are low energy molecular vibrations[5] (these are of particular interest in Chapters 3 and 5). Large amplitude motions such as internal rotation, inversion, or ring puckering can also cause additional spectral splitting to occur in rotational transitions. Internal rotation occurs when two groups are connected by a single bond and the atoms in the two groups rotate relative to one another. Figure 1.2 shows the Newman projection for ethane, which has three equivalent hydrogen atoms on either end of the C–C bond. The methyl groups can rotate relative to one another in order to obtain two conformations, namely staggered and eclipsed. It is important to realize that the rotation of a methyl group will give rise to equivalent orientations of hydrogen atoms. If, for example, one of the carbon atoms in ethane had a fluorine substituent (CH_3CH_2F), then equivalent conformations would not result from internal rotation of the fluoromethyl top. In this case the lowest energy structure of the molecule would have to be determined. If, however, there would be an internal rotation of the second methyl top (only containing hydrogens) relative to the fluorinated top, three equivalent structures could be obtained (one for each of the three hydrogen atoms), and this motion could be considered as a low energy molecular vibration. These low energy vibrational motions cause the

vibrational energy levels to split into two states (labeled the *A* and *E* states). The *A* state can be thought of as the ground vibrational mode, and the *E* state as a torsionally excited vibrational mode. Microwave spectroscopy can be used to assign rotational transitions within these two separate vibrational modes from the splitting of energy levels (which are manifested as doublets in microwave spectra) and determine an energy barrier to these motions.

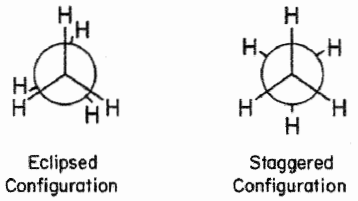

Figure 1.2: The staggered and eclipsed orientations of ethane.

These barriers provide valuable insight into the conformational preference that molecules acquire, and the forces responsible for the arrangement of atoms in low energy structures of molecules. A typical potential energy function for a three fold torsional motion is displayed in Figure 1.3. The *A* and *E* torsional energy levels are labeled as v = 0, 1, and 2. If the barrier height (V_3) is large, there will be a harmonic torsional oscillation of the groups relative to one another about the C–C bond. However, if the barrier is small, there will simply be a free rotation of a methyl top relative to the other about that bond.

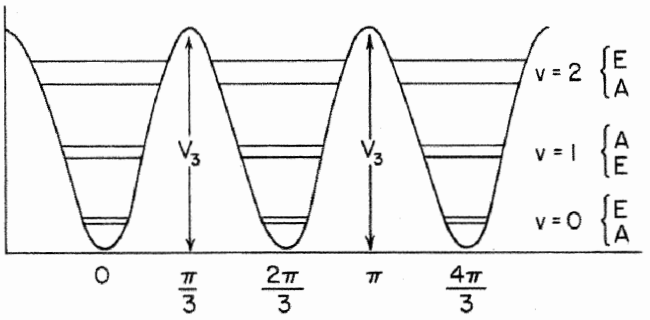

Figure 1.3: The potential function for internal rotation showing the *A* and *E* vibrational states for each respective rotational energy level.

In classical terms, if $V_3 > E$ then the vibrational motion will not have sufficient energy to surpass the barrier and vibrational motion/rotation should not exist. A relatively high barrier may lead to quantum-mechanical tunneling, where the wavefunctions extend through the classically forbidden regions of the potential energy surface, but the width of the barrier will also determine if the wavefunctions have the ability to cross and tunneling to occur. The two limits to consider when developing an energy level scheme would be when the barrier $V_3 = 0$ and when $V_3 = \infty$. If the barrier was infinite then the separate vibrational energy levels (*A* and *E* states) will collapse down to one vibrational mode, and internal rotation would be forbidden. When the torsional energy (E) is higher than V_3 then free rotation will occur (which can be considered as $V_3 = 0$, and $E > 0$). Figure 1.4 displays how the energy levels change with respect to barrier height as it is increased from 0 (free rotation) up to an infinite barrier (where torsional motion is classically forbidden). At the limit where the barrier is infinite, the triply degenerate vibrational modes (displayed in Figure 1.4 as quantum number v) will display a single rotational spectrum. Once the barrier is decreased, the torsional energy levels begin to split two states (*A* and *E* states) which are displayed with the quantum number m in Figure 1.4.

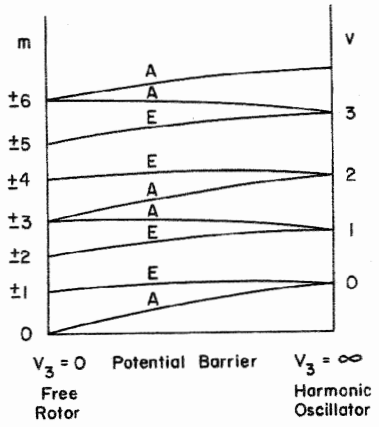

Figure 1.4: Energy levels of an internal rotor and how they correlate as barrier height is increased.

The spectral analysis of a molecule with internal rotation will display a doubling of rotational transitions, shown by the energy sublevels dictated by barrier height (Figure 1.4). This theory will be necessary for the treatment of some of the species described in this thesis, namely, CMG (Chapter 3) and FM–OCS (Chapter 4).

1.4. Stark Effect (Applied Electric Field)

Another important tool for microwave spectroscopists is the Stark effect[6], which is the effect that applied electric fields have on rotational spectra. It is primarily used to obtain very accurate dipole moments of gas phase species. Pure rotational transitions can also be identified (or assigned quantum numbers) with this technique, and this is particularly useful to deconvolute the complex spectra of asymmetric tops, which are the only type of molecular systems discussed in this text. The applied electric field (E) is assumed to have a constant magnitude and a fixed direction. The electric dipole moment components (μ_a, μ_b, and μ_c) are fixed along each of the three axes of inertia for the molecule. The application of an electric field will interact with the dipole moment of the molecular system, perturbing molecular rotation, and consequently perturbing the rotational energy levels. The quantum number (M) describes the rotational energy

sublevels generated by the applied electric field, and 2J+1 M energy sublevels exist for a specific value of J, where J is the rotational quantum number. The microwave spectrometer utilized has a parallel arrangement of the microwave antennae to the electric field, which restricts the selection rule to $\Delta M = 0$. If a perpendicular arrangement of the antenna to the electric field would be used the selection rules would change to $\Delta M = \pm 1$. The first–order Stark effect has an electric field dependence of the first order in the Stark effect Hamiltonian, so for the rotational energy level J = 2, the sublevels would be determined by setting M = –2, –1, 0, +1, and +2 (five total energy sublevels from M = 2J + 1). Since all the species described in this thesis show second order Stark effects, we will no longer consider first order Stark effects. In the second order Stark effect Hamiltonian, the electric field dependence is second order (see eq. 7), and consequently the M energy sublevels become degenerate as $|\pm M|$. For a second order Stark effect, the rotational energy level J = 2 would divide up into three sublevels, namely M = 0, ±1, and ±2. The dipole moment can be measured by plotting $\Delta\upsilon$ (shift in transition frequency) vs. E^2 (electric field squared) equation 7,

(7) $$\Delta\upsilon = (A + BM^2)\,\mu^2 E^2$$

where A and B are the Stark coefficients, and $\Delta\upsilon$ is the frequency shift due to the applied electric field. The linear plot of $\Delta\upsilon$ vs. E^2 will yield a slope that is equal to $(A + BM^2)\,\mu^2$. The Stark coefficients are first calculated from second order perturbation theory, and experimental $(\Delta\upsilon/ E^2)$ data is fit to the equation using least squared fitting techniques to give the experimental dipole moment. A good understanding of the Stark effect and how it affects rotational spectra (splittings that occur from rotational sublevel generation) is a very useful tool in assigning spectral lines. As mentioned above, the number of components that a rotational transition splits into upon interaction with the electric field can help assign it as long as there is sufficient

intensity such that all the components are observed. For example, lets take a look at the second order perturbation for J = 2← 1. The J = 2 rotational level will split into three sublevels (M = 0, ±1, and ±2) and the J = 1 rotational level will split into two sublevels (M = 0 and ±1). The selection rule is ΔM = 0, so there should be two components for a J = 2← 1 transition when it interacts with the applied electric field, namely (J=1 M=0 → J=2 M=0) and (J=1 M=±1 → J=2 M=±1).

Rotational spectroscopy is useful as a real time, rapid technique with extremely high sensitivity. Rare and exotic chemical species can be observed with this technique including gas phase free radicals or hydrogen bound systems. Rotational spectra do however become complicated as molecules get larger or have internal rotors such as methyl tops (–CH_3). As described earlier in this chapter, internal rotation of a subunit will cause the spectrum to be split due to the coupling of the angular momentum to the overall angular momentum of the system. If a nucleus of any atom displays a nuclear quadrupole moment (such as a ^{35}Cl nucleus), the spectrum will display additional splitting, which may further distort the rotational spectrum with hyperfine structure. Even though only relatively small molecular systems may be probed with this technique, the understanding of the structural dynamics, dipole moments, barriers to rotation (of internal rotors), and electric field gradients (of quadrupolar nuclei) may be applied to many branches of chemistry and science.

This thesis will cover the instrumentation utilized in our lab, and four projects for which data has been collected and analyzed. The experimental setup and various techniques used to investigate molecular parameters with microwave spectra will be discussed in the Experimental Technique chapter (Ch. 2). Chapter 3 will discuss the project involving the cyclopropylmethylgermane molecule and details of our use of a new program (XIAM[7]) to solve

internal motion problems. This molecule also has a quadrupolar nucleus and the spectral splitting due to this effect is also summarized in Chapter 3. Some work was also performed to analyze the structure and dipole moments of the additional isotopologues of difluoromethane–carbonyl sulfide dimer, and this is discussed in Chapter 4. A complete analysis of the theoretical structures, spectra, and dipole moment analysis is discussed in Chapter 5 for the fluoromethane–carbonyl sulfide dimer, which is thought to exhibit internal motions. A final project was to perform theoretical studies (*ab initio* calculations) to determine the effects of the levels of theory and basis sets in the improvement of theoretical values in a series of weakly bound complexes. The calculations compared four separate complexes, namely, trifluoromethane–carbonyl sulfide, difluoromethane–carbonyl sulfide, fluoromethane–carbonyl sulfide, and trifluoromethane–carbon dioxide, and are discussed in Chapter 6.

References

[1] A.C. Legon, *Ann. Rev. Phys.* Chem., **1983**, *34*, 275-300

[2] Gordy, W. Cook, R.L. Microwave Molecular Spectra, John Wiley and Sons, **1984**, Ch.1.

[3] Gordy, W. Cook, R.L. Microwave Molecular Spectra, John Wiley and Sons, **1984**, Ch.7.

[4] Gordy, W. Cook, R.L. Microwave Molecular Spectra, John Wiley and Sons, **1984**, Ch.14.

[5] Gordy, W. Cook, R.L. Microwave Molecular Spectra, John Wiley and Sons, **1984**, Ch.12.

[6] Gordy, W. Cook, R.L. Microwave Molecular Spectra, John Wiley and Sons, **1984**, Ch.10.

[7] Hartwig, H. Dreizler, XIAM, version 2.5e, *Z. Naturforsch*, **1996**, *51a*, 923.

Chapter 2

Experimental Technique

2.1. Instrumentation: Balle-Flygare Microwave Spectrometer

The instrument used to perform all the experiments described in this paper, was a Balle-Flygare design Fourier-transform microwave (FTMW) spectrometer. The experiment involves a gas sample introduced via a pulsed nozzle into the Fabry-Pérot cavity which is under vacuum. It is not possible to obtain an absolute vacuum of 0 torr, however, the cavity utilized by the FTMW spectrometer may reach a pressure on the order of 10^{-7} torr. Resonant microwave radiation within the cavity (from 4-18 GHz) is used to probe the adiabatically cooled molecules (which cool to approximately 1-5 K). This adiabatic cooling occurs within the vacuum chamber because the gas sample is at relatively high pressure and rapidly introduced into the vacuum chamber at very low pressure, and due to adiabatic cooling the molecules are able to relax into the vibrational ground state. A mixture of 18% helium and 82% neon is used as a carrier gas (~97-99% of the gas sample) which is used as a third body in the system to carry off excess vibrational or rotational energy from the collision of the molecules of interest. It is also possible to utilize other rare gases or mixtures as carrier gases; for example, a colder expansion is possible if argon is used as the carrier gas due its larger mass and ability to remove more energy from the system. However, there may be disadvantages to using argon as a carrier gas, due to the fact that it is larger and more polarizable and can actually complex efficiently with the molecules of interest, reducing the number that will form the required dimer. Rotational spectra are observed for any stabilized chemical species within the gas expansion by collecting the emitted radiation in the time domain which is Fourier transformed to obtain a spectrum in the frequency domain. The spectrometer is sensitive enough to experimentally determine any given rotational transition to within 4 kHz uncertainty and with a signal to noise ratio of about 30:1 to 80:1 for dimer systems (monomer signals can be observed with S/N ratios to the order of 100:1).

2.2. Fabry-Pérot Cavity

In 1979, T. J. Balle and W. H. Flygare at the University of Illinois in Urbana/Champaign, introduced a new type of microwave spectrometer that combined the Fabry-Pérot cavity with a synchronized microwave pulse with a pulsed supersonic expansion[1]. The main advancement of Balle and Flygare's design for the microwave spectrometer, was to replace a waveguide absorption cell with a Fabry-Pérot cavity which was spacious enough to allow for a supersonic gas expansion that was not possible in the waveguide absorption cell previously used. A supersonic expansion is useful because it is known that a pulse of the gas mixture diluted in an inert gas and supersonically expanded from a nozzle is rich in dimers[2]. The ease of construction of the instrument as well as the high resolution and high sensitivity made the technique useful in assigning rotational spectra of weakly bound complexes[3]. The Fabry-Pérot cavity is a resonant cavity in which microwave radiation forms a standing wave that polarizes the molecules within the gas expansion and also allows for the Fourier-transform analysis of the emitted signal. This type of cavity is used to isolate and positively reinforce certain wavelengths of radiation and can be utilized to isolate almost any wavelength, which makes this cavity useful in various spectroscopic techniques. In 1996, Jens-Uwe Grabow introduced significant improvements to the FTMW circuit design[4], which has been adapted for the instrument described here. Figure 2.1 is a schematic representation of the basic FTMW instrument with an example of sample gas (OCS and HCCH) concentrations. The vacuum chamber contains the Fabry-Pérot cavity, composed of two opposing spherical mirrors which are separated by an adjustable distance to contain a resonant standing wave of microwave radiation.

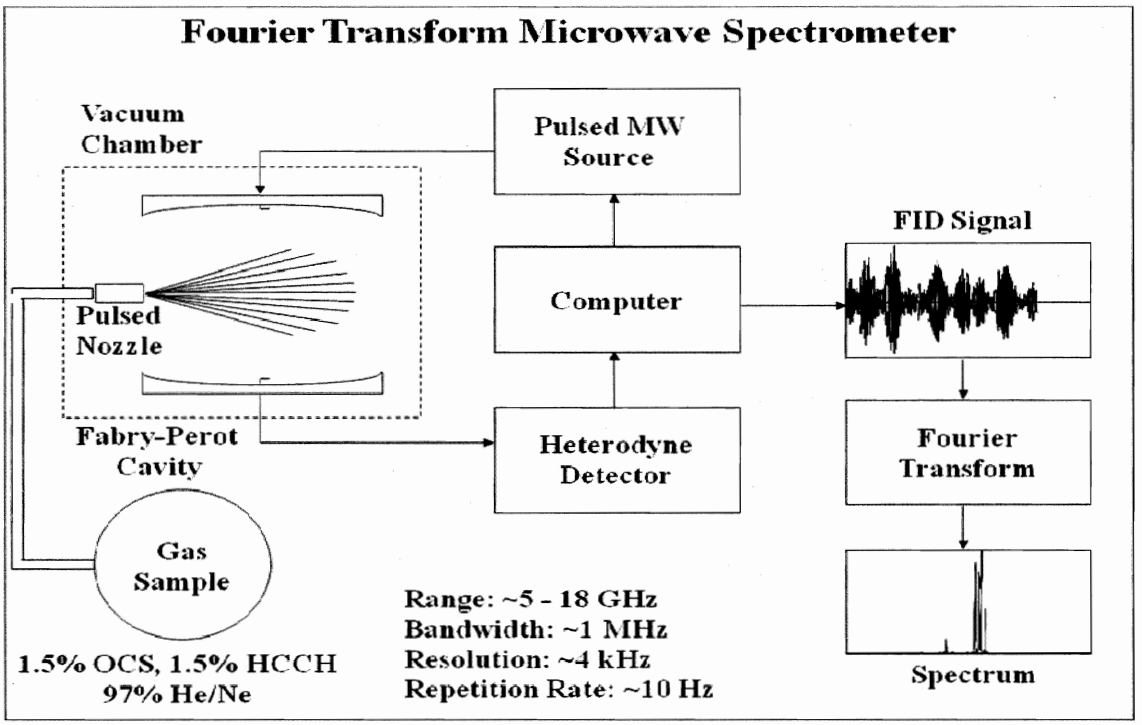

Figure 2.1: Schematic Diagram of the Fourier Transform Microwave Spectrometer

The mirrors are smooth and polished aluminum and have microwave antennae protruding from their center. The microwave radiation is produced in the cavity by a microwave synthesizer and induces an electric dipole polarization of all of the molecules in the gas expansion, and a free induction decay (FID) is detected as the molecules relax from rotational excitement. The sequence of events in the experiment involves a gas pulse, followed by a pulse of microwave radiation that resonates within the Fabry-Pérot cavity building the power within the cavity that polarizes the molecules (thereby rotationally exciting the molecules) in the expansion. As the radiation is switched off and the molecules relax, the emission of radiation from the excitation is detected. One polarizing pulse of microwave radiation is propagated for each gas pulse, and another after each gas pulse is evacuated from the chamber, and any residual emission from the chamber is detected by the same antenna that propagates the microwaves. The gas pulse and

microwave power are the adjustable timing parameters and are on the microsecond timescale. The radiation emitted from the rotationally excited molecules is detected and is stored in an averaging system, while the residual emission effects are subtracted from the data collected to remove any noise. Averaging this process for 100 to 10000 gas pulses which are pulsed at 10 gas pulses per second (10 Hz) allowing for real signals to be collected with a smooth baseline after the signal accumulates in the averager which greatly reduces any noise that may be introduced into the system.

The pressures achieved within the vacuum chamber can be as low as ~10^{-7} torr, which are obtained with two diffusion pumps (Varian VHS-400 Diffusion Pumps) backed by a large mechanical pump (Alcatel 1200A vacuum pump). Oil inside the diffusion pumps is boiled and any residual gas is pumped out of the cavity at a rate of up to 8000 liters per second by the large mechanical pump, allowing the 10 Hz repetition rate of the nozzle to be maintained without pressure building up in the chamber. A pulsed-valve nozzle (General Valve Nozzle, Series 9 solenoid valve) is utilized to introduce the gas sample between the two mirrors and is aligned perpendicular to the axis of microwave radiation. It is also possible to arrange the nozzle such that the gas sample is introduced coaxially with the microwave radiation, however a disadvantage of this arrangement is that rotational transitions are complicated due to the Doppler effect. The supersonic expansion is very complicated and has been studied in detail[5], however the gas expansion is generally conical in shape as it expands from the nozzle into the cavity. As the molecules enter the vacuum chamber in a perpendicular nozzle arrangement, some molecules move towards the propagated microwaves, and some molecules move away, but the general direction is perpendicular to the radiation, and minimizing the Doppler effect. The Doppler effect is only detectable at the highest end of the frequency range of this instrument with minimal

splitting. In a coaxial arrangement where the molecules are moving with high velocities away and toward the propagated radiation causing Doppler splittings detectable at all wavelengths. An advantage of the coaxial nozzle arrangement is that significantly better resolution may be obtained with this arrangement (1-2 kHz versus 10-20 kHz resolution of our current instrument).

Above and below the gas expansion into the Fabry-Pérot cavity, are two steel mesh plates on which large voltages of opposite polarity can be applied (up to 5000 V each). An electric field is then produced between these steel plates when the voltage is applied, and this electric field is used to perform Stark effect experiments. As outlined in Chapter 1, a uniform static electric field causes perturbations in the rotational energy levels resulting in shifting or splitting of rotational transitions.

2.3. Circuitry and Electronic Components

The instrument and all of its components are controlled with an instrument PC that utilizes the FTMW software written by Jens-Uwe Grabow, and the circuit is based on the Kiel University design.[4] By utilizing this type of setup it is possible to automatically scan the region of interest of the microwave spectrum. The automatic process is used to scan regions of the microwave spectrum of typically about 2 GHz before an assignment is made. The program automatically sets the polarizing frequency to the specified wavelength, tunes the cavity mirrors to resonance at that frequency, and averages the desired number of gas pulses at each step of the process. The frequency scan steps across approximately 0.3 to 0.5 MHz per step (depending on the input of desired parameters into the program), and if a real signal is observed, the data can be saved or the automatic process can be terminated in order to manually measure the transition. The advantages of having an automated system are the increased speed of frequency scanning,

the ability to maintain a steady pace of scanning, and the option to run the spectrometer unassisted. Rotational spectra are usually very sparse and rotational transitions may exist several hundreds of MHz apart from one another, so automated searching is useful in order to scan over large regions of the microwave spectrum.

The circuit used to perform the automated process is the design that is shown in Figure 2.2 and will be described in detail. The first component (1) is the microwave synthesizer (or master oscillator, a Hewlett Packard 8671 frequency synthesizer) which generates the microwave signal anywhere from 2-18 GHz. To drive the spectrometer in phase, the microwave synthesizer also utilizes a 100 MHz sideband and a 10 MHz reference signal. A timing box is controlled by this process which is referenced to the computer (28) and the gas pulse sequence is initiated when required. The timing box is responsible for the timing sequence of the gas pulse, microwave pulse, and all the switches in the circuit. The 100 MHz microwave signal is triggered by a switch (3) after which, the signal travels through an amplifier, low pass filter, phase selector, and a mixer (4-7). At this point the 100 MHz reference signal is mixed with the microwave signal generated by the microwave synthesizer (1) that passed through attenuators (11 and 12) and the directional coupler (13). The signal is then passed through a switch (8), amplified (9), and radiation is released into the Fabry-Pérot cavity via switch (10). The same antenna is used to propagate the microwave signal and to detect any molecular signal from the sample. Switch (10) then allows any detected signal to an amplifier (14) and mixed with the microwave signal (15), followed by a downconversion to 100 MHz plus the molecular signal.

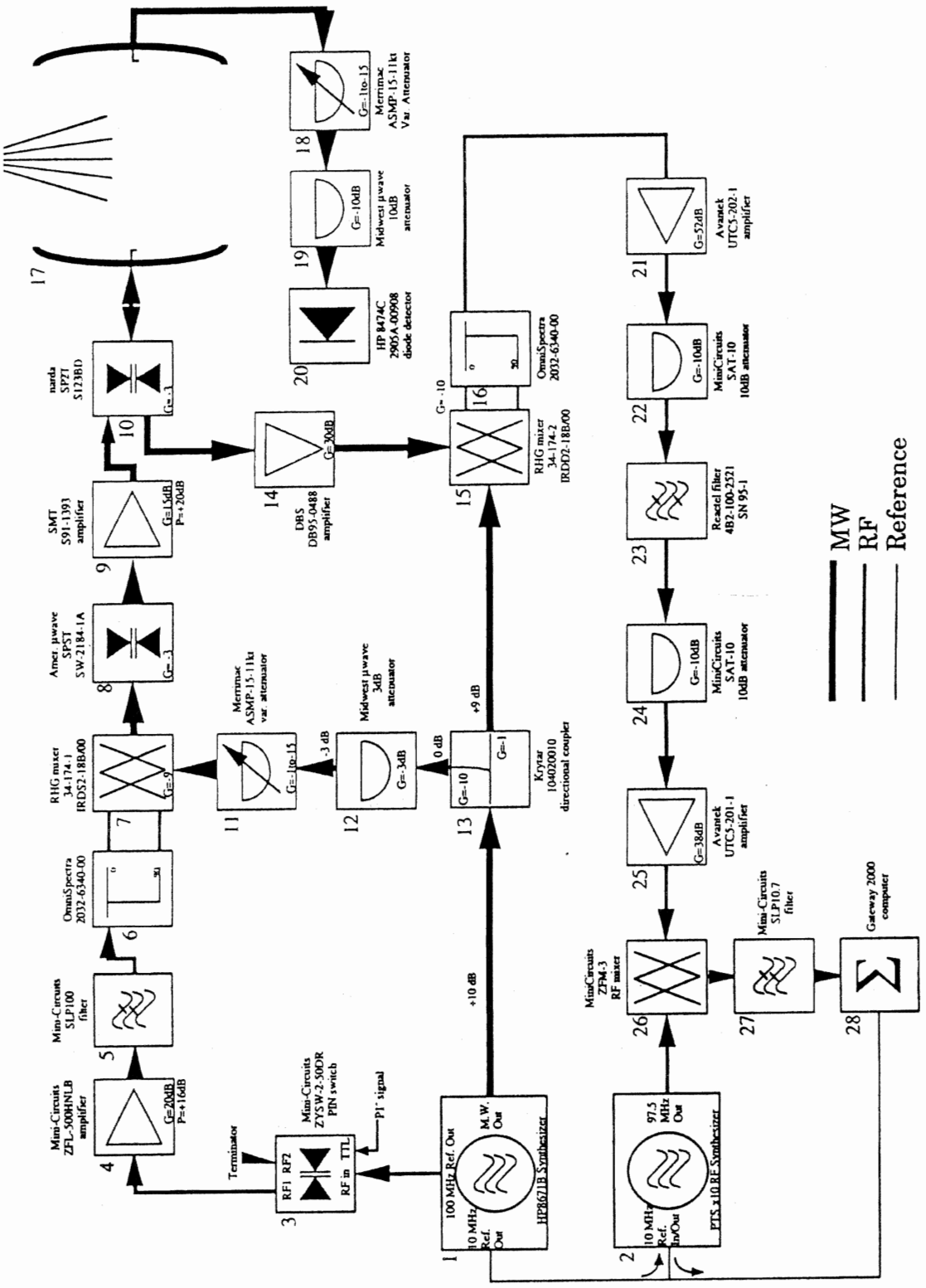

Figure 2.2: Schematic of the North Spectrometer MW/RF Circuit

When microwave radiation of the excitation frequency is applied to the chamber containing the molecular system of interest, the molecules are rotationally excited and the dipole moments begin to rotate in phase, generating a macroscopic polarization of the individual dipole moments of all of the molecules. The emitted signal corresponds to decay of the macroscopic polarization with time as a free induction decay. The signal is phase selected (16), amplified and passes through several attenuators (21-25) which is used to amplify the signal of interest, before it is reduced to 2.5 MHz plus any molecular signal with the radio frequency of 97.5 MHz which is generated by (2). A low pass filter is used to filter any higher range frequencies that are not desired, and the signal is then transmitted to the computer, and the computer obtains the free induction decay if a signal is observed. Components (18-20) are used to tune the Fabry-Pérot cavity, where the antenna not used to propagate microwaves, detects the radiation within the cavity, converts the signal to a voltage and is passed through to the oscilloscope. The cavity is manually tuned using an oscilloscope to display any resonant modes within the cavity. It is important to locate modes of microwave radiation resonance, because this is the basic principle that allows successful operation of the Fabry-Pérot cavity. In an automated search, the computer has the ability to track these modes if the tuning parameters per step are changed in relation to the frequency and need to be adjusted approximately every 200 MHz for optimal automated searching. If the mode tuning parameters are not changed every 200 MHz in an automated search, the distance between the two mirrors will not adjust correctly according to frequency of radiation, resulting in an untuned cavity that will not contain resonant radiation.

Several other electronic components are incorporated into the system which are also responsible for spectrometer operation. A pressure gauge is attached to the sample manifold which displays the sample pressure (usually kept between 1500 and 2500 mbar). A mirror

control box is utilized to control the distance between the two mirrors. One of the two mirrors is on a movable carriage which is moved with a stepper motor controlled by the mirror control box. A pressure gauge is used to display the pressure within the vacuum chamber and can measure pressures down to 10^{-7} torr. An Iota One valve control box controls the General Valve solenoid valve and the settings can be modified for sample introduction into the vacuum chamber. A power source is also need to supply power to the amplifiers and switches in the circuit. To produce the static electric field on the Stark plates, two Glassman High Voltage (EL series) power supplies are utilized to apply the desired voltage across the Stark plates.

2.4. Theoretical Calculations

The region accessible by the FTMW spectrometer is from 4 to 18 GHz, and the average step in an automated search may be from 0.3 to 0.5 MHz. It would be an extremely tedious endeavor to scan the entire region accessible by the spectrometer with this automated technique, thus it is necessary to acquire good theoretical structural models of the systems studied. Theoretical calculations provide reasonable structural parameters which in turn allow for predictions of where rotational transitions may exist. Since the rotational spectrum occurs due to the rotational excitation of the molecular systems studied, changes in the theoretical moments of inertia will cause variations in the theoretical rotational spectrum. Therefore, if large uncertainties are obtained in the theoretical calculations, the predicted spectrum will also have large uncertainties, making it more difficult to locate the experimental spectrum. If highly accurate theoretical structures are obtained, then small search regions of high probability of rotational transitions are determined which reduce the cost of time when searching for rotational spectra. The program utilized for molecular modeling is called Gaussian 03.[6] It is an electronic structure program that

employs the basic laws of quantum mechanics in order to predict energies, molecular structure, or other parameters and molecular properties. To predict microwave spectra, Gaussian03 is utilized to obtain the lowest energy structure of the molecular system of interest. Gaussian03 is not directly used to predict rotational spectra; however, rotational constants can be obtained from the geometries of the molecular systems with the lowest (most stable) optimized energies. Other theoretical parameters which are obtained include bond angles, bond distances, dipole moments, and, in the case of quadrupolar nuclei the electric field gradients can be calculated to provide a prediction of the hyperfine structure in the spectrum (see eq. 6 in Chapter 1). Once the rotational constants are obtained, a rigid rotor model (RRFIT[7]) is utilized to predict theoretical rotational spectra, which is a model that can be used to predict rotational energies of molecules. The program RRFIT is written so that the rotational energy levels are obtained from the rotational constants for a rigid system, and since rotational spectra occur due to the difference in rotational energy levels, the rigid system is the first theoretical predicted spectrum that is used to narrow down a search region for the rotational spectrum. It is important to note that the rotational spectrum obtained from the rigid rotor model is only a theoretical spectrum and is used to identify and initial search region and also to provide a means for initial assignment of the spectrum. The rigid rotor model does not take into account distortion that occurs when molecules are rotationally excited. When the molecules distort due to rotational excitement, the moments of inertia will distort as well, resulting in slightly different transition frequencies. Theoretical rotational spectra are only used as a guide when locating rotational spectra, which may be predicted up to 0.5 GHz away from the actual rotational spectrum after distortion effects are taken into account. When searching for rotational spectra in the microwave region, the lowest *J* rotational transitions that are accessible are typically chosen to locate first. This is due

to the fact that in a supersonic expansion the lowest J rotational energy levels will have the highest population, resulting in transitions of highest intensity. Three dipole moment components are also calculated that correspond to the axis on which they lie i.e. μ_a corresponds to the *a*-axis, μ_b corresponds to the *b*-axis, and μ_c corresponds to the *c*-axis. Dipole moment components are also an important factor to take into account from structural predictions, because if a particular dipole moment component is larger for a particular direction, it will lead to more intense rotational transitions. This is because stronger dipole moment components will be more easily polarized resulting in a stronger signal of microwave radiation emitted.

2.5. Fitting Rotational Spectra

Once a portion of the desired rotational spectrum is located, it is necessary to assign quantum numbers to the rotational transitions that are obtained. Experimental spectra are fit with the program SPFIT by Herb Pickett,[8] which can calculate and predict energies and intensities of rotational transitions of asymmetric rotors, symmetric tops, and linear molecules. The program will fit rotational transitions to the designated quantum numbers which must be provided, and also has the capability to add centrifugal distortion parameters to the fit. This is important because as the molecule is rotationally excited, it does not remain rigid (as described by the rigid rotor model), but the molecule will distort due to centrifugal forces, and thus the moment of inertia changes. Once the spectrum is fit, it is possible to utilize SPFIT to predict all the remaining rotational transitions for the molecular system of interest. This is useful because it is no longer required to search the entire spectrum for transitions, rather specific rotational transitions are selected that fall within the accessible region, and if the fit is correct these

rotational transitions are easily located and then added to the fit to further refine the fitted rotational constants.

Another spectral feature which is prominent in the types of molecular systems described herein, is the splitting which arises due to internal rotation. An internal rotor can exist in a molecular system if the barrier to rotation is low enough to allow for torsion about the bond axis. If there is an internal rotor (such as a methyl group) in the molecular system, the rotational spectrum is split into *A* and *E* states (the number of peaks in the spectrum is effectively doubled). The *A* states correspond to the rotational spectrum that would exhibit rotational parameters if no internal rotation would be present, and the *E* states introduce the coupled internal rotation to the overall rotational angular momentum, thus splitting the spectrum. A separate program, called XIAM[9] is utilized to fit a spectrum that displays *A* and *E* state splitting. XIAM will also calculate the barrier to rotation for the internal rotor from the rotational spectrum, as well as, the angle of the internal rotation axis with regard to the coordinate system used, and the moment of inertia of the internal rotor. Centrifugal distortion constants are also utilized by XIAM to correctly fit the rotational spectrum, and similarly to SPFIT, once the spectrum is fit correctly, all of the rotational transitions can be predicted and easily located. XIAM was used in the analysis of the cyclopropylmethylgermane molecule which will be discussed in Chapter 3.

References

[1] Balle, T. J., Campbell, E. J., Keenan, M. R., Flygare, W. H. *J. Chem. Phys.* **1979**, *71*, 2723-24.

[2] A.C. Legon. *Ann. Rev. Phys. Chem.* **1983**, *34*, 275-300.

[3] Balle, T. J.; Campbell, E. J.; Keenan, M.R.; Flygare, W. H. J. *Chem. Phys.* **1980**, *72*, 922-33.

[4] Grabow, J.U.; Stahl W.; Dreizler, H. *Rev. Sci. Instrum.* **1996**, *67*, 4072.

[5] Campbell, E.J.; Buxton, L.W.; Balle, T.J.; Keenan, M.R.; Flygare, W.H. J. *Chem. Phys.* **1981**, *74(2)*, 829-840.

[6] Frisch, M. J.; Trucks, G. W.; Schlegel, H. B.; Scuseria, G. E.; Robb, M. A.; Cheeseman, J. R.; Montgomery, J. A., Jr.; Vreven, T.; Kudin, K. N.; Burant, J. C.; Millam, J. M.; Iyengar, S. S.; Tomasi, J.; Barone, V.; Mennucci, B.; Cossi, M.; Scalmani, G.; Rega, N.; Petersson, G. A.; Nakatsuji, H.; Hada, M.; Ehara, M.; Toyota, K.; Fukuda, R.; Hasegawa, J.; Ishida, M.; Nakajima, T.; Honda, Y.; Kitao, O.; Nakai, H.; Klene, M.; Li, X.; Knox, J. E.; Hratchian, H. P.; Cross, J. B.; Bakken, V.; Adamo, C.; Jaramillo, J.; Gomperts, R.; Stratmann, R. E.; Yazyev, O.; Austin, A. J.; Cammi, R.; Pomelli, C.; Ochterski, J. W.; Ayala, P. Y.; Morokuma, K.; Voth, G. A.; Salvador, P.; Dannenberg, J. J.; Zakrzewski, V. G.; Dapprich, S.; Daniels, A. D.; Strain, M. C.; Farkas, O.; Malick, D. K.; Rabuck, A. D.; Raghavachari, K.; Foresman, J. B.; Ortiz, J. V.; Cui, Q.; Baboul, A. G.; Clifford, S.; Cioslowski, J.; Stefanov, B. B.; Liu, G.; Liashenko, A.; Piskorz, P.; Komaromi, I.; Martin, R. L.; Fox, D. J.; Keith, T.; Al-Laham, M. A.; Peng, C. Y.; Nanayakkara, A.; Challacombe, M.; Gill, P. M. W.; Johnson, B.; Chen, W.; Wong, M. W.; Gonzalez, C.; Pople, J. A.; Gaussian 03, revision D.01; Gaussian, Inc.: Pittsburgh, PA, **2004**.

[7] Rigid Rotor Spectrum Fitting Program. Version 3.1

[8] Pickett, H.M. *J. Mol. Spec.* **1991**, *148*, 371.

[9] Dreizler, H.H. XIAM, version 2.5e, *Z. Naturforsch*, **1996**, *51a*, 923.

Chapter 3

Internal Rotation Effects in the Cyclopropylmethylgermane molecule (CMG)

3.1. Introduction

Unlike the weakly bound complexes that will be described in the DFM–OCS and FM–OCS chapters, cyclopropylmethylgermane (CMG) is a stable compound that exists in the liquid phase. Rotational spectroscopy is useful in the determination of structure and dynamics of such a molecule, and new computational techniques were explored in our lab by utilizing the CMG molecule as a prototype for internal rotation analysis. The program XIAM[1] had never been utilized before in our lab to determine internal rotation parameters, and this molecule provided the ideal situation to learn how to perform fits with species that have internal motions in addition to quadrupolar nuclear effects. The compound was synthesized by Dr. Gamil A. Guirgis at the College of Charleston, South Carolina. The work described in this chapter therefore contains contributions from several people. Michael Foellmer and Amanda Steber helped in measurement of transitions for several isotopes and some dipole moment data, while Jon Murray provided theoretical estimates of the nuclear quadrupole coupling constants for the ^{73}Ge species. My main contribution, in addition to measuring numerous transitions, was in fitting the data and determining internal rotation parameters with the XIAM program. The initial interest in the molecule originated in the confirmation of the products of synthesis (via FTMW), with a determination of the most stable conformer of CMG. Figure 3.1 displays the three conformations that this molecule can exhibit.

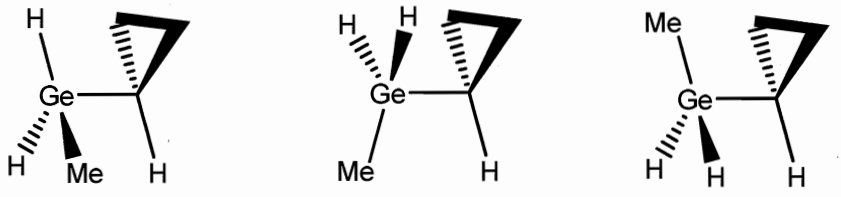

Figure 3.1: The *gauche*, *trans*, and *cis* conformations of cyclopropylmethylgermane (CMG). The methyl group is either *gauche*, *trans*, or *cis* to the cyclopropyl ring.

The Newman projections in Figure 3.2 display the three stable conformers (determined by comparing relative energies obtained from *ab initio* calculation) of the *g*-CMG (*gauche*-cyclopropylmethylgermane), *t*-CMG (*trans*-cyclopropylmethylgermane), and *c*-CMG (*cis*-cyclopropylmethylgermane). The projections are prepared looking down the C–Ge bond, where the carbon atom is at the apex of the cyclopropyl ring. The methyl group is sterically hindered in the *c*-CMG conformer, and therefore it is plausible that this conformation of CMG will have a higher relative energy compared to the *gauche* conformer.

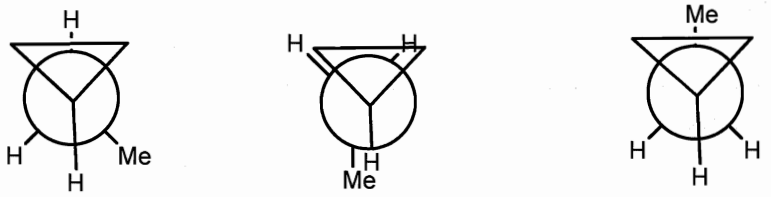

Figure 3.2: Newman projections of *g*-CMG, *t*-CMG and *c*-CMG. These are prepared by looking down the cyclopropyl carbon to germanium bond.

Notice in Figure 3.1 that there is a C_3 internal rotation axis for the methyl top. Internal rotation about this Ge–C bond (of the methyl group or Ge–CH_3) with a three fold 120° rotation of the methyl group will cause three identical structures, however, rotational spectra would become perturbed by this internal motion resulting in *A* and *E* state splitting (arising from the splitting of rotational spectra into the singly degenerate *A* state and the doubly degenerate *E* state, see Chapter 1 for details). Therefore each rotational transition will be split into two lines. Compounds that exhibit internal rotation splitting have not previously been explored in our lab, and the XIAM[1] program had to be well understood before it could be applied to study the internal rotation of the fluorinated methane subunit is likely in the series of OCS/CO_2 complexes described in later chapters. Table 3.1 was prepared to examine relative barriers to rotation (V_3) in molecules that

would exhibit a similar motion as expected in CMG (i.e. a three fold rotation of the methyl group about the Ge–Me bond) and provided initial estimates for a barrier to rotation of the methyl group. The large barriers exhibited by these types of molecules provides an ideal opportunity to easily locate the splitting of rotational spectra due to internal rotation, because molecules with large internal rotation barriers display *A* and *E* state transitions that exist in close proximity to one another (split by only a few MHz or kHz). This is an advantage because it will not be necessary to search large regions of the microwave spectrum in order to locate the *A* and *E* state transitions (which was necessary with the FM-OCS complex[2]).

Table 3.1: Comparison of barriers to internal rotation for compounds similar in composition to CMG.

Compound	V_3 / kJ mol^{-1} (cm^{-1})	Reference
Ethane	12.054 (1007.6)	3
Methylsilane	6.950 (581.0)	4
Methylgermane	5.187 (443.6)	5
Methylfluorogermane	3.936 (329.0)	6
Dichlordimethylgermane	5.803 (485.1)	7
Trimethylchlorogermane	4.459 (372.7)	8
Vinylgermane	5.183 (433.3)	9
(trifluormethyl)germane	5.359 (448.0)	10
Fluoromethylgermane	5.820 (486.5)	11

The CMG molecule was therefore utilized to learn the how to properly use a fitting program containing a Hamiltonian that includes internal rotation terms, which could then be applied to weakly bound complexes such as FM–OCS[12] or TFM–CO_2.[13] The program XIAM was used to fit the rotational spectra of this compound, resulting in assignment of *A* and *E* state transitions and the determination of structural information as well as the

barrier to rotation of the methyl group. It also has the capability to fit the relative angle of the internal rotor axis to the principal axis and the moment of inertia of the top. The experience gained in the use of XIAM was then correctly applied in the determination of internal rotation parameters in TFM-CO_2 weakly bound complex.[13]

There are five isotopes of the germanium atom, which are displayed in Table 3.2 with their relative abundances. Relative abundance of each isotope is important because the relative intensity of rotational transitions is directly related to the concentration of a specific isotope in the gas expansion.

Table 3.2: Relative abundances for the five isotopes of germanium[14].

Isotope of Germanium	Natural abundance	Mass / amu	Nuclear Spin
^{70}Ge	20.5%	69.924250	0
^{72}Ge	27.4%	71.922079	0
^{73}Ge	7.8%	72.923463	9/2
^{74}Ge	36.5%	73.921177	0
^{76}Ge	7.8%	75.921401	0

The isotope with the lowest abundance (^{73}Ge) is identified as having nuclear spin ($I = 9/2$), which couples to the overall rotation of the isotopologue containing the ^{73}Ge nucleus, resulting in hyperfine splitting of rotational spectra (see Chapter 1 for details). To accurately assign the spectrum of the ^{73}Ge isotopomer, nuclear quadrupole constants (χ_{aa} and $\chi_{bb}-\chi_{cc}$ defined in eq. 6 of Chapter 1) had to be determined from the electric field gradient experienced at the quadrupolar nucleus, which can be calculated by Gaussian03. XIAM also has the capability of determining experimental nuclear quadrupole coupling constants from rotational spectra. Theoretical nuclear quadrupole constants were predicted at several levels using density functional theory (DFT) and

compared to experimentally determined quadrupole coupling constants for several molecules. It was determined by an undergraduate student that the DFT level with a 6-311++G(3df,3pd) basis set provided the most reliable results for quadrupole coupling constants compared to known values for related molecules ($ClGeH_3$ and $MeGeH_3$).[15] Density functional theory (DFT) is still relatively new (and unexplored in our lab), and it was interesting to note that it performs well in the determination of quadrupole coupling constants (for the germanium atom).

3.2. *Ab initio* calculations

Structural optimizations were performed with Gaussian 03[16] at the MP2 level with a 6-311++G(2d,2p) basis set to obtain theoretical rotational constants, dipole moment components, and relative energies of the two most stable conformations of CMG (i.e. *g*–CMG and *c*–CMG). There is a third possible conformation of this complex (see Fig. 3.1), where the methyl group orients itself *trans* to the cyclopropyl ring. This involves a 180° rotation of the C–Ge bond in *c*–CMG (see Figure 3.1) which was found to have a 521 cm^{-1} higher relative energy than the *gauche* conformer (which had the lowest relative energy determined by *ab initio* methods), so the *t*–CMG conformer was ignored because it is too high in energy to be observed in the gas expansion. At first glance it seems strange that the *trans* conformer is so much higher in energy because there is no steric hindrance between the methyl and cyclopropyl substituents, but upon closer examination it becomes clear that a 180° rotation of the C–Ge bond of the *cis* conformer results in an eclipsed conformation (rather than the staggered conformations of the *cis* and *gauche* conformers with respect to the cyclopropyl ring) and a significant increase of bond strain resulting in an increase of the calculated energy. Figure 3.3

shows the two optimized structures obtained from Gaussian 03, for the ^{74}Ge isotopologue of *g*–CMG and *c*–CMG.

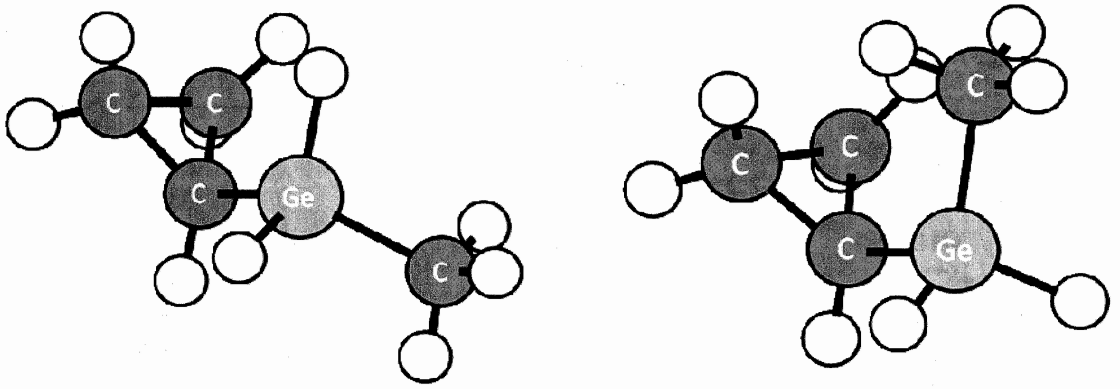

Figure 3.3: Two plausible conformations of the CMG molecule (*g*-CMG and *c*-CMG respectively), with *c*-CMG having 55 cm^{-1} higher relative energy than *g*-CMG.

The theoretical rotational constants and dipole moment components computed by *ab initio* methods for *g*–CMG and *c*–CMG are tabulated in Table 3.3 with their corresponding relative energies. These results indicate that the *c*–CMG conformer (with a 55 cm^{-1} relative energy higher than the *g*–CMG conformer) may exist in the gas expansion, and it is possible that it could be observed experimentally.

Table 3.3: Theoretical rotational constants, dipole moment components, and relative energies of the *g*–CMG and *c*–CMG conformers obtained by *ab initio* methods (results shown for calculation of ^{74}Ge isotopologue with highest natural abundance).

Parameter	*g*–CMG	*c*–CMG
A / MHz	7186	5260
B / MHz	1889	2110
C / MHz	1653	1805
μ_a / D	0.21	0.52
μ_b / D	0.62	0.41
μ_c / D	0.30	0.00
μ_{tot} / D	0.72	0.66
Relative energy / cm^{-1}	0	55

3.3. Spectra

The rotational constants obtained from the *ab initio* calculations were then utilized to predict spectra for all isotopologues of *g*–CMG using RRFIT, and the predicted spectra provided excellent direction in locating rotational transitions. The ^{74}Ge isotopologue $1_{11}\leftarrow0_{00}$ *b*–type was predicted at 8920.2 MHz and was located at 9166.2973 MHz, while the $2_{02}\leftarrow1_{01}$ *a*–type was predicted at 7233.5 MHz and was located at 7230.1908 MHz. Clearly the predicted spectra of the optimized structures were in reasonable agreement with observed rotational transitions, and the observed rotational transitions reflected the rotational constants of the *g*–CMG conformer.

A doubling of rotational transitions (approx. 1-5 MHz) were attributed to the *A* and *E* state internal rotation splitting coming from the internal rotation of the methyl group. By changing the mass of the germanium atom to the specific isotopic masses of each isotopologue, it was possible to obtain rotational constants for each respective isotopologue (based on the *ab initio* structure of *g*–CMG). An interesting pattern was

observed in the spectrum, where the $1_{11} \leftarrow 0_{00}$ transitions of the ^{70}Ge, ^{72}Ge, ^{74}Ge, and ^{76}Ge, isotopologues were evenly separated in the spectrum by approximately 30 MHz, with the spectrum of the ^{73}Ge isotopologue located roughly half way between the spectra of the ^{72}Ge and ^{74}Ge isotopologues (see Figure 3.4). The relation of these spectra can be explained by the change in mass in going from one isotopologue to another. Rotational spectrometers are more than capable of distinguishing the mass difference of isotopologues. Mass, being directly proportional to moment of inertia, which is itself inversely proportional to the rotational constant, dictates that spectrum of the heaviest isotopologue occurs at lower frequencies than lighter isotopologues. Using this rationale, it was possible to locate and assign the spectra of the five isotopologues rapidly due to the proximity of rotational transitions as is displayed in Figure 3.4a. Figure 3.4b is an enlargement of the spectrum for the ^{76}Ge isotopologue to display the internal rotation splitting observed in the spectrum. There were several unassigned transitions in the spectrum which could perhaps belong to the *c*–CMG conformer. The rotational constants of *c*-CMG and *g*-CMG differ by up to ~2 GHz, so determining the spectrum would unambiguously assign the conformer of higher stability, however we have not attempted to assign any of the unassigned lines to a rotational spectrum of the *cis*- conformer.

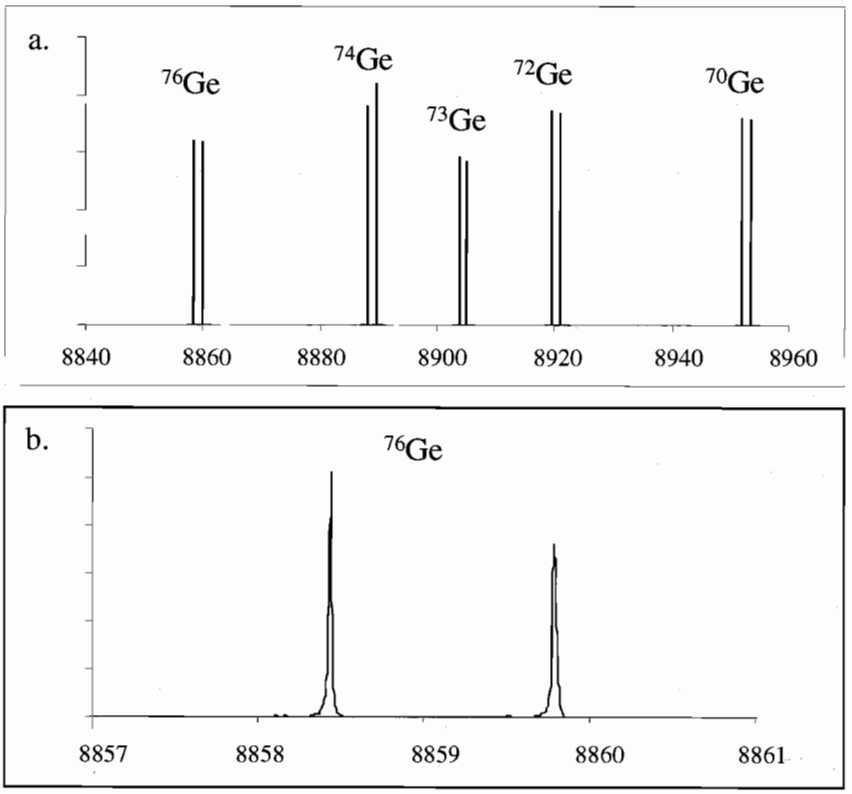

Figure 3.4: a) Observed spectrum in the $1_{11}\leftarrow0_{00}$ region of the spectrum, shows the effect of a mass change of 1 or 2 amu between isotopologues. b) Small splitting observed between *A* and *E* state transitions (specifically shown for the ^{76}Ge isotopologue of *g*-CMG). Frequencies on x-axis given in MHz, intensity given on y-axis.

The program XIAM was utilized to assign the rotational transitions of each isotopologue and the splitting between *A* and *E* state transitions, because the Hamiltonian that XIAM uses has the capability to calculate internal rotation parameters. The relevant portions of the XIAM input file utilized in the fit of the rotational spectrum of the ^{70}Ge isotopologue is shown below:

```
BJ        1.809635955          !    0.5(X+Y)
BK        5.424318155          !    Z-0.5(X+Y)
B-        0.122704095          !    0.5(X-Y)
DJ        0.704000E-6          !
DJK       4.000000E-6          !
V1n    13171.                  ! based on 5.256 kJ / mol
F0     161.72100               ! rot const of top (fix by setting
```

The rotational constants are entered as BJ, BK, and B-, which are functions of *A*, *B*, and *C* (X, Y, and Z respectively; the program utilizes the equations shown in the above input for rotational constant information), followed by the barrier to rotation (V1n where n=3 for the three fold axis of internal rotation) and the rotational constant of the methyl top (F0). The *A* and *E* state rotational transitions are entered separately into the input file, which requires a systematic process of inputting each rotational transition, running the program, and making sure that the *A* and *E* state transitions are fitting correctly. An example of the XIAM output for the ^{76}Ge isotopologue is shown below:

```
            Parameters  and  Errors
BJ             1.798173563 {  .000000245}
BK             5.385588519 {  .000001102}
B-              .122616731 {  .000000300}
DJ              .596921E-6 {  .008624E-6}
DJK            -4.177046E-6 {  .101992E-6}
DK              .000000E-6 {     fixed  }
dj              .181185E-6 {  .006070E-6}
dk              .000000E-6 {     fixed  }
Vss             .000000E-6 {     fixed  }
Vcc             .000000E-6 {     fixed  }
mu_x            .615000000 {     fixed  }
mu_y            .290000000 {     fixed  }
mu_z            .254000000 {     fixed  }
P_x             .000000E-6 {     fixed  }
P_y             .000000E-6 {     fixed  }
P_z             .000000E-6 {     fixed  }
F             163.561394822 {     derived}
F0            159.284773239 {  .316651109}
epsil           .000000E-6 {     fixed  }
delta           .859289677 {  .001025210}

Standard Deviation        .003001 MHz

------------------------------------ B =  1
Rotational Constants and Errors (in GHz)
     B_z       7.183762082        .000001142
     B_x       1.920790293        .000000401
     B_y       1.675556832        .000000373
Ray's kappa    -.91096
F0(calc)     159.284773239        .316651109
I_alpha        3.172802144        .006307391
```

In the output we observe all the non-zero values of parameters have been fitted by XIAM using the rotational transitions obtained from the spectrum. It provides the rotational constants, the distortion constants, the dipole moment data, and the inertial data for the internal rotor. The Hamiltonian utilized by this program is shown below:

(1) $$H = H_{rr} + H_{cd} + H_{ir}$$

where H_{rr} is the Hamiltonian from the rigid rotor (and fits *A*, *B*, and *C*), H_{cd} describes the centrifugal distortion of the molecule, and H_{ir} describes the internal rotation in the molecule and provides the internal rotation parameters such as V_3, F_0, etc. The H_{ir} Hamiltonian is defined below:

(2) $$H_{ir} = F(P_\alpha - \rho P_r)^2 + \frac{V_3}{2}(1 - \cos 3\alpha)$$

The details of the Hamiltonian shown in eq. 2 are beyond the scope of this, but the terms do indicate where the barrier to rotation (V_3), the rotational constant of the methyl top (F), and the torsional angle of the internal rotor (α) are located in the program's Hamiltonian. This program is very useful in its ability to fit many parameters at once, and it is therefore not necessary to utilize many programs to get all the information that this one program provides.

Rotational spectra were located and fit, including the *A* and *E* state transitions, for the five isotopologues of *g*–CMG with observed $\Delta\nu_{rms}$ values not exceeding 5.2 kHz (a measure of the fit quality). The structural and dynamic properties obtained from the fitting of rotational spectra are displayed in Table 3.4, including the rotational constants, centrifugal distortion constants, internal rotation parameters and nuclear quadrupole coupling constants (for the ^{73}Ge species). The nuclear quadrupole coupling constants were calculated by XIAM for the ^{73}Ge isotopologue, and the higher $\Delta\nu_{rms}$ observed can

be attributed to the relatively weak lines (7.8% natural abundance) and the additional hyperfine splitting due to its quadrupolar nucleus that further deteriorates spectral resolution. The theoretical nuclear quadrupole coupling constants[15] were found to be χ_{aa} = 8.26614 MHz, and χ_{bb}-χ_{cc} = 7.8011 MHz at the DFT level of theory with a B3LYP functional and the 6-311++G(3df,3pd), which are have good agreement with experimental values (see Table 3.4). Table 3.5 compares the predicted and experimentally observed quadrupole coupling constants that were used in the assignment of the hyperfine structure arising from the coupling of the ^{73}Ge nuclear spin. The relative sizes of the distortion constants obtained from fitting all the isotopologues of *g*–CMG do not show much variation (as expected). This hold true for the barrier to rotation and the moment of inertia about the methyl top rotor as well.

Table 3.4: Spectroscopic constants for the gauche conformer of CMG.

Parameter	^{70}Ge	^{72}Ge	^{73}Ge	^{74}Ge	^{76}Ge
A / MHz	7260.0925(10)	7233.4857(10)	7220.6101(26)	7208.0673(8)	7183.7621(11)
B / MHz	1938.36354(35)	1932.3070(4)	1929.3477(11)	1926.45300(26)	1920.7902(4)
C / MHz	1692.92029(33)	1686.9185(4)	1683.9929(11)	1681.13359(25)	1675.5568(4)
Δ_J / kHz	0.618(8)	0.622(8)	0.48(4)	0.600(6)	0.597(9)
Δ_{JK} / kHz	–4.4(9)	–4.358(26)	–4.7(7)	–4.29(7)	–4.18(10)
δ_J / kHz	0.183(5)	0.179(6)	0.179(fixed)	0.195(4)	0.181(6)
V_3 / kJ mol^{-1} [a]	4.753(8)	4.737(8)	4.734(23)	4.736(6)	4.740(9)
F_0 / GHz [b]	159.8(3)	159.1(3)	159.2(7)	159.18(21)	159.3(3)
I_α / u Å^2 [c]	3.163(5)	3.176(6)	3.175(13)	3.175(4)	3.173(6)
δ / rad [d]	0.8529(4)	0.8537(10)	0.858(4)	0.8580(7)	0.8593(10)
$< i, a$ / deg [e]	48.84(5)	48.91(6)	49.15(20)	49.16(4)	49.23(6)
$< i, b$ / deg	41.16(5)	41.09(6)	40.85(20)	40.84(4)	40.77(6)
$< i, c$ / deg	90.0	90.0	90.0	90.0	90.0
χ_{aa} / MHz	–	–	8.134(8)	–	–
χ_{bb}–χ_{cc} / MHz	–	–	7.693(26)	–	–
Std. dev. / kHz	2.63	3.44	5.07	2.10	3.00
N [f]	36	52	54	36	36

[a] Barrier to internal rotation of the methyl group [fitted using XIAM version 2.5e]. [b] Rotational constant of the internal rotor, $F_0 = h / 8 \pi^2 I_\alpha$ [fitted]. [c] I_α is the moment of inertia of the internal rotor [derived from the fitted value of F_0]. [d]) δ is the angle between the internal rotation axis (i) and the principal inertial axis ($z = a$). [fitted]. The other angle (ε, the angle between the principal inertial axis (x=b) and the projection of the internal rotation axis (i) into the xy plane) was fixed at a value of 0° since the ab initio structure indicated that the Ge-Me bond coincidentally lies within a degree of the ab plane. [e] $< i, a, < i, b, < i, c$ are the angles between the internal rotor axis (i) and the principal inertial axes (a, b and c, respectively). [Derived from the values of δ and ε]. [f] N is the number of fitted transitions (includes A and E state components)

Table 3.5: Nuclear quadrupole coupling constant (χ) calculations used to assist in the assignment of the nuclear quadrupole hyperfine structure of the ^{73}Ge species.

Parameter	Experimental	Predicted [a)]
χ_{aa} / MHz	8.134(8)	8.266
$\chi_{bb} - \chi_{cc}$ / MHz	7.693(26)	7.800
χ_{aa} / MHz	8.134(8)	8.266
χ_{bb} / MHz	–0.2205	–0.233
χ_{cc} / MHz	–7.9135	–8.033

[a)] χ was derived from the electric field gradient calculated using a B3LYP/6-311++G(3df,3pd) level single point calculation, using the MP2/6-311++G(2d,2p) optimized structure.

3.4. Dipole Moment

The dipole moment components for each isotopologue were determined from second order Stark shifts for eight $|M|$ lobes selected from seven transitions. The experimental rotational constants (see Table 3.4) were used to predict the Stark coefficients with ASYSPEC[17], which were least squares fitted to the measured values obtained from the slope of the $\Delta\nu / E^2$ Stark plots. Table 3.6 contains the experimental and calculated $\Delta\nu / E^2$ values and the dipole moment components for the ^{72}Ge isotopologue. All the $\Delta\nu / E^2$ plots were well behaved with little to no deviation from linearity. The Stark shifts did not exceed 1 MHz from the original frequency with applied voltages of up to ±5 kV. The fitted dipole moment components are in reasonable agreement with the *ab initio* values of $\mu_a = 0.25$ D, $\mu_b = 0.61$ D, and $\mu_c = 0.29$ D, with $\mu_{total} = 0.725$ D.

Table 3.6: Dipole moment data for the ^{72}Ge isotopomer.

Transition	$\Delta\nu / E^2$(calc) [a] (10^5 MHz cm^2 / V^2)	$\Delta\nu / E^2$(obs) (10^5 MHz cm^2 / V^2)	% Difference [b]
$1_{10} \leftarrow 1_{01}$ $\lvert M\rvert = 1$	1.7040	1.7047	-0.04
$1_{11} \leftarrow 0_{00}$ $\lvert M\rvert = 1$	0.3712	0.3697	0.40
$2_{12} \leftarrow 1_{01}$ $\lvert M\rvert = 1$	0.5771	0.5745	0.45
$2_{11} \leftarrow 1_{01}$ $\lvert M\rvert = 1$	0.7250	0.7256	-0.09
$3_{03} \leftarrow 2_{02}$ $\lvert M\rvert = 2$	0.4403	0.4406	-0.06
$2_{11} \leftarrow 2_{02}$ $\lvert M\rvert = 2$	1.1819	1.1759	0.51
$3_{12} \leftarrow 3_{03}$ $\lvert M\rvert = 2$	0.4012	0.39622	1.25
$3_{12} \leftarrow 3_{03}$ $\lvert M\rvert = 3$	1.0912	1.0998	-0.79

$\mu_a = 0.1782(10)$ D
$\mu_b = 0.581(4)$ D
$\mu_c = 0.305(9)$ D
$\mu_{total} = 0.680(5)$ D

[a] "$\Delta\nu / E^2$(calc)" is the Stark coefficient obtained from a second-order perturbation theory calculation, using the fitted rotational constants given in Table 3.1.
[b] "% Difference" is obtained from "$\Delta\nu / E^2$(calc)" – "$\Delta\nu / E^2$(obs)"

3.5. Structure

The isotopic data from the five isotopologues of *g*–CMG was used to obtain an accurate determination of the principal axis coordinates of the Ge atom. It was determined that the *gauche* conformer was the most stable and the *ab initio* and experimental rotational constants were in good agreement (see Tables 3.3 and 3.4). The calculated principal axis coordinates of the Ge atom using each set of single isotopic substitution data (using the ^{74}Ge as the parent isotopologue) are shown in Table 3.7, which also includes the *ab initio* principal axis coordinates of the Ge atom acquired from the MP2/6-311++G(2d,2p) optimized structure. The agreement between the Kraitchman coordinates of the Ge atom and the coordinate obtained from *ab initio* calculation is excellent. The coordinates are small, but the agreement in the *a*, *b* and *c* coordinates is at

worst 0.0096 Å (2%), 0.0004 Å (0.1%) and 0.0048 Å (9%), respectively, even given the very small magnitude of the *c*-coordinate. The experimental rotational constants have unambiguously determined that the *gauche* conformer of CMG is present in the gas expansion. The *cis* conformer may still exist in the gas expansion and will most likely exhibit weaker rotational transitions because fewer molecules will be populated at this conformation. There were many unassigned transitions in the searched spectral region which may correspond to the rotational spectrum of the *cis* conformer. This will be pursued if more sample is made available.

Table 3.7: Kraitchman single isotopic substitution coordinates. All errors are to ±0.0001Å.

	^{70}Ge	^{72}Ge	^{73}Ge	^{76}Ge	Ab initio
$\|a\|$ / Å	0.6241	0.6241	0.6239	0.6241	0.6336
$\|b\|$ / Å	0.3440	0.3441	0.3442	0.3439	0.3437
$\|c\|$ / Å	0.0504	0.0500	0.0495	0.0508	0.0543

3.6. Conclusions

The rotational spectra for five isotopologues of the *gauche* conformer of cyclopropylmethylgermane have been located and assigned. *Ab initio* calculations predict this conformer to be the most stable with the *cis* conformer having an energy of 55 cm^{-1} higher than the *gauche* conformer. *A* and *E* state rotational transitions were observed in the spectrum which were attributed to a 120° internal rotation of the methyl group about the Ge-Me bond. Rotational spectral afford precise measurements of rotational constants for each isotopologue, with a calculated barrier to rotation of approximately 4.7 kJ mol^{-1} for all isotopologues, which is comparable to the barriers of

the compounds displayed in Table 3.1. This barrier lies close to trimethylchlorogermane which has a considerably different structure. The internal workings of the XIAM program were explored using the *g*–CMG molecule as a prototypical system for internal rotation analysis, and the program will be utilized in the weakly bound dimer series to try and fit any internal rotation parameters. The nuclear quadrupole coupling constants were determined for the ^{73}Ge isotopologue from the hyperfine splitting caused by the coupling of the quadrupolar nucleus to the overall moment of inertia for this molecule and were in excellent agreement with the DFT predictions. The dipole moment components were obtained via Stark effect experiments, and the dipole moment components were measured for *g*–CMG, which did not show any deviations from linearity for the Stark plots. Determination of detailed structural parameters using Kraitchman isotopic substitution confirmed the Kraitchman coordinate of the Ge atom in the molecule, which were in excellent agreement among isotopologues and *ab initio* predictions.

References

[1] Hartwig, H. Dreizler, XIAM, version 2.5e, *Z. Naturforsch.* **1996**, *51a*, 923.

[2] Serafin, M.M.; Peebles, S.A. *J. Phys. Chem. A.* **2008**, *112*, 1473.

[3] Hirota, E.; Saito, S.; Endo, Y. *J. Chem. Phys.* **1979**, *71(3)*, 1183.

[4] Lin, C.C.; Swalen, J.D. *Rev. Mod. Phys.* **1959**, *31*, 841.

[5] Laurie, V.W. *J. Chem. Phys.* **1959**, *30(5)*, 1210.

[6] Krisher, L.C.; Morrison, J.A. *J. Chem. Phys.* **1976**, *64*, 3556.

[7] Ottaviani, P.; Caminati, W.; Schnell, M.; Grabow, J.U. *Inorg.Chim. Acta.* **2007**, *360(3)*, 1240.

[8] Schnell, M.; Grabow, J.U. *Phys. Chem. Chem. Phys.* **2006**, *8*, 2225.

[9] Cullen, W,R.; Hall, L.D.; Ward, J.E.H. *J. Am. Chem. Soc.* **1974**, *96(24)*, 3429.

[10] Krisher, L.C.; Watson, W.A.; Morrison, J.A. *J. Chem. Phys.* **1974**, *61(8)*, 3429.

[11] Krisher, L.C.; Watson, W.A.; Morrison, J.A. *J. Chem. Phys.* **1974**, *60(9)*, 3417.

[12] Serafin, M.M.; Peebles, S.A. *J. Phys. Chem. A.* **2008**, *112*, 1473.

[13] Serafin, M.M.; Peebles, R.A., Peebles, S.A. *J. Mol. Spectrosc.*, (submitted)

[14] http://physics.nist.gov/PhysRefData/Handbook/Tables/germaniumtable1.htm

[15] Murray, Jon. Fall 2006 Research Report, personal. Eastern Illinois University, **2006**.

[16] Gaussian 03, Revision D.01, Frisch, M. J.; Trucks, G. W.; Schlegel, H. B.; Scuseria, G. E.; Robb, M. A.; Cheeseman, J. R.; Montgomery, Jr., J. A.; Vreven, T.; Kudin, K. N.; Burant, J. C.; Millam, J. M.; Iyengar, S. S.; Tomasi, J.; Barone, V.; Mennucci, B.; Cossi, M.; Scalmani, G.; Rega, N.; Petersson, G. A.; Nakatsuji, H.; Hada, M.; Ehara, M.; Toyota, K.; Fukuda, R.; Hasegawa, J.; Ishida, M.; Nakajima, T.; Honda, Y.; Kitao, O.; Nakai, H.; Klene, M.; Li, X.; Knox, J. E.; Hratchian, H. P.; Cross, J. B.; Bakken, V.; Adamo, C.; Jaramillo, J.; Gomperts, R.; Stratmann, R. E.; Yazyev, O.; Austin, A. J.; Cammi, R.; Pomelli, C.; Ochterski, J. W.; Ayala, P. Y.; Morokuma, K.; Voth, G. A.; Salvador, P.; Dannenberg, J. J.; Zakrzewski, V. G.; Dapprich, S.; Daniels, A. D.; Strain, M. C.; Farkas, O.; Malick, D. K.; Rabuck, A. D.; Raghavachari, K.; Foresman, J. B.; Ortiz, J. V.; Cui, Q.; Baboul, A. G.; Clifford, S.; Cioslowski, J.; Stefanov, B. B.; Liu, G.; Liashenko, A.; Piskorz, P.; Komaromi, I.; Martin, R. L.; Fox, D. J.; Keith, T.; Al-Laham, M. A.; Peng, C. Y.; Nanayakkara, A.; Challacombe, M.; Gill, P. M. W.; Johnson, B.; Chen, W.; Wong, M. W.; Gonzalez, C.; and Pople, J. A.; Gaussian, Inc., Wallingford CT, 2004.

[17] Stark coefficients were calculated using a modified version of the original ASYSPEC code: Beaudet, R. A. Ph.D. Thesis, Harvard University, Cambridge, MA, 1961.

Chapter 4

Rotational Spectra and Structure of Difluoromethane–Carbonyl Sulfide Dimer (DFM–OCS)

4.1. Introduction

Structural parameters have recently been reported for trifluoromethane-carbonyl sulfide[1] (TFM-OCS) and methyl fluoride-carbonyl sulfide[2] (FM-OCS) weakly bound complexes in order to characterize weak intermolecular dipole-dipole and hydrogen bonding interactions. The difluoromethane-carbonyl sulfide (DFM-OCS) dimer was studied by means of Fourier-transform microwave spectroscopy (FTMW) to complete a series of weakly bound systems involving fluorinated methane molecules complexed with carbonyl sulfide (HCF_3–OCS, H_2CF_2–OCS, and H_3CF–OCS) to determine what effects the degree of fluorination on the fluoromethane subunit may have on hydrogen bonding and structural dynamics for these types of systems. Difluoromethane only has two fluorine atoms and two hydrogen atoms which are attached to a central carbon atom. This molecule fits into the series of alkyl halide molecules that are in this series of complexes because it is compared to trifluoromethane (which has three fluorine atoms and one hydrogen atom attached to a central carbon atom) and methyl fluoride (which has one fluorine atom and three hydrogen atoms attached to a central carbon atom). The electronegative fluorine atoms in the alkyl halide subunits cause the hydrogen atoms to acquire acidic character, enabling the formation of at least one C–H···O hydrogen bond. Structurally, the trend observed for the series observed shows that the individual dipole moments in each molecule align themselves in an antiparallel fashion. The driving force behind this type of alignment is a dipole–dipole interaction between the dipole moments of the monomer subunits. Interest in rotational spectra of complexes involving difluoromethane (H_2CF_2, DFM) have been expressed in the literature[3,4,5,6,7] and dimer

dipole moments, rotational constants, internal rotation parameters, and structural parameters were reported.

In this study, rotational spectra have been collected in the ground vibrational state for DFM-OCS to acquire rotational constants, centrifugal distortion constants, and/or any indication of large amplitude motions of the DFM subunit. Two low energy structures have been obtained via *ab initio* calculations (shown in Fig. 4.1). It is possible that the difluoromethane molecule may perform a 180° rotation about its C_2 axis, however no spectral evidence so far confirms such a large amplitude motion for this complex.

Interestingly, the rotational spectrum of the DFM–oxirane system[3] displays a low energy conformation where both hydrogen atoms in DFM interact through hydrogen bonding interactions with the oxygen atom on the oxirane subunit. Unlike DFM–oxirane, the low energy conformation obtained from computational techniques for DFM-OCS exhibits one C–H···O hydrogen bond, and this structure was confirmed by the rotational spectrum. Due to the excellent sensitivity of FTMW spectroscopy, the spectra of H_2CF_2–$OC^{34}S$ and $H_2{}^{13}CF_2$–OCS were measured in natural abundance, which helped to unambiguously determine the molecular structure of this complex.

4.2. *Ab Initio* Calculations

Gaussian 03[8] was utilized to obtain two low energy conformations of DFM–OCS at the MP2/6-311++G(2d,2p) level which are shown in Fig. 4.1, and denoted as Structures I and II. Both structures are very similar and are related by the fact that both hydrogen atoms and both fluorine atoms are in the *ab* plane of symmetry in Structures I and II respectively. Structure I was determined to be the low energy structure while Structure II had a relative energy of 76 cm^{-1} higher compared to Structure I.

Theoretically, Structure II is quantitatively sufficient energy such that the population of DFM–OCS dimers in this configuration should not be observable in the microwave spectrum. At first glance, both arrangements of the molecules in Structures I and II seem intuitively plausible; however, the rotational constants are very different (see Table 4.1). In Structure I we see that there are two fluorine atoms out of the *ab* plane of symmetry while Structure II has two hydrogen atoms sticking out of that symmetry plane. A calculation of the mass out of the *ab* plane of symmetry (two F atoms in I, and two H atoms in II) would help to correctly identify the structural arrangement of these molecules in the system. Rotational spectra depend on moments of inertia projected in a three dimensional axis system, therefore due to the symmetry in this complex, if two hydrogen atoms or two fluorine atoms are out of the plane of symmetry then the moments of inertia will be significantly different, resulting in observation of rotational spectra for one or both species. The theoretical rotational constants and structural parameters for both *ab initio* structures are tabulated in Table 4.1.

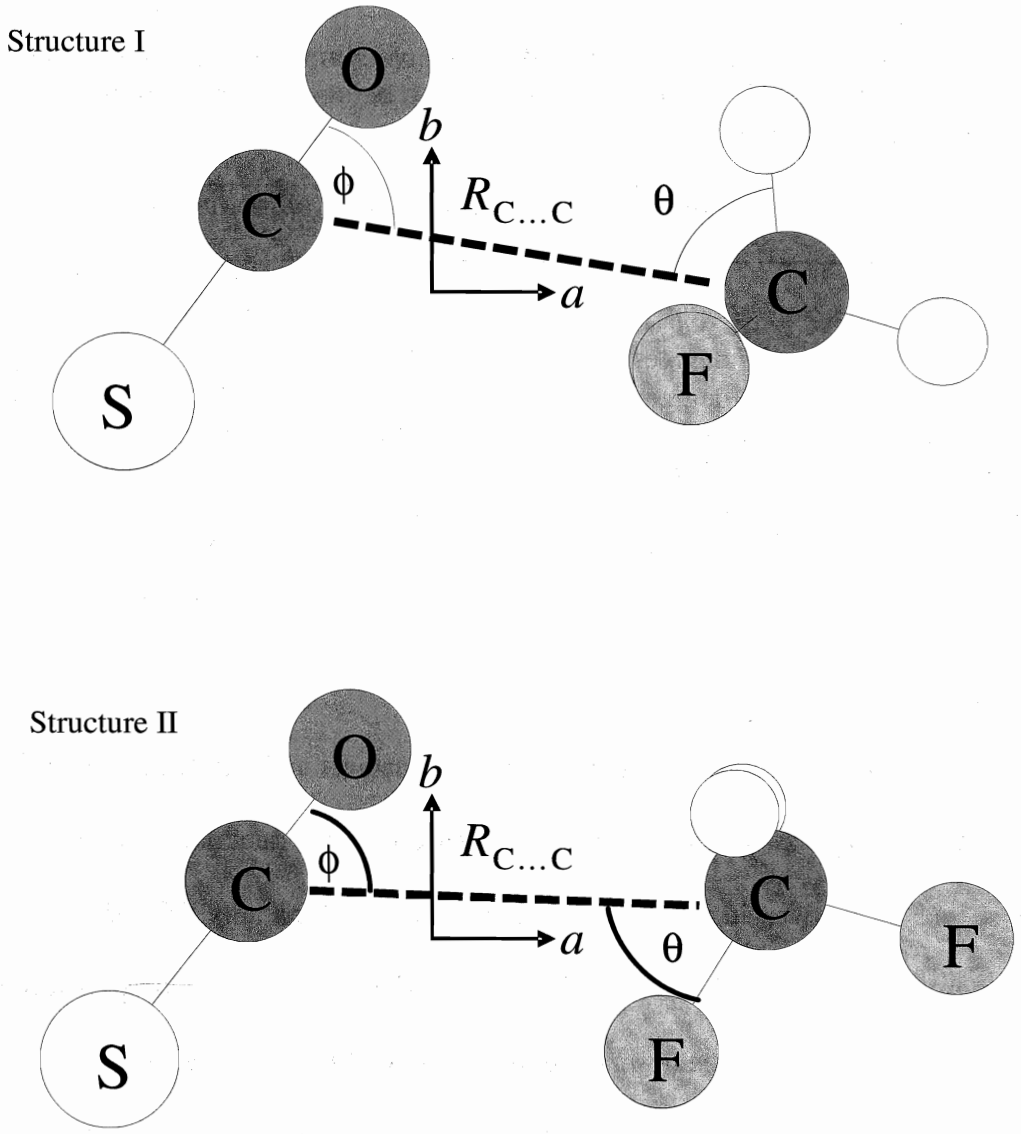

Figure 4.1: Structure I - Low energy structure of DFM–OCS obtained at the MP2/6-311++G(2d,2p) level of calculation, also determined to be actual experimental structure. Structure II - Structure of DFM–OCS obtained at the MP2/6-311++G(2d,2p) level of calculation, higher in energy by 76 cm^{-1} relative to Structure I.

Table 4.1: Structural parameters and rotational constants obtained from the *ab initio* (MP2/6-311++G(2d,2p)) optimizations on Structures I and II. Structural parameters defined in Figure 4.1.

Parameter	Structure I	Structure II
$R_{C...C}$ / Å	3.450	3.610
θ / degrees	74.9	58.4
ϕ / degrees	63.8	53.4
A / MHz	4480	7597
B / MHz	1333	914
C / MHz	1266	820
Relative energy / cm^{-1}	0	76

4.3. Spectra

Rotational spectra have afforded rotational constants and dipole moment data for the DFM–OCS complex. The spectra were slightly congested due to the population of several species that exist within the spectral region searched (namely DFM dimer and trimer spectra),[9,10] however, the rotational spectrum of the DFM–OCS complex has been unambiguously assigned for the normal, H_2CF_2–$O^{13}CS$, H_2CF_2–$OC^{34}S$, and $H_2{}^{13}CF_2$–OCS isotopomers of this complex. It is still possible that the rotational spectrum of Structure II may be assigned from transitions that have been located in the spectrum, but the rotational constants are very different between Structures I and II and therefore the rotational spectra will appear to be very different as a result. The near prolate asymmetric nature of the DFM–OCS dimer (with $\kappa = -0.96$; see eq. 3 in Chapter 1), means that the rotational spectrum is symmetrically spaced easing the task of assignment. The intense *a*–type spectrum had signal to noise ratios of approximately 80 in 100 gas pulses, while the *b*–type spectrum was weaker with signal to noise ratios of

about 50 in 200 gas pulses. The spectra of the H_2CF_2–$O^{13}CS$ isotopomer were located utilizing an enriched sample (Icon Isotopes), while the spectra of the H_2CF_2–$OC^{34}S$, $H_2{}^{13}CF_2$–OCS and the normal isotopomers were located in natural abundance. This explains the lower number of transitions measured for the H_2CF_2–$OC^{34}S$ and H_2CF_2–$O^{13}CS$ isotopomers (weak intensity due to approx. 4%, and 1% abundance respectively). The rotational constants (*A*, *B*, and *C*) were obtained once the spectrum was fit to a Watson *A*-reduction Hamiltonian[11] using Herb Pickett's SPFIT[12] program, and the rotational transitions used to fit the normal isotopomer are displayed in Table 4.2. Table 4.3 contains the experimental rotational constants and distortion constants obtained from the Watson *A*-reduction Hamiltonian[15], and the normal isotopomer was fit to 1.7 kHz. This is considered to be an excellent fit, because a fit of the rotational transitions measured by a spectrometer should not exceed the measurement reproducibility, which in our case is 4 kHz. The planar moments for all the isotopomers are also tabulated in Table 4.3, and for each isotopomer the P_{cc} value (which describes the mass lying out of the *ab* plane) obtained from the rotational constants confirms that the two fluorine atoms are out of the *ab* plane of symmetry which will be discussed further in the Structure section below. Several unidentified rotational transitions do exist in the rotational spectrum of this complex, however, none of these could be directly linked to the existence of a rotational spectrum for Structure II of DFM-OCS. The possibility remains that rotational spectra for the species corresponding to Structure II may still be located in the searched region, but only Structure I has been unambiguously assigned from the spectrum.

Table 4.2: Rotational transition frequencies for the normal isotopic species of the dimethyl fluoride–OCS complex.

$J'_{K_aK_c} \leftarrow J''_{K_aK_c}$		ν_{obs} / MHz	$\Delta\nu$ / MHz [a]
1_{11}	0_{00}	5717.4974	0.0019
2_{12}	1_{11}	4912.6581	0.0009
2_{02}	1_{01}	4977.0063	0.0001
2_{11}	1_{10}	5043.2220	–0.0010
2_{12}	1_{01}	8141.0943	–0.0012
2_{20}	2_{11}	9685.8943	–0.0009
2_{21}	2_{12}	9880.7724	0.0017
2_{21}	1_{10}	14728.1285	–0.0023
2_{20}	1_{11}	14794.4162	0.0010
3_{13}	2_{12}	7368.0946	0.0012
3_{03}	2_{02}	7462.7415	–0.0008
3_{22}	2_{21}	7466.3705	0.0034
3_{21}	2_{20}	7470.3113	–0.0019
3_{12}	2_{11}	7563.8611	–0.0007
3_{21}	3_{12}	9592.3437	–0.0029
3_{22}	3_{13}	9979.0447	0.0003
3_{13}	2_{02}	10532.1832	0.0006
4_{04}	3_{13}	6875.7319	0.0002
4_{14}	3_{13}	9822.4746	0.0012
4_{22}	4_{13}	9472.6553	0.0021
4_{04}	3_{03}	9945.1722	0.0001
4_{23}	3_{22}	9953.7799	0.0001
4_{32}	3_{31}	9956.0458	0.0013
4_{31}	3_{30}	9956.0983	–0.0029
4_{22}	3_{21}	9963.6260	–0.0022
4_{14}	3_{03}	12891.9123	–0.0015
4_{23}	4_{14}	10110.3494	–0.0013
5_{23}	5_{14}	9331.1178	0.0009
5_{05}	4_{14}	9476.4878	–0.0014
5_{24}	5_{15}	10274.8979	0.0014
5_{15}	4_{14}	12275.4726	0.0034
5_{05}	4_{04}	12423.2335	0.0026
5_{24}	4_{23}	12440.0128	–0.0022
5_{33}	4_{32}	12444.9471	0.0026
5_{32}	4_{31}	12445.1414	–0.0013
5_{23}	4_{22}	12459.6524	–0.0006
5_{14}	4_{13}	12601.1902	0.0009
5_{15}	4_{04}	15222.2116	0.0007
6_{06}	5_{15}	12096.9329	0.0018
6_{16}	5_{15}	14726.7709	–0.0018
6_{06}	5_{05}	14895.9095	–0.0016
6_{15}	5_{14}	15117.0352	–0.0001

[a] $\Delta\nu = \nu_{obs} - \nu_{calc}$ where ν_{calc} is calculated from the spectroscopic constants in Table 4.3.

Table 4.3: Spectroscopic parameters for the five isotopologues of the CH_2F_2–OCS complex.[a)]

Parameter	H_2CF_2–OCS	$H_2{}^{13}CF_2$–OCS	H_2CF_2–$O^{13}CS$	H_2CF_2–$OC^{34}S$
A / MHz	4505.6740(27)	4505.5025(35)	4489.7386(9)	4472.3799(18)
B / MHz	1277.0710(27)	1261.1336(12)	1271.9949(7)	1248.8408(9)
C / MHz	1212.0064(27)	1197.6235(9)	1206.2624(7)	1184.1930(7)
Δ_J / kHz	5.0345(86)	4.8726(94)	4.978(11)	4.841(13)
Δ_{JK} / kHz	13.386(48)	13.64(20)	13.15(6)	12.08(20)
Δ_K / kHz	21.72(52)	21.72 [b)]	21.72 [b)]	21.72 [b)]
δ_J / kHz	0.5906(43)	0.567(11)	0.598(15)	0.554(10)
δ_K / kHz	–59.3(14)	–59.3 [b)]	–59.3 [b)]	–59.3 [b)]
$\Delta\nu_{rms}$ / kHz [c)]	1.7	3.6	1.7	3.0
N [d)]	42	14	25	15
P_{cc} / u Å^2 [e)]	45.4604(9)	45.4592(4)	45.4563(2)	45.4539(3)

[a)] Errors given in parentheses are a priori errors reported by the SPFIT program.
[b)] Δ_K fixed at value obtained for the normal isotopic species
[c)] $\Delta\nu_{rms} = \left[\sum\left(\nu_{obs} - \nu_{calc}\right)^2 / N\right]^{1/2}$
[d)] N is the number of fitted transitions
[e)] P_{cc} is the planar moment = $0.5(I_a + I_b - I_c) = \sum_i m_i c_i^2$ (see Structure section for more detail on planar moment)

4.4. Dipole Moment

The overall dipole moment was experimentally determined for the DFM–OCS complex by measuring Stark coefficients for five lobes (see Chapter 1) from four rotational transitions. The M lobes were linear with no curvature observed in the $\Delta\nu$ versus E^2 Stark plots. The Stark plots with their transition quantum numbers and lobes are displayed in Figure 4.2. The program ASYSPEC[13] was utilized to predict the Stark coefficients, and take into account approximations that include up to second order terms in the electric field. Stark coefficients depend on the rotational constants and the relative proximity of energy levels. When an electric field is applied to a complex, the rotational

energy levels become perturbed, thus perturbing the rotational transitions and the extent to which the transitions are perturbed are described by the Stark coefficients. The Stark coefficients are the slope of the $\Delta\nu$ versus E^2 Stark plots, and a steeper slope indicates that the frequency change will be larger as the electric field is increased (also referred to as fast Stark effects). Due to an *ab* plane of symmetry it was expected to only obtain dipole moment components for μ_a and μ_b, while μ_c was expected to be zero. Therefore the μ_a and μ_b components were fit while fixing the μ_c dipole component at zero; and when the μ_c component was fitted, the value obtained was always zero within experimental uncertainty (or ~0.001D).

Each individual Stark measurement was then also fit with the QSTARK program,[14,15] which allows for exact determination of the Stark coefficients (rather than the second order perturbation approach of ASYSPEC). The frequency shifts at each electric field can be directly input into the QSTARK program. Since it takes into account higher order perturbation terms than the ASYSPEC/DIPOLE least squares fitting program (which accounts for terms only up to second order), QSTARK is a more reliable source for determination of experimental dipole moment components. Compared to the DIPOLE program, it was found that the dipole moment components (μ_a= 1.1385 (18) D and μ_b= 1.2371 (41) D) obtained from QSTARK were only ~0.05% different from DIPOLE.

The dipole moment of the DFM monomer is 1.96 (2) D[14] which is significantly higher than the experimental dipole moments obtained for the DFM-OCS dimer (see Table 4.4). Due to a dipole-dipole cancellation effect upon dimerization of DFM with OCS (as shown in Figure 4.3, μ_{OCS} = 0.7152 (2) D) we would expect a value for the

dimer to be lower than the monomer, and the dipole moment components (in Table 4.4) obtained from the *ab initio* calculations suggest that the experimental dipole moment components are in fact reasonable. If there was a perfect cancellation of the monomer dipole moments, then we would observe a total dipole moment of this theoretical complex of 1.245D, which is comparable to what is experimentally observed (see Table 4.4), but there will be a difference because the dipole moments are not exactly antiparallel to one another. The theoretical dipole moment results also demonstrate excellent agreement between Structure I and the experimental structure (not so well with Structure II), which is further evidence that this is the structure for this dimer that we observe experimentally. Table 4.4 summarizes the experimental dipole moment components for μ_a and μ_b from the least squares fitting program, QSTARK, and the *ab initio* theoretical results.

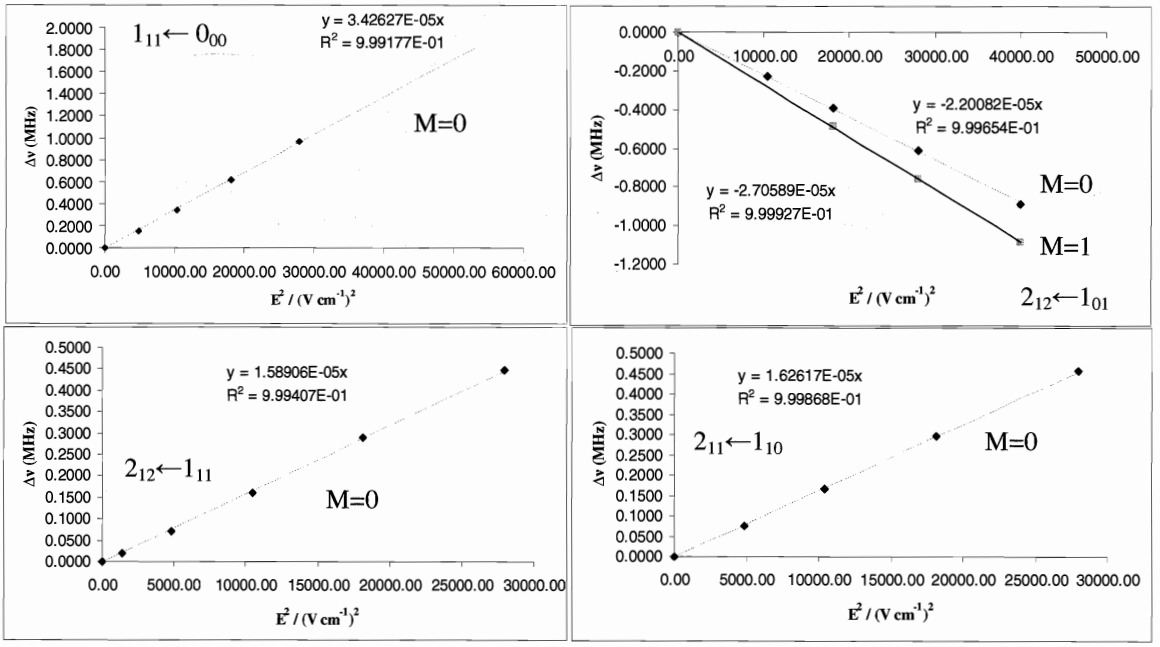

Figure 4.2: Stark plots obtained for 5 lobes at 4 frequencies for DFM–OCS. The lobes and transition quantum numbers are denoted on each plot.

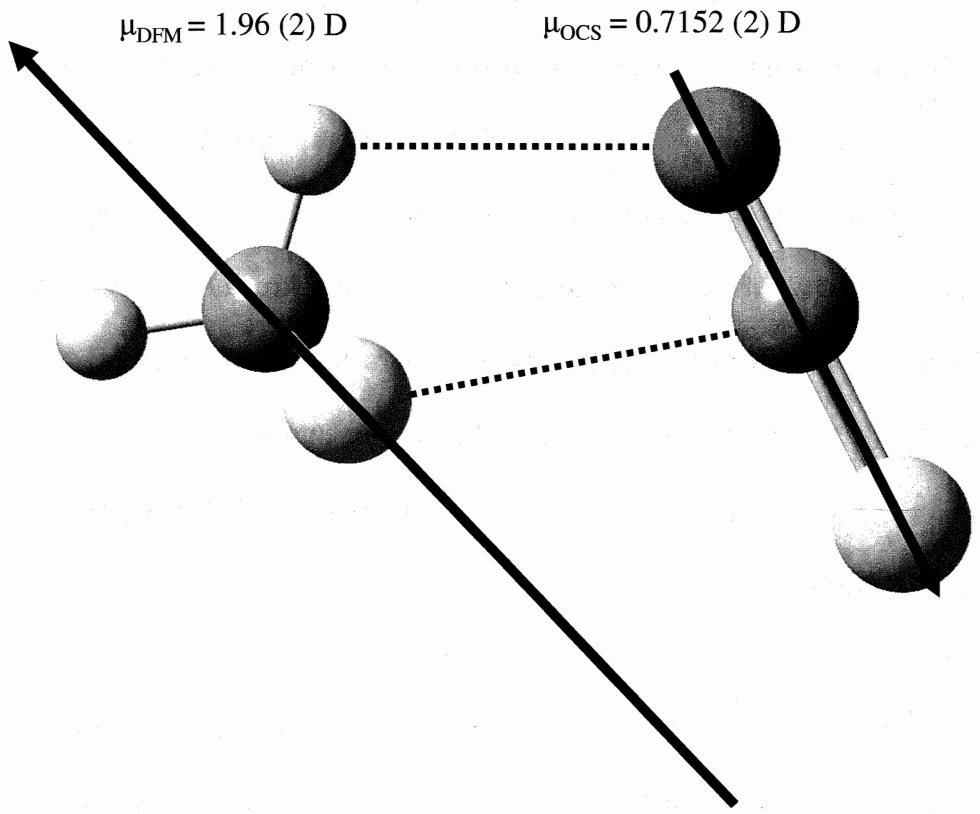

Figure 4.3:Approximate antiparallel arrangement of the monomer dipoles in order to establish the dipole-dipole and C–H···O weak bonding interactions.

Table 4.4: Dipole moment components for the CH_2F_2–OCS complex. The Experimental column shows the result of fitting the experimental data using the QSTARK and DIPOLE programs[14,15] while the Calculated column gives the values obtained from the MP2/6-311++G(2d,2p) calculation for structures I and II, respectively.

Parameter	Experimental	Calculated
	QSTARK, DIPOLE[d]	Structures I, II
μ_a / D	1.1385(18), 1.1342(16)	1.182, 1.284
μ_b / D	0.4839(62), 0.4921(57)	0.520, –1.201
μ_c / D[a]	0.00, 0.00	0.00, 0.00
μ_{total} / D	1.2371(41), 1.2365(27)	1.291, 1.759
N[b]	28, 5	–
Std. dev. / kHz[c]	0.0068	–

[a] μ_c was fixed at zero. Attempts to fit this parameter give values that are zero to within the reported uncertainty (to about ±0.001 D). See the text for further discussion.
[b] N is the number of Stark measurements included in the fit.
[c] The standard deviation of the fit (QSTARK only).
[d] DIPOLE is a least squares fitting program.

4.5. Structure

Calculating planar moments enables the determination of mass that exists out of a plane of symmetry, where P_{cc} denotes the mass out of the *ab* plane of symmetry for this system. The P_{cc} (where $P_{cc} = 0.5(I_a + I_b - I_c) = \Sigma_i m_i c_i^2$, and c_i is the coordinate of an atom from the center of mass on the c-axis, and m_i is the mass of that atom) value obtained from the rotational constants was approximately 45.5 u Å^2 for all the isotopomers, confirming that the two fluorine atoms are indeed out of the *ab* plane of symmetry (comparing to P_{aa} of DFM being 46.01 u Å^2)[16]. If the two hydrogen atoms were lying out of the plane (Structure II), then the P_{cc} would be closer to~1.6 u Å^2. Assuming that the DFM-OCS complex is arranged with C_s symmetry such that we obtain an *ab* plane of

symmetry, and that the monomer structures are fixed to their literature values,[17] then only three structural parameters need to be defined as shown in Figure 4.1. The STRFITQ fitting program was utilized to generate a structure by inputting the *ab initio* structure in terms of bond distances, bond angles, and dihedral angles. The program will then fit the moments of inertia of the isotopologues to the theoretical structure and generate a best fit from them. The three structural parameters fit are two bond angles (θ,ϕ) and a bond distance between the two carbon atoms ($R_{C\cdots C}$). Several inertial fits were carried out using the STRFITQ program of Schwendeman[18] in order to determine the best fit possible values for the three structural parameters of interest. Initial attempts to fit the structure were not performing well in locating some of the atoms in the difluoromethane subunit of this complex because no isotopic substitutions on that subunit had been obtained. The rotational spectrum of $H_2{}^{13}CF_2$ –OCS was finally obtained in natural abundance; however the rotational transitions were significantly weaker than anticipated with signal to noise ratios of about 20 in 5000-10000 gas pulses. This spectrum did however enable a more accurate determination of the structure by pinpointing the location of the carbon atom of the DFM subunit, and the C···C bond distance was obtained from STRFITQ to a high order of precision. The problem encountered was that there is no natural isotope of fluorine, and there were no commercially available sources for a deuterated sample of DFM (D_2CF_2 or $HDCF_2$) at the time of experimentation. The C···C–H bond angle (θ) would in turn be very flexible to a pivoting motion about the central carbon atom since neither the hydrogen or fluorine atoms could be exactly pinned down, and explains the large uncertainty in that bond angle (79 (2)° seen in Table 4.5). The location of the carbonyl sulfide subunit could be fixed due to the linear nature of the

molecule and a double isotopic substitution ($OC^{34}S$, and $O^{13}CS$) meant that the O=C···C bond angle (ϕ) could be obtained to a higher degree of uncertainty (64 (7)° from Table 4.5) when both angles and the bond distance were fit, but it was still necessary to perform multiple inertial fits in order to find a best fit value for this angle with a satisfactory uncertainty. Multiple fits allow for the determination of which parameters are sensitive to different moments of inertia, and if the exact locations of all the atoms are known, then multiple fits would not have to be performed. By alternating which moments of inertia (I_a, I_b, or I_c) are utilized in the inertial fit, it was possible to obtain best fit values for the three structural parameters, and the best fit values are summarized in Table 4.5, and the moments of inertia utilized to obtain these values are displayed for each of the fits. It is important to realize that even by manipulating the moments of inertia that are utilized in the fitting process, the structural parameters are not greatly perturbed. These three structural parameters are defined in Figure 4.1 for Structure I, and this is the experimental structure for DFM–OCS.

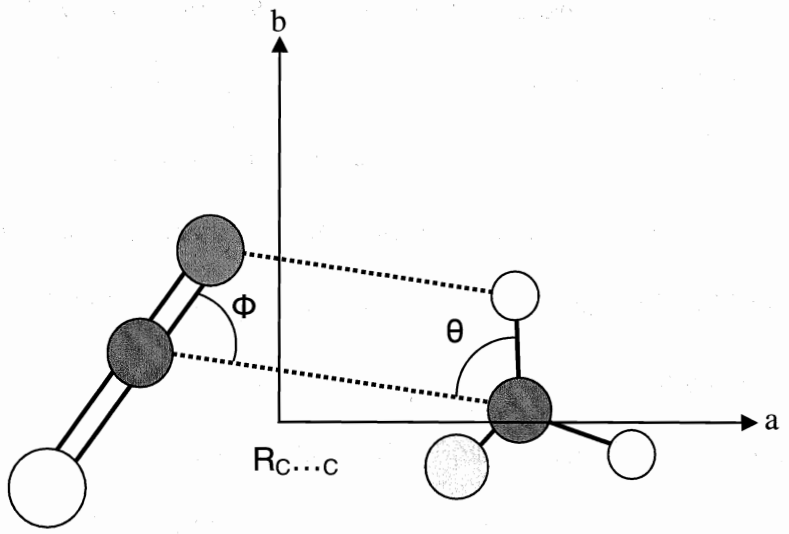

Figure 4.4: Final structure of DFM-OCS dimer with the origin of the a and b axes at the center of mass for the system.

Table 4.5: Structural parameters resulting from least-squares fits of moments of inertia for the isotopic species of CH_2F_2–OCS. See the text for an explanation of the different data sets included in this table.

	R / Å	θ / degrees	ϕ / degrees	Std. Dev. / u Å^2
All isotopic data [a]				
I_a, I_b, I_c	3.582(82)	79(10)	64(2)	0.4
I_a, I_b	3.586(16)	80.1(19)	64.9(4)	0.06
I_a, I_c	3.582(16)	79.0(19)	64.7(4)	0.05
I_b, I_c	3.578(9)	77.8(10)	65.2(2)	0.14
Best fit[b]	3.582(4)	79(2)	64.7(6)	–

[a] Fitting the H_3CF–OCS, $H_3{}^{13}CF$–OCS, H_3CF–$O^{13}CS$, H_3CF–$OC^{34}S$, and D_3CF–OCS moments of inertia.
[b] The best fit value is an attempt to incorporate all the values in the above table into a "best guess" value for each structural parameter.

The principal axis coordinates of the isotopically substituted atoms were determined from a Kraitchman single substitution calculation and compared to the inertial fit coordinates and the theoretical coordinates for Structures I and II in Table 4.6. There is very good agreement between the single substitution coordinates and both inertial and principal axis coordinates. Comparing the *ab initio* values with the experimentally determined coordinates for each of the singly substituted atoms in Table 4.6 proves once again that Structure I is the correct experimental structure for this complex. As a check the Kraitchman coordinates can be utilized to determine the C=S bond distance of OCS in the dimer independently. The experimental C=S bond length is (1.568(2) Å) and the agreement with the literature value is very good for the C=S bond length in the monomer (1.5651 Å)[19]. Another internal check of the system was to obtain the C···C=S bond angle from the Kraitchman fit, which was 114.7 (2)°, and this value corresponds within experimental uncertainty to the C···C=O bond angle (180° - 64.3° =

115.7°). There are also some non-zero values arising in the Kraitchman fits for the *c*-axis coordinates, but since there is an assumed *ab* plane of symmetry for this complex these coordinates must be zero. These small deviations from zero for the *c* coordinates could be due to a vibrational averaging effect with some small amplitude out of plane vibrational motions of these atoms. An important point is that the Kraitchman fits only provide the magnitude and not the sign of each coordinate, however, the inertial fits provide the appropriate signs which are attributed to a specific coordinate.

Table 4.6: Principal axis coordinates[a] derived from the Kraitchman single substitution calculations, inertial fit, and *ab initio* optimizations (in angstroms). Note that only the coordinate's magnitude, and not the sign, is determined from Kraitchman's equations.

	Principal axis coordinates[b] / Å		
	a	*b*	*c*
$H_2{}^{13}CF_2$	2.2427(7)	0.075(20)	0.035*i*(44)
	2.264(5)	0.083(12)	0.000
	2.1899; –2.0337	0.10096; –0.28879	0.000; 0.000
$O^{13}CS$	1.2609(12)	0.6378(24)	0.065*i*(24)
	–1.274(4)	0.642(2)	0.000
	–1.2172; 1.5624	0.6441; –0.6031	0.000; 0.000
$OC^{34}S$	2.1335(7)	0.6655(23)	0.060*i*(25)
	–2.150(4)	–0.655(5)	0.000
	–2.1257; 2.6032	–0.6316; 0.5662	0.000; 0.000

[a] Uncertainties obtained from Kraitchman coordinate calculation. [b] Three principle axis coordinate values for each isotopologue come from a Kraitchman substitution coordinate (first line), the inertial fit coordinate (second line), and the *ab initio* coordinates are displayed for Structures I and II respectively (in line 3).

4.6. Conclusions

Rotational spectra have been measured and fit to a semi-rigid Watson A-reduction Hamiltonian[15] for DFM–OCS, which was fit to a 1.7 kHz uncertainty for the normal isotopomer. From the P_{cc} value obtained for the mass out of the *ab* plane of symmetry, it was determined that the two fluorine atoms (Structure I), and not the two hydrogen atoms (Structure II), lie out of that plane. This evidence leads us to believe that Structure I is the correct experimental structure for this complex. The dipole moment components were determined with a least squares fitting program and QSTARK in order to determine the two dipole moment components with non-zero values (μ_a and μ_b). The third dipole moment component must be zero (μ_c) due to the symmetry plane in the DFM–OCS dimer, and all dipole moment components displayed excellent agreement with the *ab initio* theoretical values for Structure I (Table 4.1). The best fit inertial data and single substitution Kraitchman coordinates have pinned down the location of the singly substituted atoms are also comparable to the theoretical values obtained for Structure I. Future work will investigate the possibility of the existence of the higher energy Structure II in the gas expansion.

References

[1] Serafin, M.M.; Peebles, S.A. *J. Phys. Chem. A.* **2006**, *110*, 11938.

[2] Serafin, M.M.; Peebles, S.A. *J. Phys. Chem. A.* **2008**, *112*, 1473.

[3] Blanco, S.; López, J.C.; Lesarri, A.; Caminati, W.; Alonso, J.L. *Chem Phys Chem.* **2004**, *5*, 1779.

[4] Blanco, S.; Lopez, J. C.; Lesarri, A.; Alonso, J. L. *J. Mol. Struct.* **2002**, *612*, 255.

[5] Caminati, W.; Melandri, S.; Moreschini, P.; Favero, P. G. *Angew. Chem. (Intl. ed. Engl.)* **1999**, *38*, 2924.

[6] Caminati, W.; Melandri, S.; Schnell, M.; Banser, D.; Grabow, J.-U.; Alonso, J. L. *J. Mol. Struct.* **2005**, *742*, 87.

[7] Blanco, S.; Melandri, S.; Ottaviani, P.; Caminati, W. *J. Am. Chem. Soc.* **2007**, *129*, 2700.

[8] Frisch, M. J.; Trucks, G. W.; Schlegel, H. B.; Scuseria, G. E.; Robb, M. A.; Cheeseman, J. R.; Montgomery, J. A., Jr.; Vreven, T.; Kudin, K. N.; Burant, J. C.; Millam, J. M.; Iyengar, S. S.; Tomasi, J.; Barone, V.; Mennucci, B.; Cossi, M.; Scalmani, G.; Rega, N.; Petersson, G. A.; Nakatsuji, H.; Hada, M.; Ehara, M.; Toyota, K.; Fukuda, R.; Hasegawa, J.; Ishida, M.; Nakajima, T.; Honda, Y.; Kitao, O.; Nakai, H.; Klene, M.; Li, X.; Knox, J. E.; Hratchian, H. P.; Cross, J. B.; Bakken, V.; Adamo, C.; Jaramillo, J.; Gomperts, R.; Stratmann, R. E.; Yazyev, O.; Austin, A. J.; Cammi, R.; Pomelli, C.; Ochterski, J. W.; Ayala, P. Y.; Morokuma, K.; Voth, G. A.; Salvador, P.; Dannenberg, J. J.; Zakrzewski, V. G.; Dapprich, S.; Daniels, A. D.; Strain, M. C.; Farkas, O.; Malick, D. K.; Rabuck, A. D.; Raghavachari, K.; Foresman, J. B.; Ortiz, J. V.; Cui, Q.; Baboul, A. G.; Clifford, S.; Cioslowski, J.; Stefanov, B. B.; Liu, G.; Liashenko, A.; Piskorz, P.; Komaromi, I.; Martin, R. L.; Fox, D. J.; Keith, T.; Al-Laham, M. A.; Peng, C. Y.; Nanayakkara, A.; Challacombe, M.; Gill, P. M. W.; Johnson, B.; Chen, W.; Wong, M. W.; Gonzalez, C.; Pople, J. A.; Gaussian 03W, revision D.01; Gaussian, Inc.: Pittsburgh, PA, **2004**.

[9] Caminati, W., Melandri, S., Moreschini, P., Favero, P. G., *Agnew. Chem. Int. Ed.* **1999**, *38*(19), 2924.

[10] Blanco, S., Melandri, S., Ottaviani, P., Caminati, W. *Journal of the American Chemical Society*. **2007**, *129*, 2700.

[11] J.K.G. Watson, in J. Durig (Ed.), Vibrational Spectra and Structure, vol. 6, Elsevier, Amsterdam, **1997**, 1-89.

[12] Pickett, H.M. *J. Mol. Spec.* **1991**, *148*, 371.

[13] Stark coefficients were calculated using a modified version of the original ASYSPEC code: Beaudet, R. A. Ph.D. Thesis, Harvard University, Cambridge, MA, 1961.

[14] Kisiel, Z.; Kosarzewski, J.; Pietrewicz, B.A.; Pszczółkowski, L. *Chem. Phys. Lett.* **2000**, *325*, 523.

[15] Kisiel, Z. "PROSPE—Programs for Rotational Spectroscopy," *available at* http://info.ifpan.edu.pl/~kisiel/prospe.htm.

[16] Lide, David R., Jr. *J. Am. Chem. Soc.* **1952**, *74*, 3548-52.

[17] Harmony, M. D.; Laurie, V. W.; Kuczkowski, R. L.; Schwendeman, R. H.; Ramsay, D. A.; Lovas, F. J.; Lafferty, W. J.; Maki, A. J. *J. Phys. Chem. Ref. Data.* **1979**, *8*, 656(DFM) and 667(OCS).

[18] Schwendeman, R. H. In *Critical Evaluation of Chemical and Physical Structural Information*; Lide, D. R., Paul, M. A., Eds.; National Academy of Sciences: Washington, DC, **1974**. The STRFITQ program used in this work is the University of Michigan modified version of Schwendeman's original code.

[19] Harmony et. al. *J. Phys. Chem. Ref. Data.* **1979**, *8(3)*, 667.

Chapter 5

Rotational Spectra of Fluoromethane–Carbonyl Sulfide Dimer (FM–OCS)

5.1. Introduction

Rotational spectra have previously provided the rotational constants, dipole moments, and structures of trifluoromethane–carbonyl sulfide (TFM–OCS)[1] and difluoromethane–carbonyl sulfide (DFM–OCS)[2] weakly bound complexes. The main project in my master thesis involves the assignment of the rotational spectrum of the methyl fluoride–carbonyl sulfide (FM–OCS)[3] van der Waals complex using Fourier-transform microwave spectroscopy. In the weakly bound system comprised of methyl fluoride and carbonyl sulfide, there are three hydrogen atoms which may potentially form hydrogen bonding interactions with the oxygen atom in carbonyl sulfide. There is also a three fold axis of rotation that is possible about the C–F bond axis which gives rise to three equivalent structures which could lead to spectral splitting into *A* and *E* states due to internal rotation (see Chapter 1 for details).

Figure 5.1 displays the two lowest energy theoretical structures obtained from *ab initio* calculations at the MP2/6-311++G(2d,2p) level, and both structures are related to one another by an approximate 60° rotation about the C–F bond. So far the only complex in this series of complexes that has displayed internal rotation splitting that have been unambiguously assigned was trifluoromethane–carbon dioxide (TFM–CO_2) complex[4].

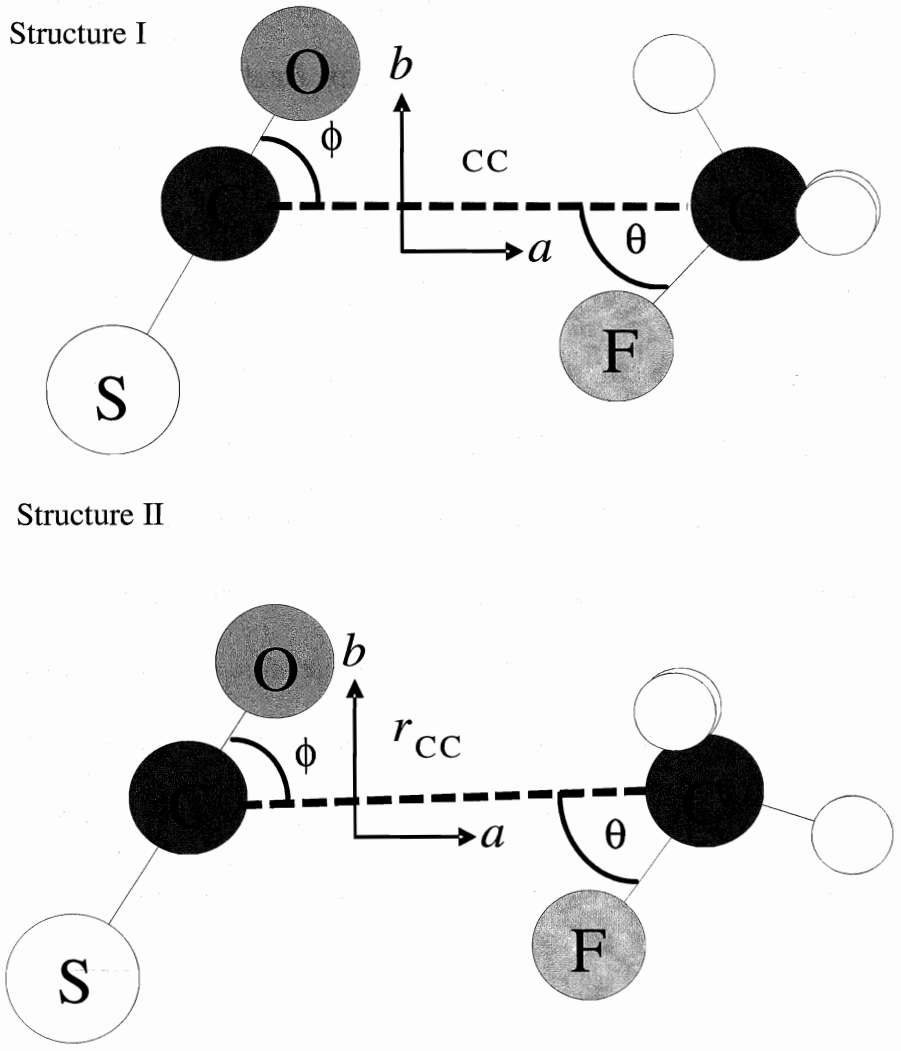

Figure 5.1: Two minimum energy configurations of FM–OCS. Structure II is calculated to be 0.5 cm^{-1} higher in energy than Structure I.

In this study, rotational spectra have been collected for the ground vibrational state of FM–OCS to acquire rotational constants, centrifugal distortion constants, and/or any indication of large amplitude motions of the FM subunit. If spectral complications are observed, they could most likely be attributed to internal rotation effects (see Chapter 1 for details). If the barrier to rotation of FM is very small, the *A* and *E* state transitions will be very widely separated in the spectrum. The smaller the barrier is, the larger the splitting will become causing transitions to split over several gigahertz and out of the

accessible spectral region. The TFM–CO_2 complex[5] displayed an internal rotation barrier of 30 cm^{-1} and the *A* and *E*- states were split by approximately 0.5-2 MHz. The rotation of TFM subunit should require more energy for rotation than the FM subunit because there are three fluorine atoms (in TFM) which are more massive than the hydrogen atoms in FM. Therefore, it is sensible to expect a much smaller internal rotation barrier in FM–OCS (predicted to be 0.5 cm^{-1} from the relative energy difference between the two *ab initio* Structures I and II at the MP2/6-311++G(2d,2p) level).

In the complex of trifluoromethane with methyl fluoride (TFM–FM)[6] it was previously observed that the minimum energy structures had multiple C–H···F interactions (shown in Figure 5.2). In this complex, there were indications that both the methyl fluoride and trifluoromethane subunits exhibited internal rotation. The barrier to rotation was obtained for the internal rotation of the trifluoromethane subunit (V_3=0.840 kJ/mol[6]) and both *A* and *E*-state transitions were observed for this motion.

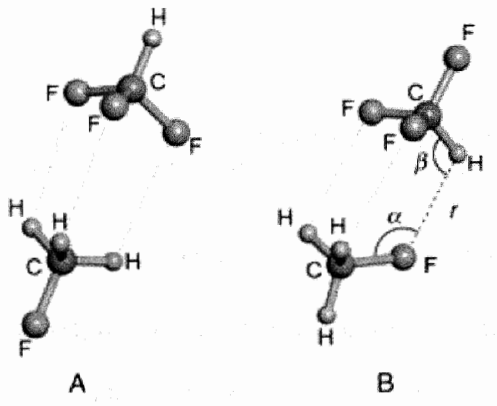

Figure 5.2: Two minimum energy configurations of TFM–FM showing multiple C–H···F interactions.

However, it was determined that the barrier to rotation of the methyl fluoride subunit ($V_3 \approx 0.36$ kJ/mol) was considerably lower than the trifluoromethane subunit and the

E-state transitions were shifted out of the accessible spectral region due to the much larger *A* and *E* splitting. This previous study shows that even though internal rotation splittings may occur in the spectrum, the *E*-state transitions may not be easily obtained if the barrier to rotation is small and so we might expect similar problems in our present study.

5.2. *Ab initio* Calculations

Gaussian 03[7] was utilized to obtain two low energy conformations of FM–OCS at the MP2/6-311++G(2d,2p) level which are shown in Fig. 5.1, and denoted as Structures I and II. Structures I and II are related to one another by an approximately 60° rotation about the C–F bond and the energy difference between these two structures was utilized to calculate a very crude barrier to internal rotation ($0.5 cm^{-1}$). An example of the Gaussian 03 output file is displayed below, and the theoretical equilibrium energy (in Hartree) is highlighted in the output:

```
The integrals were generated   1 times.
 ANorm=     0.1130741979D+01
 E2 =     -0.8891831265D+00 EUMP2 =     -0.65029811946547E+03
Leave Link906 at Tue Oct 03 14:53:06 2006, MaxMem=6291456cpu:189.0
 (Enter C:\G03W\l1002.exe)
Minotr:  Closed-shell wavefunction.
```

Structure I is lower in energy by approximately $0.5 cm^{-1}$ compared to structure II, therefore one can conclude that a flat potential energy surface exists for internal rotation between the two structures. The coordinates obtained for the two minimum energy structures indicate that there is a difference in the distance of 0.12 Å between the two carbon atoms (see Table 5.1 for r_{CC}), which suggests that the internal rotation axis does not coincide exactly with the C_3 axis of methyl fluoride.

The theoretical rotational constants were obtained from the Gaussian 03 output file. An example of the output file is displayed below with highlighted rotational constants:

```
---------------------------------------------------------------------

 Center     Atomic      Atomic              Coordinates (Angstroms)
 Number     Number       Type              X           Y           Z
 ---------------------------------------------------------------------
    1          1             0       -1.935821   -1.736216    0.888201
    2          6             0       -1.489251   -2.167789    0.000000
    3          1             0       -1.606720   -3.245534    0.000000
    4          9             0       -0.125236   -1.872249    0.000000
    5          1             0       -1.935821   -1.736216   -0.888201
    6          8             0       -1.159297    0.984196    0.000000
    7          6             0        0.000000    1.141243    0.000000
    8         16             0        1.550960    1.365870    0.000000
 ---------------------------------------------------------------------
 Rotational constants (GHZ):      7.2671601      1.6901042    1.3831413
 Leave Link  202 at Tue Oct 03 14:56:57 2006, MaxMem=    6291456 cpu:    0.0
 (Enter C:\G03W\l601.exe)
 Copying SCF densities to generalized density rwf, ISCF=0 IROHF=0.
```

The rotational constants displayed in Table 5.1 were used to predict the location of rotational transitions for both structures using RRFIT. Theoretical dipole moment components are also obtained from the Gaussian output file as shown below for structure I (dipole moment components highlighted):

```
Sum of Mulliken charges=   0.00000
 Electronic spatial extent (au):  <R**2>=    776.7064
 Charge=      0.0000 electrons
 Dipole moment (field-independent basis, Debye):
    X=     -1.0929    Y=     -0.4601    Z=      0.0000  Tot=      1.1858
 Quadrupole moment (field-independent basis, Debye-Ang):
   XX=    -33.1006   YY=    -34.1586   ZZ=    -35.7147
   XY=      5.0930   XZ=      0.0000   YZ=      0.0000
 Traceless Quadrupole moment (field-independent basis, Debye-Ang):
   XX=      1.2241   YY=      0.1660   ZZ=     -1.3901
   XY=      5.0930   XZ=      0.0000   YZ=      0.0000
 Octapole moment (field-independent basis, Debye-Ang**2):
  XXX=     -1.1177  YYY=    -19.8086  ZZZ=      0.0000  XYY=    -10.8973
  XXY=     -8.8083  XXZ=      0.0000  XZZ=     -3.5481  YZZ=     -4.0765
  YYZ=      0.0000  XYZ=      0.0000
 Hexadecapole moment (field-independent basis, Debye-Ang**3):
 XXXX=   -352.6984 YYYY=   -552.3333 ZZZZ=    -45.2412 XXXY=   -122.1001
 XXXZ=      0.0000 YYYX=   -120.9702 YYYZ=      0.0000 ZZZX=      0.0000
 ZZZY=      0.0000 XXYY=   -144.5756 XXZZ=    -69.7093 YYZZ=   -105.7247
 XXYZ=      0.0000 YYXZ=      0.0000 ZZXY=    -47.9642
```

The *ab initio* calculations utilized have been used in previous complexes[1,2,3,] and have shown to provide rotational constants to within 5% of experimental error. Table 5.1 contains the theoretical rotational constants, distance between the two carbon atoms (r_{CC}), and the intermolecular bond angles (θ and ϕ which are the F–C···C and O–C···C angles respectively – see Figure 5.1).

Table 5.1: *Ab initio* structural parameters and rotational constants for low energy structures I and II obtained at the MP2/6-311++G(2d,2p) level of calculation.

Parameter	Structure I	Structure II
r_{CC} / Å	3.75	3.63
θ / degrees	48.4	53.5
ϕ / degrees	61.1	58.1
A / MHz	7121	7267
B / MHz	1661	1690
C / MHz	1358	1383
Relative energy / cm^{-1}	0	0.5

5.3. Spectra

As mentioned in the previous section, the rotational constants obtained from Gaussian were used to predict the rotational spectra for both low energy structures depicted in Figure 5.1 with the rigid rotor program RRFIT[8]. All that is required to generate an input file for RRFIT are the theoretical rotational constants and the region of the spectrum accessible by our spectrometer and is displayed in the two respective highlighted sections as shown below:

```
OCS-FM
      7267.160       1690.104     1383.141        Rot. const. A, B, C

      5000.0         18000.0                      Predicted spectrum range (5-18 GHz)
  0    0    0    9    4    1    0
```

The output file contains the spectrum for the input rotational constants, within the specified region of the spectrum, and assigns quantum numbers to all the transitions in the output. The transition frequencies are also calculated and displayed for each transition, followed by the dependence of the transition frequencies on the rotational constants. An example of the RRFIT program output file for structure I is shown below:

```
1     OCS-FM
                                                    Expectation value differences
                                                    (derivatives with respect to)
                                                      A          B          C
          B type transitions for J =  1

  1   1   0     1   0   1       5763.390        1.00000    0.00000   -1.00000
  1   1   1     0   0   0       8480.210        1.00000    0.00000    1.00000
    C type transitions for J =  1
  1   1   1     1   0   1       5460.831        1.00000   -1.00000    0.00000
  1   1   0     0   0   0       8782.769        1.00000    1.00000    0.00000
    A type transitions for J =  2
  2   0   2     1   0   1       6026.531        0.00218    1.91813    2.07969
  2   1   2     1   1   1       5736.199        0.00000    1.00000    3.00000
  2   1   1     1   1   0       6341.317        0.00000    3.00000    1.00000
```

This particular output file contains the entire predicted spectrum between 5-18GHz, but only the first seven predicted transitions are shown above. The *a*-type spectrum could be readily assigned from these predictions, due to the high intensity of these transitions, providing precise determination of the rotational constants B and C. There were several other transitions in the regions where the *b*-type transitions were predicted, which made it very difficult to unambiguously assign these transitions. The $1_{11} \leftarrow 0_{00}$ *b*-type transition was finally located (after several months and several failed attempts) approximately 470 MHz from where it was predicted (it was finally identified using Stark effect measurements). It had an order of magnitude lower intensity than expected (within a region littered with rotational transitions that did not fit the standard Watson *A*-reduction Hamiltonian). The unassigned transitions could belong to complexes other than FM–OCS, such as water dimers, FM trimers, etc. Although it is also possible that some

of the transitions could be the *E*-state transitions that arise due to internal rotation, but the *E*-state spectrum has not unambiguously been assigned to date.

The program SPFIT[9] was used to fit the observed spectrum to a Watson *A*-reduction Hamiltonian. The input file for this program requires a slightly more complex two file input format. The .par file contains the parameters which need to be fit (including rotational constants and distortion constants), and the number of transitions that need to be fit (highlighted below). The rotational constants (*A*, *B*, and *C*) and the distortion constants (DeltaJ, DeltaJK, etc.) are also fit with this program. An example of the .par input file is shown below for the normal isotopologue:

```
OCS-Fluoromethane normal                                  Thu Apr 05 13:24:19 2007
   7   30   50    0    0.0000E+000    1.0000E+006    1.0000E+000 1.0000000000
a  1  1  0  8  0  1  1  1    0  1 0
        10000  7.322349987698137E+003 1.00000000E+000 /A
        20000  1.655608164696833E+003 1.00000000E+000 /B
        30000  1.348766444902532E+003 1.00000000E+000 /C
          200 -5.251496331347772E-003 1.00000000E+000 /-DeltaJ
         1100  2.410724001226854E-002 1.00000000E+000 /-DeltaJK
        40100 -1.272825114529615E-003 1.00000000E+000 /-deltaJ
        41000  2.283868867908306E-001 1.00000000E+000 /-delta_K
```

The second of the two input files that needs to be created is the .lin file. These files contain the quantum numbers for the transitions that have been located in the spectrum with the transition frequency, and are continually updated during a search. An example of the .lin file for the normal isotopomer of this complex is shown below with the transition quantum numbers input first (in the format $J'_{KaKc} \leftarrow J''_{KaKc}$), the measured frequency second, and the uncertainty in the measurement last (all in MHz):

```
2  1  2  1  1  1                    5701.8784     0.004
1  1  0  1  0  1                    5973.8515     0.004
2  0  2  1  0  1                    5996.4583     0.004
2  1  1  2  0  2                    6292.8750     0.004
2  1  1  1  1  0                    6315.4791     0.004
3  1  2  3  0  3                    6793.7636     0.004
4  0  4  3  1  3                    6942.7631     0.004
```

Once a frequency is measured it is entered into the .lin file followed by a modification to the .par file and SPFIT program is rerun; the program will generate an output file, an example of which is shown below (excluding previous iterations and correlation parameters):

```
END OF ITERATION  2 OLD, NEW RMS ERROR=         1.66495          0.76202

EXP.FREQ.-CALC. FREQ.- DIFF.-EXP.ERR.-EST.ERR.-AVG CALC.FREQ.-DIFF.- WT.

    1:   2  1  2  1  1  1  5701.87840  5701.87628  0.00212 0.00400 0.00103
    2:   1  1  0  1  0  1  5973.85150  5973.85297 -0.00147 0.00400 0.00144
    3:   2  0  2  1  0  1  5996.45830  5996.45808  0.00022 0.00400 0.00110
    4:   2  1  1  2  0  2  6292.87500  6292.87113  0.00387 0.00400 0.00160
    5:   2  1  1  1  1  0  6315.47910  6315.47624  0.00286 0.00400 0.00129
    6:   3  1  2  3  0  3  6793.76360  6793.76070  0.00290 0.00400 0.00194
    7:   4  0  4  3  1  3  6942.76310  6942.76238  0.00072 0.00400 0.00216
    8:   4  1  3  4  0  4  7502.18030  7502.18275 -0.00245 0.00400 0.00219
    9:   5  1  4  5  0  5  8449.36370  8449.36528 -0.00158 0.00400 0.00213
   10:   3  1  3  2  1  2  8545.14300  8545.14860 -0.00560 0.00400 0.00115
   11:   1  1  1  0  0  0  8671.37400  8671.37529 -0.00129 0.00400 0.00149
   12:   3  0  3  2  0  2  8964.20310  8964.20814 -0.00504 0.00400 0.00124
   13:   3  2  2  2  2  1  9013.13960  9013.13981 -0.00021 0.00400 0.00152
   14:   3  2  1  2  2  0  9061.48050  9061.47770  0.00280 0.00400 0.00152
   15:   3  1  2  2  1  1  9465.10040  9465.09771  0.00269 0.00400 0.00138
   16:   6  1  5  6  0  6  9667.89510  9667.89548 -0.00038 0.00400 0.00359
   17:   5  0  5  4  1  4 10345.73120 10345.73640 -0.00567 0.00400 0.00198
   18:   2  1  2  1  0  1 11368.89510 11368.89894 -0.00384 0.00400 0.00175
   19:   4  1  4  3  1  3 11379.64760 11379.64341  0.00419 0.00400 0.00106
   20:   4  0  4  3  0  3 11896.14380 11896.14370  0.00010 0.00400 0.00112
   21:   4  2  3  3  2  2 12007.52140 12007.52157 -0.00017 0.00400 0.00283
   22:   4  3  2  3  3  1 12041.23730 12041.24025 -0.00295 0.00400 0.00245
   23:   4  3  1  3  3  0 12043.03310 12043.03259  0.00051 0.00400 0.00245
   24:   4  2  2  3  2  1 12127.50140 12127.50261 -0.00121 0.00400 0.00287
   25:   4  1  3  3  1  2 12604.57060 12604.56576  0.00484 0.00400 0.00111
   26:   6  0  6  5  1  5 13760.21090 13760.21290 -0.00200 0.00400 0.00295
   27:   3  1  3  2  0  2 13917.58700 13917.58946 -0.00246 0.00400 0.00210
   28:   5  1  5  4  1  4 14203.11600 14203.11761 -0.00161 0.00400 0.00177
   29:   5  0  5  4  0  4 14782.62160 14782.61790  0.00370 0.00400 0.00161
   30:   5  1  4  4  1  3 15729.80600 15729.80043  0.00557 0.00400 0.00185

NORMALIZED DIAGONAL:
    1  1.00000E+000    2  9.95875E-001    3  9.24529E-001    4  3.42669E-001
5  7.96797E-001    6  2.96425E-001
    7  2.93318E-002
MARQUARDT PARAMETER = 0, TRUST EXPANSION = 1.00
                                NEW PARAMETER (EST. ERROR) -- CHANGE THIS
ITERATION
   1          10000          A       7322.57531(146)          0.00000
   2          20000          B        1655.6314( 34)          -0.0000
   3          30000          C        1348.7426( 33)           0.0000
   4            200    -DeltaJ          -5.3319(234)E-03        0.0000E-03
   5           1100   -DeltaJK         0.024741(136)         -0.000000
   6          40100    -deltaJ          -1.2636( 51)E-03        0.0000E-03
   7          41000   -delta_K         -0.01209(165)           0.00000
 MICROWAVE AVG =       -0.000028 MHz, IR AVG =         0.00000
 MICROWAVE RMS =        0.003039 MHz, IR RMS =         0.00000
```

This is where the experimental rotational constants, distortion constants, and root mean square (MICROWAVE RMS) are obtained. This parameter is defined by equation (1) and is a measure of how well the transitions fit to the quantum mechanical Hamiltonian of the rotational energy states. N is the number of measured transitions.

(1) $$\Delta\nu_{rms} = \left[\frac{\Sigma(\nu_{obs} - \nu_{calc})^2}{N}\right]^{\frac{1}{2}}$$

The spectrum should fit to within the measurement uncertainty of the instrument and so $\Delta\nu_{rms}$ should be at or below 4 kHz. The program will also specify the observed minus calculated (obs - calc) values so that it is easier to determine which transitions are not fitting the Hamiltonian. If this occurs, the transition needs to be remeasured, or a different transition needs to be located that will fit. The rotational transitions for the normal isotopomer obtained in the accessible region of the spectrum are displayed in Table 5.2. The rotational constants and spectral parameters obtained by fitting the rotational transitions to a Watson *A*-reduction Hamiltonian for all the measured isotopolgues are displayed in Table 5.3. SPFIT utilizes a semirigid Hamiltonian with no internal rotation effects accounted for to fit the rotational transitions, which is an indication that the *A*-state transitions are assigned, because the *E*-state transitions are not expected to fit well to this type of Hamiltonian. The *A*-state transitions tend to behave as if the rotational transitions exist in the ground vibrational state, so the *A*-state spectrum of a complex exhibiting internal rotation can still be fit with this type of Hamiltonian. The *E*-state transitions are the torsionally excited rotational transitions and do not behave in a similar fashion to the *A*-state transitions, and need to be assigned with a different Hamiltonian (see XIAM fitting in Cyclopropylmethylgermane chapter for Hamiltonian

details). A broad region of the spectrum was searched (5.5-9.7 GHz) in order to locate the *b*-type spectrum and *E*-state transitions, and several transitions were measured that required both methyl fluoride and carbonyl sulfide in the sample. It is possible that some of these transitions may be unassigned *E*-state transitions or belong to torsionally excited states (which are very likely in this complex due to the relatively small theoretical barrier to rotation obtained from *ab initio* calculations).

Table 5.2: Rotational transitions for the normal isotopologue of FM-OCS complex.

$J'_{K_aK_c} \leftarrow J''_{K_aK_c}$		ν_{obs} / MHz	$\Delta\nu$ / MHz
2_{12}	1_{11}	5701.8784	0.0021
1_{10}	1_{01}	5973.8515	–0.0015
2_{02}	1_{01}	5996.4583	0.0002
2_{11}	2_{02}	6292.8750	0.0039
2_{11}	1_{10}	6315.4791	0.0029
3_{12}	3_{03}	6793.7636	0.0029
4_{04}	3_{13}	6942.7631	0.0007
4_{13}	4_{04}	7502.1803	–0.0025
5_{14}	5_{05}	8449.3637	–0.0016
3_{13}	2_{12}	8545.1430	–0.0056
1_{11}	0_{00}	8671.3740	–0.0013
3_{03}	2_{02}	8964.2031	–0.0050
3_{22}	2_{21}	9013.1396	–0.0002
3_{21}	2_{20}	9061.4805	0.0028
3_{12}	2_{11}	9465.1004	0.0027
6_{15}	6_{06}	9667.8951	–0.0004
5_{05}	4_{14}	10345.7312	–0.0057
2_{12}	1_{01}	11368.8951	–0.0038
4_{14}	3_{13}	11379.6476	0.0042
4_{04}	3_{03}	11896.1438	0.0001
4_{23}	3_{22}	12007.5214	–0.0002
4_{32}	3_{31}	12041.2373	–0.0030
4_{31}	3_{30}	12043.0331	0.0005
4_{22}	3_{21}	12127.5014	–0.0012
4_{13}	3_{12}	12604.5706	0.0048
6_{06}	5_{15}	13760.2109	–0.0020
3_{13}	2_{02}	13917.5870	–0.0025
5_{15}	4_{14}	14203.1160	–0.0016
5_{05}	4_{04}	14782.6216	0.0037
5_{14}	4_{13}	15729.8060	0.0056

Table 5.3: Spectral parameters obtained for the five isotopologues of FM-OCS.

Parameter	H_3CF–OCS	$H_3{}^{13}CF$–OCS	H_3CF–$O^{13}CS$	H_3CF–$OC^{34}S$	D_3CF–OCS
A / MHz	7322.5753(15)	7322.1689(16)	7279.4636(19)	7253.5315(27)	7166.7556(16)
B / MHz	1655.6314(34)	1614.9628(18)	1651.0414(8)	1618.7493(9)	1513.9106(20)
C / MHz	1348.7426(33)	1321.6426(17)	1344.2144(6)	1321.8642(7)	1252.0266(19)
Δ_J / kHz	5.332(23)	5.020(14)	5.294(11)	5.168(11)	4.353(14)
Δ_{JK} / kHz	–24.74(14)	–23.98(9)	–23.91(15)	–25.61(33)	–2.87(9)
δ_J / kHz	1.264(5)	1.186(8)	1.300(9)	1.240(10)	1.022(8)
δ_K / kHz	12.1(17)	11.7(8)	12.1[b]	12.1[b]	14.0(9)
$\Delta\nu_{rms}$ / kHz [c]	3.0	2.3	3.2	3.6	3.4
N[d]	30	26	20	16	27
P_{cc} / u Å^2 [e]	–0.21938(15)	–0.21563(6)	–0.2212(1)	–0.2232(1)	0.34595(8)

5.4. Planar Moments

Since the complex has an *ab* plane of symmetry with two hydrogen atoms lying out of that plane (regardless of whether structure I or II is taken into consideration), the planar moment should be similar to the P_{bb} of methyl fluoride monomer (P_{bb}=1.62656 u Å^2)[10]. The planar moment calculated from the experimental rotational constants (P_{cc}= -0.21938 (15) u Å^2) is non physical because:

(2) $$P_{xx} = 0.5(-I_x + I_y + I_z) = \Sigma m_i x_i^2$$

I is the moment of inertia about a particular axis, m is the mass of the particle, and r is the distance of the particle from the axis. This equation therefore does not allow for a negative value to be obtained for P_{cc} unless there is a contamination of the moments of inertia due to large amplitude motions. The planar moments obtained for each isotopologue of FM-OCS complex (displayed in Table 5.3) all gave non-physical values of approximately -0.22 u Å^2, except for D_3CF-OCS (which still displayed a much lower P_{cc} of 0.34595(8) u Å^2 compared to the expected value of 3.23795 u Å^2 for the monomer species)[8]. It should also be noted that the Δ_{JK} distortion constant for the deuterated

isotopologue is an order of magnitude lower than the Δ_{JK} values obtained for the other isopologues. This difference can be attributed to a significant change in the internal motion dynamics of the system upon deuteration, and point to the fact that there may be some internal motion of the methyl fluoride subunit even though no *E*-state transitions were measured. The parameters obtained (in Table 5.3) are consistent among all the isotopologues that do not contain deuterium atoms and serve to confirm the quality of our assignment.

5.5. Dipole Moment

The conventional approach of measuring the experimental dipole moment from Stark coefficients (as discussed in Chapter 4) utilizes second order perturbation theory. However, if there are close lying rotational energy levels, these energy levels will be additionally perturbed due to their close proximity, and this effect is not taken into account in second order perturbation theory. An indication of transitions with near proximity to other close lying energy levels is a deviation from linearity in the Δv versus E^2 Stark plots which will manifest as curvature for a specific lobe of that transition. One such transition was the $2_{02} \leftarrow 1_{01}$ transition where the $|M|=0$ lobe shows clear curvature compared to $|M|=1$ lobe. This type of curvature requires special treatment, where each individual frequency shift that occurred at a given field is input to the QSTARK[11] program.

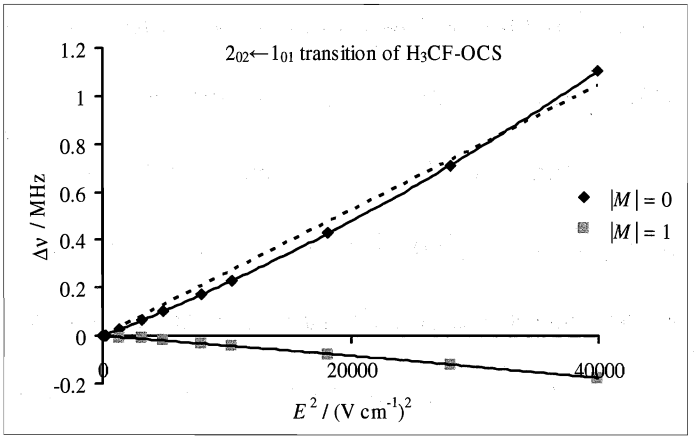

Figure 5.3: Stark effect plot for the $2_{02} \leftarrow 1_{01}$ rotational transition for the normal isotopologue of FM-OCS complex.

This program was used to fit a total of 11|M| components from seven different rotational transitions and experimentally determined rotational constants because it has the capability of separately calculating exactly how energy levels get perturbed in an electric field, providing accurate dipole moment components (details about Stark effects are explained in Chapter 1 and QSTARK is explained in Chapter 3). Some other transitions that behaved in a linear fashion (in terms of frequency shift vs. E^2) are displayed in Figure 5.4. Later inspection of the rotational energy levels revealed that the 2_{02} level was very close in energy to the 1_{10} level, which explains the curvature in Figure 5.3 (see also Figure 5.5 for another transition involving the 2_{02} level)

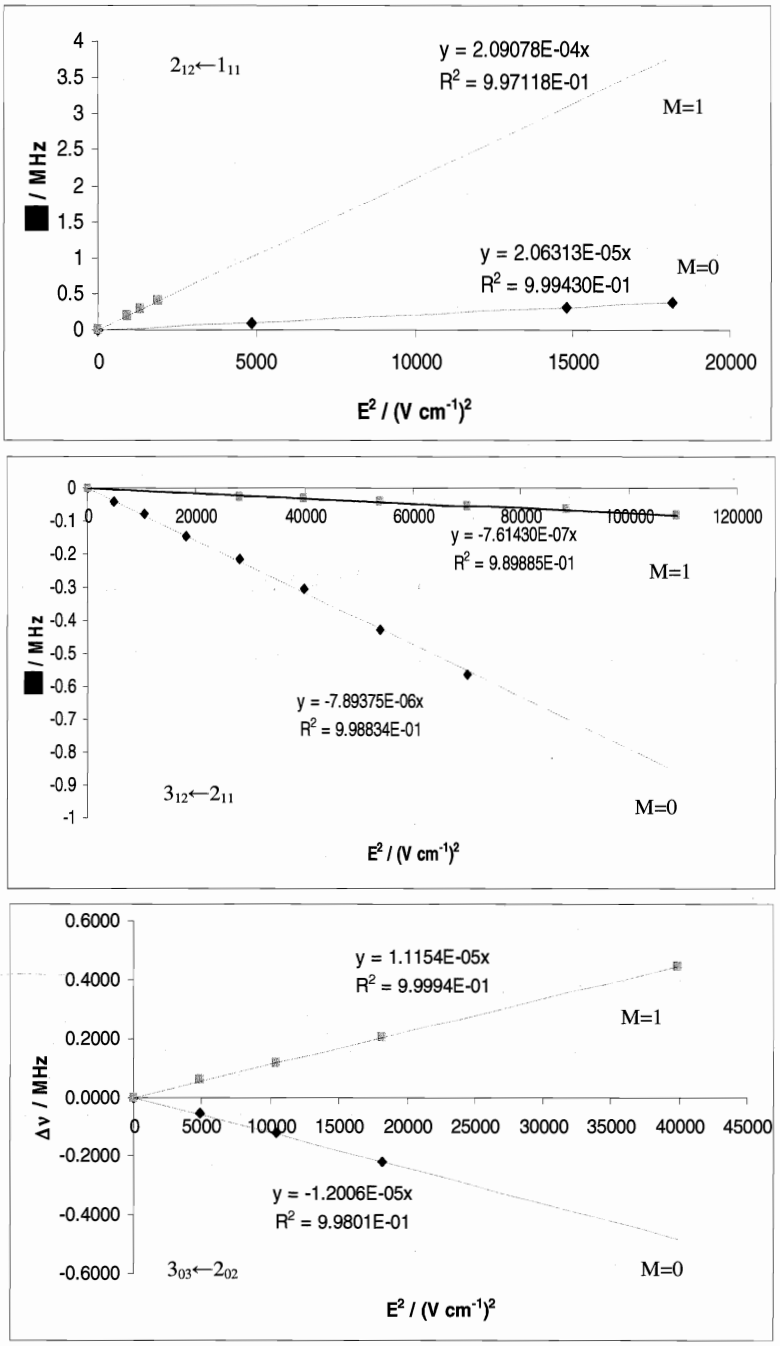

Figure 5.4: Stark plots obtained showing 6 lobes for three different rotational transitions that did not deviate from linearity.

The QSTARK program utilizes an input file that requires the rotational constants and distortion constants (acquired from the SPFIT program) as shown below:

```
FM-OCS with QSTARK

----------------------------------------
Fit frequencies(1) or differences(2) =  1
spin of nucleus 1 (units of 1/2)     =  0
spin of nucleus 2 (units of 1/2)     =  0
Number of iterations                 =  5
Excess in F and J over value in data =  2
Dump options (0,1,2)                 =  0
Freq. contributions options (0,1,2)  =  0
Number of transitions                = 61
----------------------------------------
    A        = 0      7322.5753
    B        = 0      1655.6314
    C        = 0      1348.7426
    DJ       = 0         .00533
    DJK      = 0       -0.02474
    DK       = 0          .000000000000
    dJ       = 0        0.001264000000
    dK       = 0        0.012090000000
```

followed by the transition quantum numbers, which Stark lobe is being fit, the Stark shift observed, and the applied electric field (V/cm) as shown below (for the $2_{12}\leftarrow1_{01}$ |M|=1 lobe):

```
J'KaKc  JKaKc
2 1 2  1 0 1    4 2 2 2    11368.9653    134.79 1
2 1 2  1 0 1    4 2 2 2    11369.0004    167.30 1
2 1 2  1 0 1    4 2 2 2    11369.0454    199.81 1
2 1 2  1 0 1    4 2 2 2    11369.0961    232.32 1
2 1 2  1 0 1    4 2 2 2    11369.1535    264.83 1
2 1 2  1 0 1    4 2 2 2    11369.2223    297.33 1
2 1 2  1 0 1    4 2 2 2    11369.2979    329.83 1
```

Figure 5.5 shows another transition involving the 2_{02} rotational energy level, and it is evident that this transition is perturbed by close lying energy levels in an electric field.

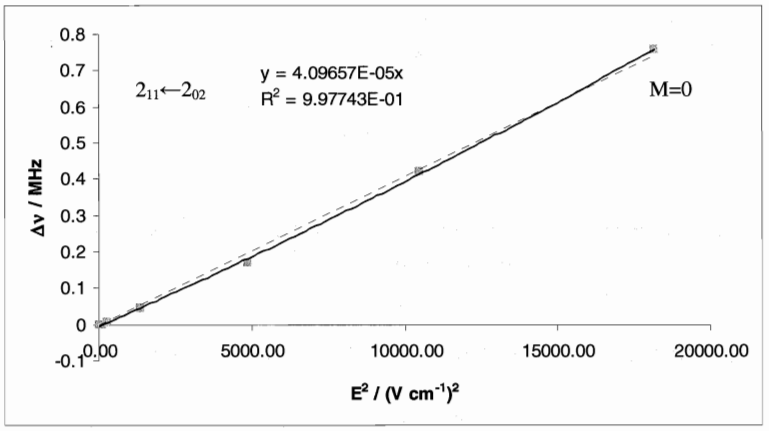

Figure 5.5: A second transition which also displays curvature in the Stark plots.

A representative of the output file generated by QSTARK showing the last iteration in the fitting cycle below:

```
  1. 212 101  4020    0.0  11368.90370  0.00468 11368.8990   0.0000      0.00
  2. 212 101  4020  102.3  11368.72190  0.00463 11368.7173 102.2600  10457.11
  3. 212 101  4020  134.8  11368.58630  0.00301 11368.5833 134.7900  18168.34
  4. 212 101  4020  167.3  11368.41700  0.00430 11368.4127 167.3000  27989.29
  5. 212 101  4020  199.8  11368.19750 -0.00797 11368.2055 199.8100  39924.04

   Standard deviation =       0.007349

ITERATION NO = 5 CONSTANTS, deviations and changes:

     Mu.a     =          1.091024661 +-      0.001532036           0.000000000
     Mu.b     =          0.442528786 +-      0.001043685           0.000000000

 FINAL RESULTS OF LEAST SQUARES FITTING PROCEDURE
 ================================================

 FITTED CONSTANTS:

 A     /MHz        7322.575300000000424 1:Xab /MHz           0.
 B     /MHz        1655.631399999999985 1:XJ.a/kHz           0.
 C     /MHz        1348.742600000000038 1:XK.a/kHz           0.
 DJ    /kHz           5.330000000000000 1:XJbc/kHz           0.
 DJK   /kHz         -24.740000000000002 1:Ma  /MHz           0.
 DK    /kHz           0.                1:Mb-c/MHz           0.
 dJ    /kHz           1.264             1:Tr  /MHz           0.
 dK    /kHz          12.089999999999999 1:Xd  /kHz           0.
```

This output file displays the rotational transitions, standard deviation of the fit, and the fitted dipole moment components (also the rotational constants and distortion constants obtained from the spectrum).

Table 5.4 contains the *ab initio* (for both structures I and II) and experimentally determined dipole moment components which were fit to 7.3 kHz, but the transitions do get messier to measure in the presence of an electric field, so this higher value is acceptable. The μ_c was found to be equal to zero which is consistent with an *ab* plane of symmetry for the system. The dipole moment of the H_3CF monomer is 1.85 D[12] and 0.71521 D[13] for the OCS monomer. Since the monomer dipole moments arrange themselves in an antiparallel fashion to one another, it is apparent that a cancellation

effect must take place between the two individual dipole moment components, and the experimentally determined dipole moment components are consistent with this notion. The total dipole moment is the summation of the individual dipole moment component vectors. The experimental dipole moment components seem to reflect more of an average between Structures I and II in the μ_a component.

Table 5.4: The experimental (determined by QSTARK) and *ab initio* (MP2/6-311++G(2D,2p)) dipole moment components of FM-OCS complex.

	Experimental	Calculated Structures I, II
μ_a / D	1.0910(15)	0.978, 1.147
μ_b / D	0.4425(10)	0.670, 0.507
μ_c / D	0	0, 0
μ_{total} / D	1.1773(18)	1.186, 1.254
N [b]	61	–
Std. dev. / kHz [c]	7.3	–

5.6. Structure

It was explained earlier that the non-physical nature of the planar moments was most likely caused by the internal motion dynamics of the system contaminating the moments of inertia of the system. It is still possible to calculate a structure for this system, however, the internal motions that contaminate the moments of inertia manifest themselves when trying to fit the structure. The fitting process requires that the monomer structures[14] are held at their fixed values, and then structure of the dimer can be characterized by a distance ($R_{C\ldots C}$) and two angles (θ, Φ) which are displayed in Figure 5.1. Structures I and II (Figure 5.1) have the same defined angles (meaning the angle does not change dramatically upon a 60° rotation about the C–F bond between the two structures), so the structural determination was performed for Structure I only. The

program STRFITQ[15] was used to perform several inertial fits. Including all three moments of inertia generated bad fits, so it was necessary to obtain inertial fits for all the possible combinations of the moment of inertia (I_a, I_b, and I_c), (I_a, I_b), (I_a, I_c), and (I_b, I_c) to allow for an optimum structural determination of this complex. This was done in order to determine what effects the different moments of inertia had on the overall structure. When all three moments of inertia are included the structure will not fit very well when there is an inconsistent correlation between them, but when only two moments of inertia are fit the errors in the structural parameters become significantly reduced.

The input file for the STRFITQ program requires quite a complex procedure. First the structure has to be mapped out to tell the program what atoms are connected, the mass of each atom, the bond angle, the bond dihedral, and the distance of separation between the atoms as shown below:

```
FM-OCS
 1   0  0.0        0.0         0.0         0.0
 2   1  1.0        0.0         0.0         1.0
 3   2 12.0       90.0         0.0         1.100
 4   3  1.0      110.6       120.0         1.100
 5   3  1.0      110.6      -120.0         1.100
 6   3 19.0      108.8         0.0         1.383
 7   3 12.0      120.0       180.0         3.602
 8   7 16.0       61.1         0.0         1.1561
 9   8  0.0       90.0       180.0         1.0
10   9  0.0       90.0         0.0         2.7212
11  10 32.0       90.0         0.0         1.0
```

The first row of numbers indicates the atom number in the coordinate system that must be generated by drawing the complex out. The highlighted line will serve as an example for how to read this input file: atom 4 is a hydrogen atom (mass = 1.0) with a 110.6° H–C–H bond angle, a 120° dihedral (out of the plane for this hydrogen atom) and a bond length of 1.100 Å to the carbon. The first column of numbers tells the program the atom number, and the second column tells it what atom it is connected to (e.g. in the highlighted line: atom 4 (hydrogen) is connected to atom 3 (carbon), which is connected

to atom 2 and so on...). The input file for STRFITQ also contains the information about the mass of each substituted atom and the rotational constants of each isotopologue as shown below:

```
 7  13.0
 3  13.0
11  34.0
 2   2.0     4   2.0     5   2.0

7322.575  1655.631  1348.743
7279.464  1651.041  1344.214
7322.169  1614.963  1321.643
7253.531  1618.749  1321.864
7166.756  1513.911  1252.027
```

The first four lines show which atoms are substituted and by the mass which they are substituted (first line: carbon-12 for carbon-13 in atom 7) which is followed by the card containing the rotational constants for the isotopologues in the order that they are described in the previous 4 lines. The first line of rotational constants is for the normal isotopomer. The STRFITQ output file contains the coordinates of each atom in the principle axis system as shown below:

Coordinates in principal axis system of parent species

N	Mass	A	B	C
1	0.000000	3.247935	1.316181	0.000000
2	1.007825	3.725446	0.437555	0.000000
3	12.000000	2.758958	-0.087707	0.000000
4	1.007825	2.664745	-0.724861	0.891716
5	1.007825	2.664745	-0.724861	-0.891716
6	18.998405	1.742195	0.849780	0.000000
7	12.000000	-0.924941	-0.643336	0.000000
8	15.994915	-0.196922	-1.541420	0.000000
9	0.000000	-0.973745	-2.171140	0.000000
10	0.000000	-2.687338	-0.057251	0.000000
11	31.972074	-1.910516	0.572469	0.000000

These are the coordinates of each atom in the principal axis system used by the program and define where the atoms are in this system. The structural parameters obtained from several of these fits are displayed in Table 5.5, with one set of fits excluding the D_3CF isotopologue that caused some variation in the angles and distances. The mass difference

in this isotopologue (as stated in the spectra section) and its different zero point energy vibrational motions are what cause a poorer determination between the deuterated and undeuterated species (note how much the standard deviation in Table 5.5 is reduced when the D_3CF data is excluded). These differences can be accounted for by the increased contamination from the moments of inertia due to a doubling of the mass at the hydrogen coordinates. The "best fit" (last line in Table 5.5) takes into account the variation in the structural parameters from all the obtained fits. The distance between the two carbon atoms is identical to the value obtained from the *ab initio* Structure I.

Table 5.5: Structural parameters obtained from the various inertial fits for the isotopologues of FM-OCS.

	R / Å	θ / degrees	ϕ / degrees	Std. Dev. / u Å^2
All isotopic data				
I_a, I_b, I_c	3.731(74)	50.9(56)	59.7(22)	1.60
I_a, I_b	3.694(31)	51.7(23)	58.37(92)	0.47
I_a, I_c	3.750(30)	49.5(23)	59.19(93)	0.46
I_b, I_c	3.748(10)	51.64(73)	61.55(30)	0.21
All H_3CF data (excludes D_3CF data)				
I_a, I_b, I_c	3.77(24)	48(18)	61.0(75)	1.44
I_a, I_b	3.771(10)	46.19(79)	60.78(32)	0.044
I_a, I_c	3.779(16)	47.3(13)	60.23(50)	0.065
I_b, I_c	3.7703(55)	49.85(41)	62.12(17)	0.033
Best fit	3.75(3)	50(2)	61(2)	–

Comparing the *ab initio* results to the experimental coordinates, it is evident that structure I is slightly preferred over structure II (see Table 5.1).

5.7. Conclusions

The rotational spectra have been measured and assigned for five isotopic species of the methyl fluoride–carbonyl sulfide dimer. The energies of the two lowest theoretical structures were so close that it was determined that there must be a flat potential energy surface (low barrier to rotation) with large amplitude motions allowing the structure to interconvert from structure I to structure II. It was not possible to assign and *E*-type spectrum, because it is thought that the *E*-state transitions would lie far beyond the accessible region of the spectrometer, but may be pursued in future studies. Given all the studies that have been performed on this complex, it is still not possible to express a preference for either structure. Structure I did show slightly better agreement with experimental data, but it is still not possible to rule out structure II as a possible transition state in an internal motion of this dimer system. The dipole moment components were determined with QSTARK in order to determine the two dipole moment components with non-zero values (μ_a and μ_b), and μ_c was found to be zero, which is consistent with the *ab* plane of symmetry for this complex. The experimental data provided in this study provides insight into the need for improvement of *ab initio* models used to provide more accurate theoretical data in the future. Future work will address a search for the *E*-state transitions by utililizing the predicted barrier from *ab initio* calculations in a program such as XIAM to explore the potential *A*-*E* splittings.

References

[1] Serafin, M. M.; Peebles, S. A. *J. Phys. Chem. A.* **2006**, *110(43)*, 11938-11943.

[2] Serafin, M.M.; Peebles, S.A. (in preparation).

[3] Serafin, M.M.; Peebles, S.A. *J. Phys. Chem. A.* **2008**, *112*, 1473.

[4] Serafin, M.M.; Peebles, R.A.; Peebles, S.A. **2008**, manuscript in preparation.

[5] Serafin, M.M.; Peebles, R.A., Peebles, S.A. (submitted for publication).

[6] Caminati, W.; López, W.C.; Alonso, J.L.; Grabow, J.-U. *Angew. Chem. Intl. Ed.* **2005**, *44*, 3840.

[7] Frisch, M. J.; Trucks, G. W.; Schlegel, H. B.; Scuseria, G. E.; Robb, M. A.; Cheeseman, J. R.; Montgomery, J. A., Jr.; Vreven, T.; Kudin, K. N.; Burant, J. C.; Millam, J. M.; Iyengar, S. S.; Tomasi, J.; Barone, V.; Mennucci, B.; Cossi, M.; Scalmani, G.; Rega, N.; Petersson, G. A.; Nakatsuji, H.; Hada, M.; Ehara, M.; Toyota, K.; Fukuda, R.; Hasegawa, J.; Ishida, M.; Nakajima, T.; Honda, Y.; Kitao, O.; Nakai, H.; Klene, M.; Li, X.; Knox, J. E.; Hratchian, H. P.; Cross, J. B.; Bakken, V.; Adamo, C.; Jaramillo, J.; Gomperts, R.; Stratmann, R. E.; Yazyev, O.; Austin, A. J.; Cammi, R.; Pomelli, C.; Ochterski, J. W.; Ayala, P. Y.; Morokuma, K.; Voth, G. A.; Salvador, P.; Dannenberg, J. J.; Zakrzewski, V. G.; Dapprich, S.; Daniels, A. D.; Strain, M. C.; Farkas, O.; Malick, D. K.; Rabuck, A. D.; Raghavachari, K.; Foresman, J. B.; Ortiz, J. V.; Cui, Q.; Baboul, A. G.; Clifford, S.; Cioslowski, J.; Stefanov, B. B.; Liu, G.; Liashenko, A.; Piskorz, P.; Komaromi, I.; Martin, R. L.; Fox, D. J.; Keith, T.; Al-Laham, M. A.; Peng, C. Y.; Nanayakkara, A.; Challacombe, M.; Gill, P. M. W.; Johnson, B.; Chen, W.; Wong, M. W.; Gonzalez, C.; Pople, J. A.; Gaussian 03W, revision D.01; Gaussian, Inc.: Pittsburgh, PA, **2004**.

[8] Rigid Rotor Spectrum Fitting Program. Version 3.1

[9] Pickett, H.M. *J. Mol. Spec.* **1991**, *148*, 371.

[10] Demaison, J.; Breidung, J.; Thiel, W.; Papousek, D. *Struct. Chem.* **1999**, *10*, 129.

[11] Kisiel, Z.; Kosarzewski, J.; Pietrewicz, B.A.; Pszczółkowski, L. *Chem. Phys. Lett.* **2000**, *325*, 523.

[12] Nelson, R.D.; Lide, D.R.; Maryott, A.A. In *Selected Values of Electric Dipole Moments for Molecules in the Gas Phase*; NIST Standard Reference Database, NBS10: Washington, DC, 1967.

[13] Muenter, J.S. *J. Chem. Phys.* **1968**, *48*, 4544.

[14] **Monomer Structures** Harmony, M.D.; Laurie, V.W.; Kuczkowski, R.L.; Schwendeman, R.H.; Ramsay, D.A.; Lovas, F.J.; Lafferty, W.J. Maki, A.J. *J. Phys. Chem. Ref. Data.* **1979**, *8*, 619.

[15] Schwendeman, R.H. In *Critical Evaluation of Chemical and Physical Structural Information*; Lide, D.R., Paul, M.A., Eds.;National Academy of Sciences: Washington, DC, 1974. The STRFITQ program used in this work is the University of Michigan modified version of Schwendeman's original code.

Chapter 6

Comparison of TFM–OCS, DFM–OCS, FM–OCS, and TFM–CO_2 Experimental Trends with Parameters Obtained from New and Existing Computational Models

6.1. Introduction

So far, two weakly bound dimer systems have been discussed in detail in previous chapters of this thesis (namely DFM–OCS discussed in Chapter 4 and FM–OCS in discussed Chapter 5)[1, 2]. Both of these systems are members of a series of complexes that have been studied with FTMW spectroscopy in order to obtain information about the structures and dynamics of these systems in the ground vibrational state (and perhaps torsionally excited states if internal rotation is observed). The series can be extended with previous published data from trifluoromethane–carbonyl sulfide and trifluoromethane–carbon dioxide dimers (TFM–OCS and TFM–CO_2 respectively)[3, 4] to examine trends in how hydrogen bonds are affected by the environment near a C–H···O interaction with respect to changes as a function of the number of fluorine atoms on the fluorinated methane subunit (or in the case of TFM–CO_2 when the sulfur atom of OCS is exchanged for an oxygen atom). Generally, it is assumed that the number of fluorine atoms on the methyl subunit will greatly affect the acidity of the hydrogen atoms on that subunit. Since fluorine is the most electronegative atom on the periodic table, it is reasonable to imagine that the electron density around a hydrogen atom will be reduced as more fluorine atoms are added to the subunit, and thus the hydrogen will have a higher affinity for interaction with an oxygen atom belonging to either OCS or CO_2. CO_2 has no net dipole moment (unlike OCS, where $\mu = 0.7152\ (2)$ D), and an induced dipole moment on the CO_2 molecule should be considered for interactions between the TFM and CO_2 molecules. The interaction between the two monomer subunits can also occur via a dipole–quadrupole interaction (which is likely to predominate), due to the quadrupolar nature of CO_2.

This chapter concerns the determination of structural parameters obtained from *ab initio* calculations for the four weakly bound complexes in the series, which are then compared to the experimental structures. Higher levels of theory (than the previously employed MP2 and DFT methods) and new basis sets will be explored in this study. Previously only the 6-311++G(2d,2p) basis set was employed in theoretical calculations. Two minimum energy structures have been calculated for each dimer system and the relationships between these two minimum energy configurations will be investigated, with a focus on structural parameters and energy differences of a variety of levels. For each of the calculated structures, the minimum energy structures are referred to as Structure I, while the higher energy structures are referred to as Structure II. Important parameters that relate the chemical interaction of the two monomers are the C–H···O bond distance (r_{OH}), the C···C bond distance (r_{CC}: distance between two carbon atoms which can also be related to the center of mass separation (r_{CM}) of the two monomer subunits), and the two bond angles (θ and ϕ) which align the monomers relative to the line joining the two carbon atoms (see figures 6.1-6.8). All the complexes in this series have a plane of symmetry and belong to the C_s point group. Since the monomer structures are held constant at their literature values, these two bond angles are the only two angles that need to be defined in any structure, and are the only two angles that can affect the rotational constants. Bond distances are a good indicator of the bond strength between two atoms, and the bond angles describe how the monomer subunits arrange themselves in the plane of symmetry. All four of the dimer systems exhibit some structural similarities that can be immediately gathered by examining Figures 6.1-6.8. To a first approximation, the two calculated minimum energy structures for each complex

are related to one another by some rotation of the fluorinated methane subunit, specifically: TFM–OCS, 60° rotation about the C_3 axis of TFM; DFM–OCS, 180° rotation about the C_2 axis of DFM; FM-OCS, 60° rotation about the C_3 axis of FM; and TFM–CO_2, 60° rotation about the C_3 axis of TFM. The relative energies for the configurations displayed in Figures 6.1-6.8 were calculated with the MP2 / 6-311++G(2d,2p) level and basis set.

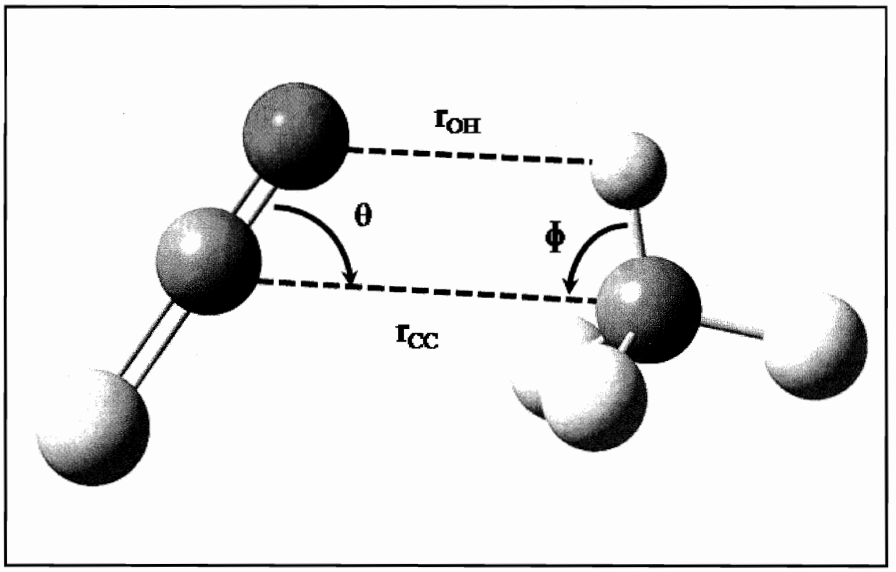

Figure 6.1: Structure I of TFM–OCS dimer. This is the minimum energy configuration of this complex. Structural parameters defined for the bond angle and distances.

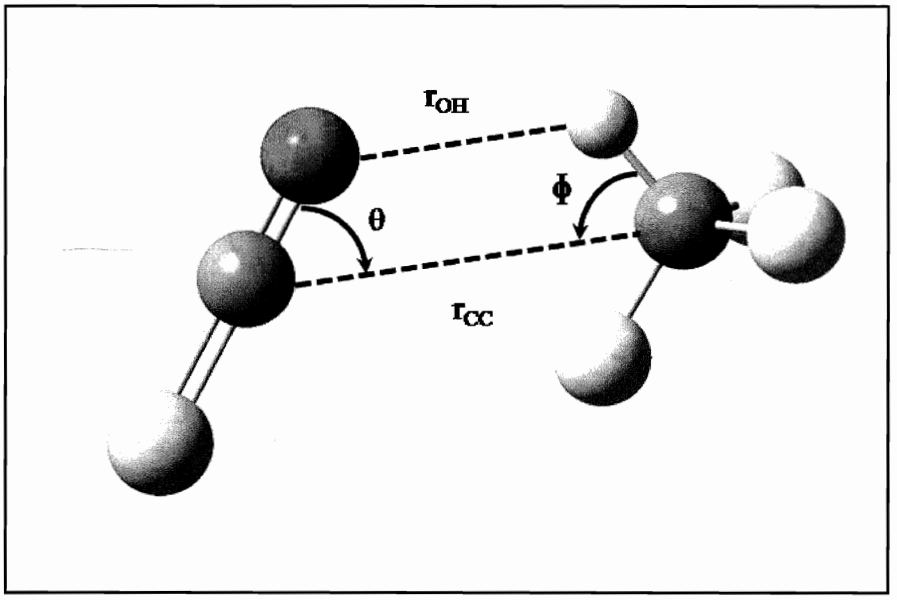

Figure 6.2: Structure II of TFM–OCS dimer. This is the next higher energy configuration +90 cm^{-1} relative to Structure I. Structural parameters defined for the bond angle and distances.

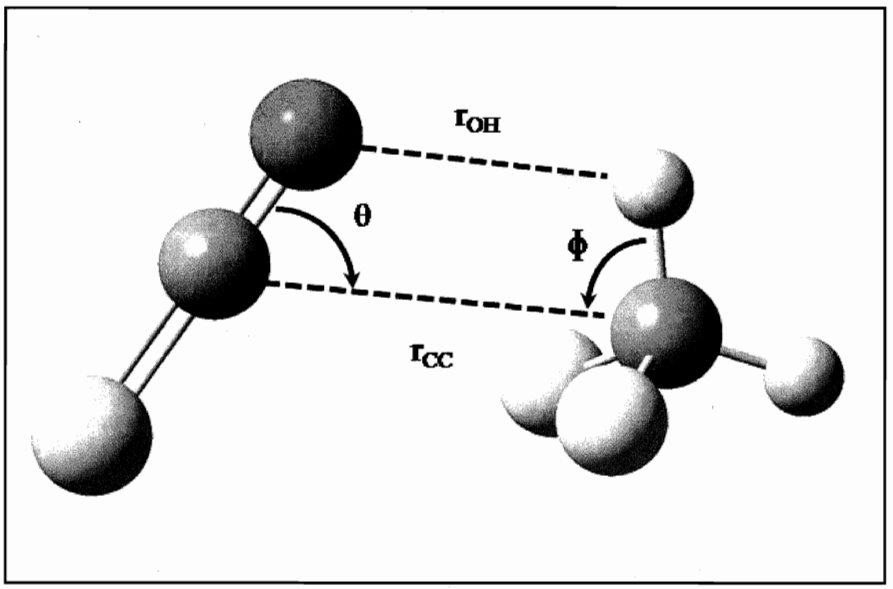

Figure 6.3: Structure I of DFM–OCS dimer. This is the minimum energy configuration of this complex. Structural parameters defined for the bond angle and distances.

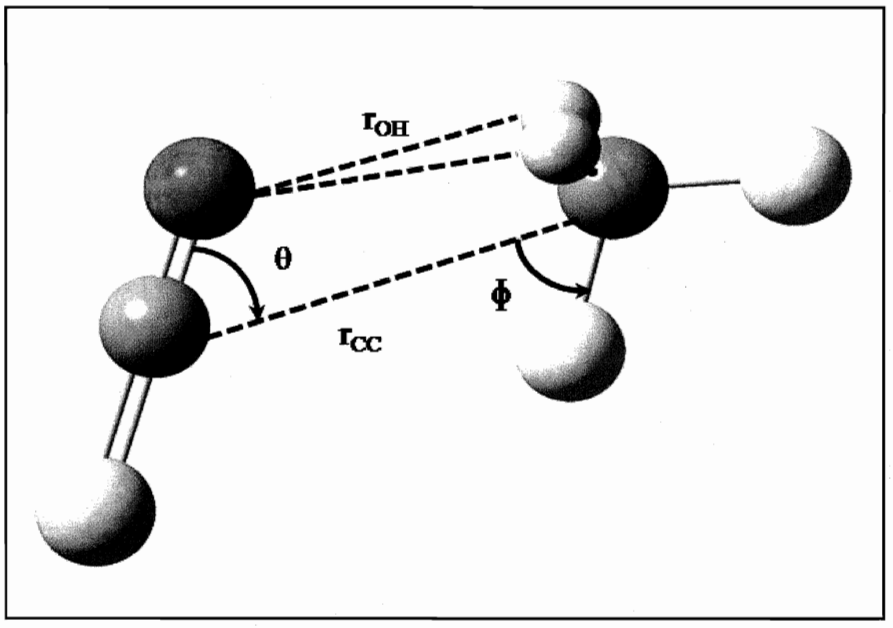

Figure 6.4: Structure II of DFM–OCS dimer. This is the next higher energy configuration +76 cm^{-1} relative to Structure I. Structural parameters defined for the bond angle and distances.

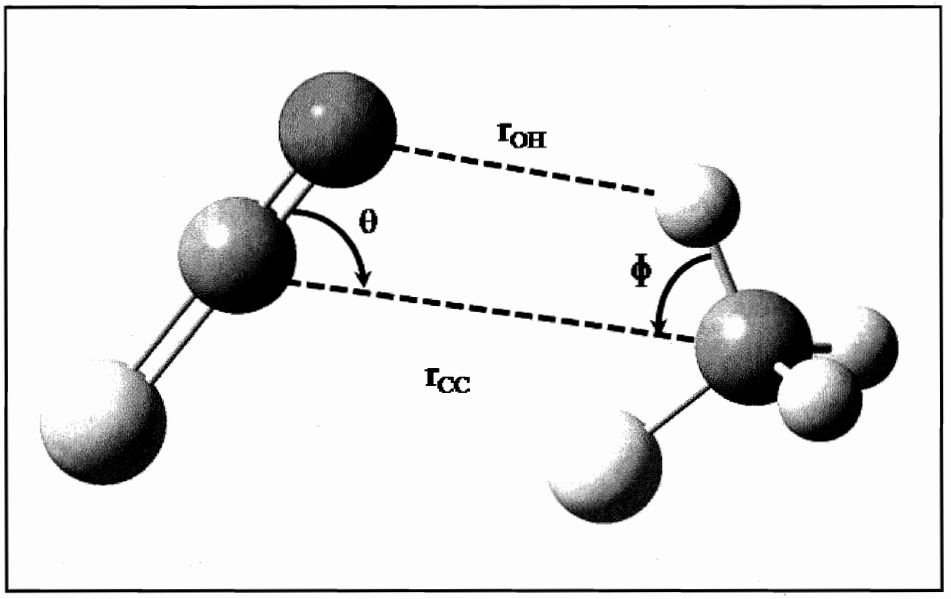

Figure 6.5: Structure I of FM–OCS dimer. This is the minimum energy configuration of this complex. Structural parameters defined for the bond angle and distances.

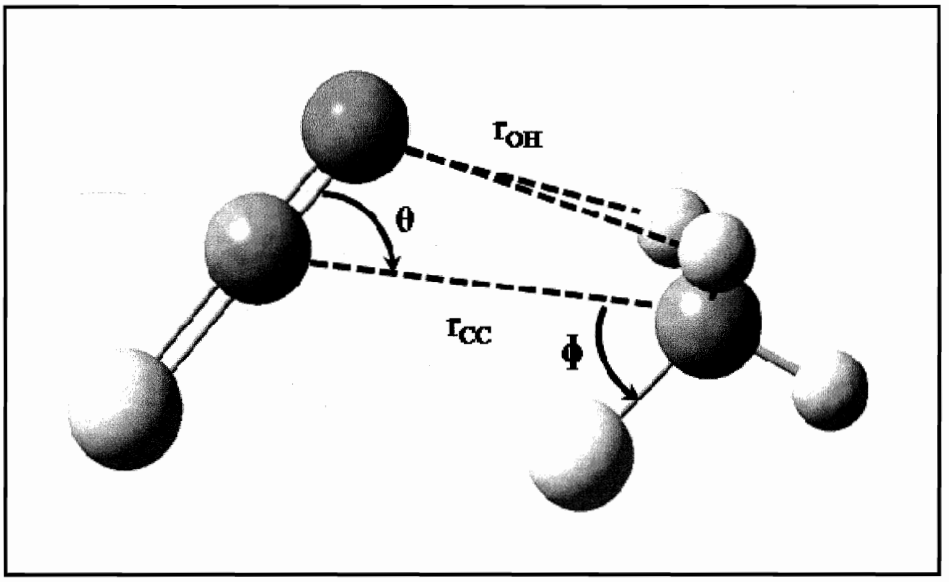

Figure 6.6: Structure II of FM–OCS dimer. This is the next higher energy configuration +0.5 cm^{-1} relative to Structure I. Structural parameters defined for the bond angle and distances.

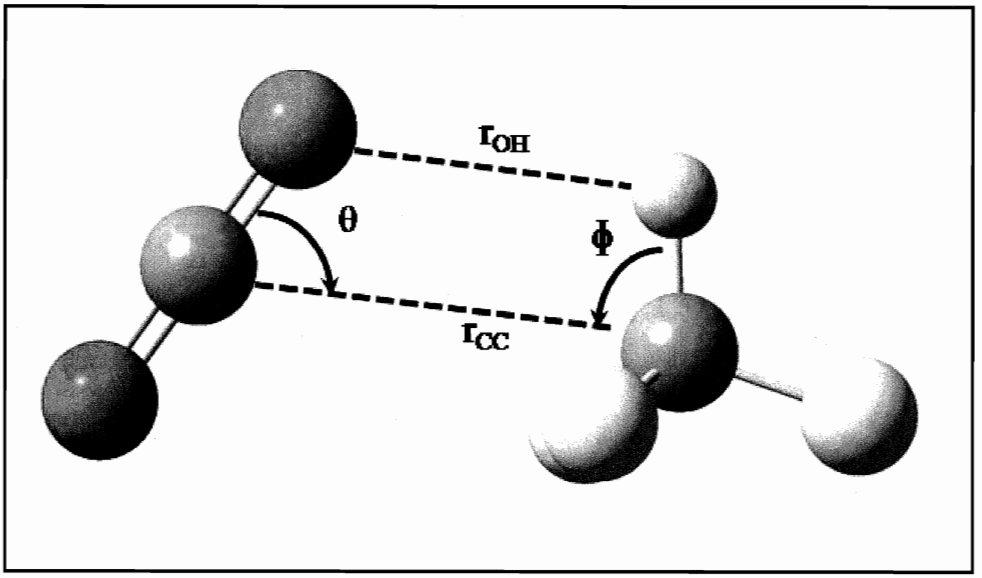

Figure 6.6: Structure I of TFM–CO_2 dimer. This is the minimum energy configuration of this complex. Structural parameters defined for the bond angle and distances.

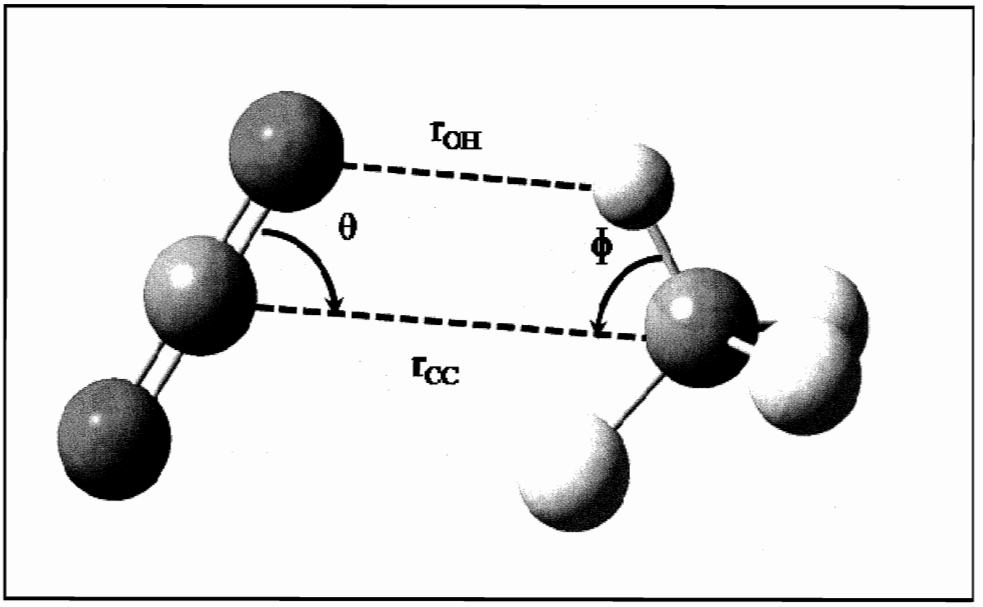

Figure 6.7: Structure II of TFM–CO_2 dimer. This is the next higher energy configuration +75 cm^{-1} relative to Structure I. Structural parameters defined for the bond angle and distances.

6.2. Investigation of levels of theory

One purpose of this chapter is to examine what effect the level of theory has on the electronic and structural parameters of interest (dipole moment data, rotational constants, structures). For high resolution microwave spectroscopy, *ab initio* calculations provide theoretical rotational constants and dipole moment information which are then used as a guide in locating and assigning rotational spectra. *Ab initio* calculations are based on "first principles," meaning no experimental data is included in the calculations (as would be the case in semi-empirical calculations), and they rely solely on quantum mechanics and physical constants to approximate the Schrödinger equation. These calculations can provide high quality quantitative predictions that are not limited to any particular type of chemical system, making them ideal to compute theoretical data for weakly bound complexes. Most of the calculations were performed at the MP2 level (Møller–Plesset second order perturbation theory[6]), which is one of the simplest models that includes electron correlation effects. The addition of electron correlation to the calculation improves the description of the repulsions between electrons relative to methods such as Hartree-Fock (HF) calculations, and includes the important dispersion interactions that govern the structures of weakly bound complexes. MP2 calculations are more computationally intensive and require more computational resources than HF theory, but the trade-off is that theoretical results provided by electron correlation models are more precise, resulting in more accurate determination of theoretical structural parameters relative to HF theory. Electron correlation improves the intermolecular interaction description because it includes a better approximation of how electrons interact with one another (electron-electron repulsion terms). The electrons are given

more freedom in these models and induced dipole moments can be more accurately modeled with this level of theory.

To investigate levels of theory beyond MP2, coupled cluster (CCD) electron correlation methods were utilized for the four lowest energy structures (i.e. structures in Figures 6.1, 6.3, 6.5, 6.7) that were initially optimized by MP2, however, there was concern for the amount of computational resources utilized by this model. Coupled cluster calculations have a wavefunction that is a linear combination of many determinants and allow the incorporation of additional excited electronic states, therefore allowing for an improvement in the description of the electron distribution. The description of electron correlation is approximated to a higher level than in MP2, so it would be hoped that the minimum energy configurations of these structures should more closely resemble those obtained by experiment due to the increased complexity of this quantum mechanical model. To give an idea of the computational resources required to operate a CCD calculation vs. an MP2 calculation; the MP2 calculations take between 10-15 hrs to complete for any given complex, while the CCD calculations take between 40-50 hrs to complete. These times can be optimized by changing the number of processors and gigabytes of RAM that are utilized per calculation, but the CCD calculations take at least 24 hrs longer to complete than an MP2 calculation.

It should be mentioned that density functional theory (DFT) was also investigated for this study; however, this technique is unpredictable for weakly bound complexes and can sometimes provide unreliable results. In our case, we ran some preliminary DFT calculations with the same basis sets described later, but the results were poorer than those obtained by MP2, so this level of theory was abandoned for the present studies.

6.3. Investigation of basis sets

A basis set is a mathematical representation[5] of the atomic orbitals in the system (usually utilizing Gaussian type functions, to describe electron density distribution), and by combining the orbital descriptions, a mathematical approximation for the total electronic wavefunction of the system is obtained. The Gaussian functions provide a constraint for the region of space occupied by the electron in each orbital, and larger basis sets provide more freedom of movement to the electron, but a larger basis set also corresponds to an increase in computational resources. Previously it was shown[1, 2, 3, 4] that *ab initio* calculations at the MP2 level of calculation, with 6-311++G(2d,2p) basis sets, have performed very well to provide theoretical predictions of rotational constants to within 5% of experimental values. The 6-311++G(2d,2p) basis set will now be referred to as the Standard Basis Set (SBS). The 6-311G basis set belongs to a family of polarized Pople[5] basis sets that allow atomic orbitals to change in shape beyond the ground state (lowest energy configuration) description of each atomic orbital[5]. These basis sets also enable diffuse functions on hydrogen atoms and heavy atoms. Diffuse functions are slightly larger versions of regular orbitals (which allow orbitals to take up a larger region of space) and are denoted for heavy atoms and hydrogen atoms respectively by the first and second (++) signs in the Pople notation of the SBS shown above. Multiple polarization functions are also included in this basis set to increase the number of functions utilized per orbital, where the polarization functions have been employed to include the two d type functions on heavy atoms and two p type functions for hydrogen atoms (shown as 2d and 2p respectively in the notation). Polarization functions allow

some distortion of the electron density around the atoms allowing for a more accurate theoretical determination of weak interactions such as hydrogen bonds.

6.4. Comparison of Minimum Energy Configurations (Structure I) for Each Complex

Structure I (Fig. 6.1, 6.3, 6.5, 6.7) had provided the most reliable theoretical structural parameters compared to experimentally determined structures for each respective complex. By comparing these predicted structures (calculated with MP2 theory employing the SBS) to one another, a structural trend in the manner of complexation is observed for the four complexes. In each complex, the monomers interact with one another via a dipole–dipole interaction resulting in an approximate antiparallel arrangement of the monomer dipoles. The theoretical predictions of intermolecular distances between atoms, namely the C···C and O···H distances, have been shown to display similarities among the four structures as well. Table 6.1 shows predicted r_{CC} and r_{OH} values (obtained from the MP2 level of theory employing the SBS, and also from CCD / *cc- pVTZ* level and basis set - specifics of which are described in the next section), alongside the experimentally measured values for each complex. Note that the predicted values compared in Table 6.1 are for predicted structures of Structure I for each respective complex.

Table 6.1: Comparison of r_{CC} and r_{OH} values predicted by MP2 theory with the SBS, CCD theory with the *cc- pVTZ* basis set, and experimental values.

Structure [ref.]	r_{OH} / Å (expt.)	r_{OH} / Å (MP2)	r_{OH} / Å (CCD)	r_{CC} / Å (expt.)	r_{CC} / Å (MP2)	r_{CC} / Å (CCD)
TFM-OCS [3]	2.90 (5)	2.63	2.74	3.642 (17)	3.48	3.63
DFM-OCS [1]	2.88 (3)	2.65	2.80	3.58 (4)	3.45	3.56
FM-OCS [2]	2.65 (6)	2.65	2.75	3.75 (3)	3.75	3.83
TFM-CO_2 [4]	2.83 (2)	2.70	2.78	3.57 (5)	3.45	3.53

The data displayed in Table 6.1 was then used to generate two column plots comparing the theoretical distances to the experimentally determined values of r_{OH} (Fig. 6.9)and r_{CC} (Fig. 6.10) for an easier visualization of these methods.

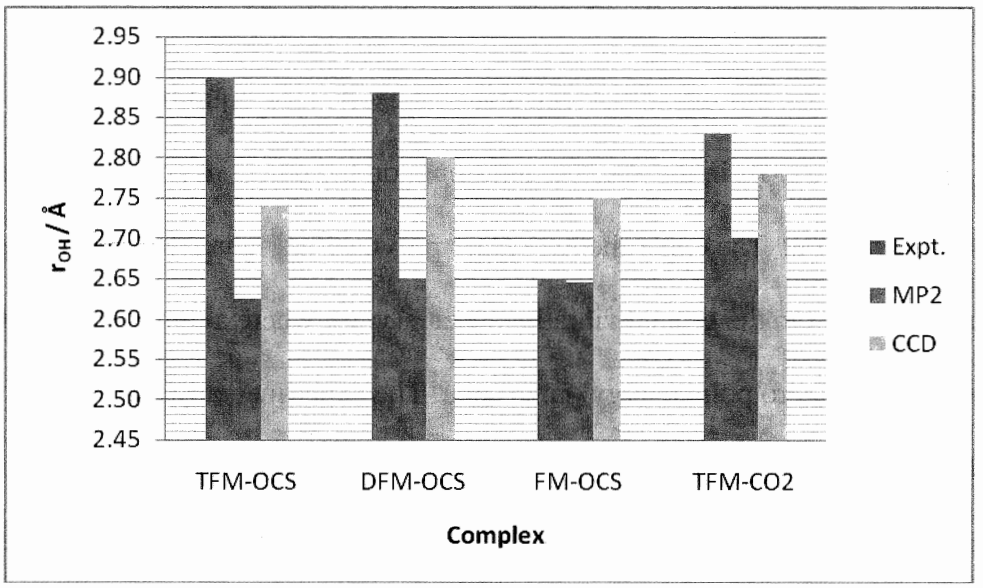

Figure 6.8: The intermolecular distances between the O and H atoms predicted by two levels of theory compared with experimentally determined distances.

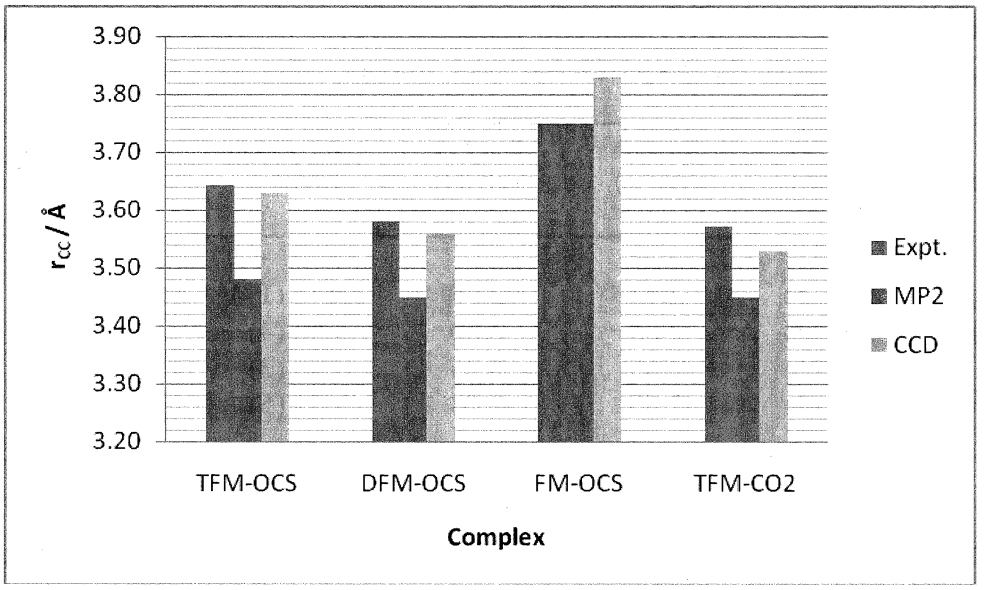

Figure 6.9: The intermolecular distances between the two carbon atoms predicted by two levels of theory compared with experimentally determined distances.

Before continuing, it should be noted that these calculations provide equilibrium structures. That is, the complexes are calculated to exist in the equilibrium state, meaning they would exist in the absolute minimum on the potential energy surface with no vibrational motion. The experimental values provided in Figures 6.9 and 6.10 refer to complexes that exist in the ground vibrational state (v=0), where a minimum amount of vibrational energy (zero point energy) is present. The experimentally obtained parameters are therefore, by definition, referring to a slightly different structure than the *ab initio* equilibrium values. However, given the quality of agreement at present, the difference between bond distances of the equilibrium and ground state structures (due to the difference in states) is so minimal that it can be overlooked for the present study. However, as the predictions get better at approximating experimental values it will be necessary to take the structural differences between the ground vibrational state and equilibrium state into account (see Conclusions section for more details).

For three out of the four complexes (specifically TFM–OCS, DFM–OCS, and TFM–CO_2), the intermolecular O···H distances and C···C distances are very similar (Tables A2-A5 in Appendix I). The experimental r_{OH} distances fall between 2.82 Å and 2.90 Å, are predicted between 2.63 Å and 2.70 Å with MP2 theory, and are predicted between 2.74 Å and 2.80 Å with CCD theory. Also, the experimental r_{CC} distances are between 3.57 Å and 3.64 Å, are predicted between 3.45 Å and 3.48 Å with MP2 theory, and are predicted between 3.53 Å and 3.63 Å with CCD theory. For these three complexes, there is a general improvement of structural parameters in going from MP2 to CCD methods. MP2 theory seems to do better than CCD in predicting the bond distances for FM–OCS, while CCD theory overestimates both distances. In every other complex, the distances are underestimated by both theoretical models, but MP2 was in almost perfect agreement with the distances of FM–OCS (by slightly underestimating and slightly overestimating the true values of r_{OH} and r_{CC} respectively). Overall, CCD / *cc-pVTZ* is better than MP2 / 6-311G++(2d,2p) at estimating the intermolecular bond distances for three out of the four cases studied.

During analysis of experimental data, an interesting linear correlation was also observed when relating the center of mass separation to the monomer dipole moments of each monomer subunit for the OCS series of complexes (TFM–OCS, DFM–OCS, and FM–OCS). Table 6.2 displays the monomer dipole moments, the experimentally determined r_{CM} (distance between the monomer centers of mass), and the predicted r_{CM} values obtained from the MP2 and CCD calculations. It is not trivial to obtain a theoretical value of r_{CM} from an *ab initio* structure since the center of mass needs to be calculated separately for each *ab initio* optimized structure, and the theoretical r_{CM} values

are tabulated in Table 6.2. A simple approximation was used to obtain these crude r_{CM} values by obtaining a ratio of the experimentally determined r_{CM} and r_{CC} values and another ratio of the experimentally determined r_{CM} and r_{OH} values. These ratios were then applied to either the predicted r_{OH} or r_{CC}, resulting in two r_{CM} values which were similar in magnitude. Averaging these two calculated values provides a crude prediction of r_{CM} from the *ab initio* calculations to allow quick determination if a correlation was apparent.

Table 6.2: Crude theoretical and experimental r_{CM} values for TFM–OCS, DFM–OCS, and FM–OCS dimers, with their monomer dipole moments.

Monomer	Dipole Moment[6]	r_{CM} (expt.) / Å [ref.]	r_{CM} (MP2) / Å	r_{CM} (CCD) / Å
TFM	1.65	3.965 (26) [3]	3.70	3.85
DFM	1.96	3.41 (2) [1]	3.21	3.35
FM	1.85	3.60 (3) [2]	3.60	3.70

A separate plot has been made to show the linear correlation of the monomer dipole moment with respect to the center of mass separation for each complex, which are displayed in Figures 6.11-6.13 for the experimental, CCD predicted, and MP2 predicted center of mass separations. The experimental correlation of these parameters is exceptional, with a first order trendline fitting to $R^2 = 0.9998$ as shown in Figure 6.11. The correlation of these parameters was reduced by about 15% for predictions made by the CCD calculation, rendering a first order trendline fitting to $R^2 = 0.8514$ (Figure 6.12). A further reduction of about 8% was observed in the correlation of these parameters for the first order trendline obtained from MP2 predictions, fitting to $R^2 = 0.7715$. The error bars in Fig. 6.11 display the experimental error in the r_{CM}, and the theoretical errors were within 3% for the CCD calculated values, and within 4% for the MP2 calculations.

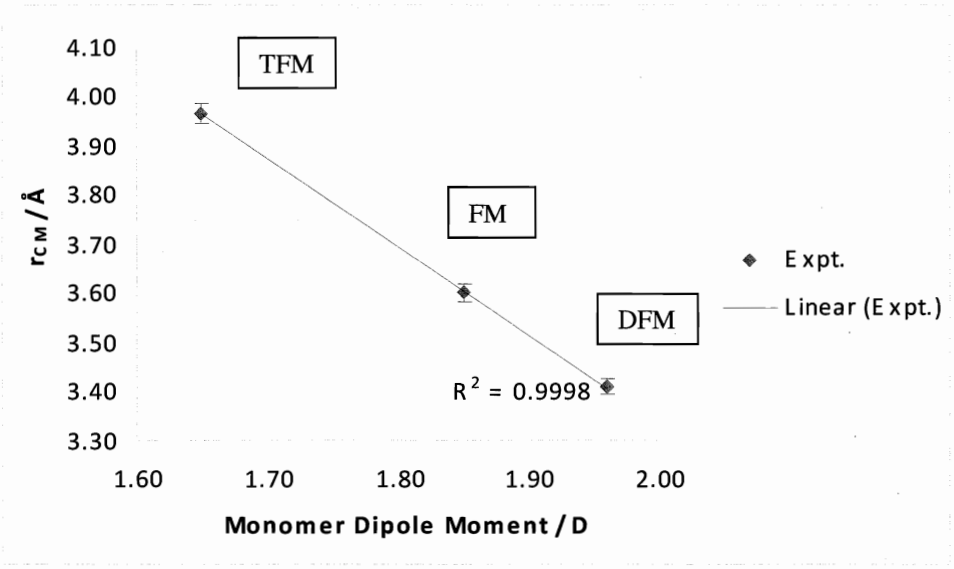

Figure 6.10: Linear correlation observed of monomer dipole moments with respect to experimentally determined center of mass separations for TFM-OCS, DFM–OCS, and FM–OCS.

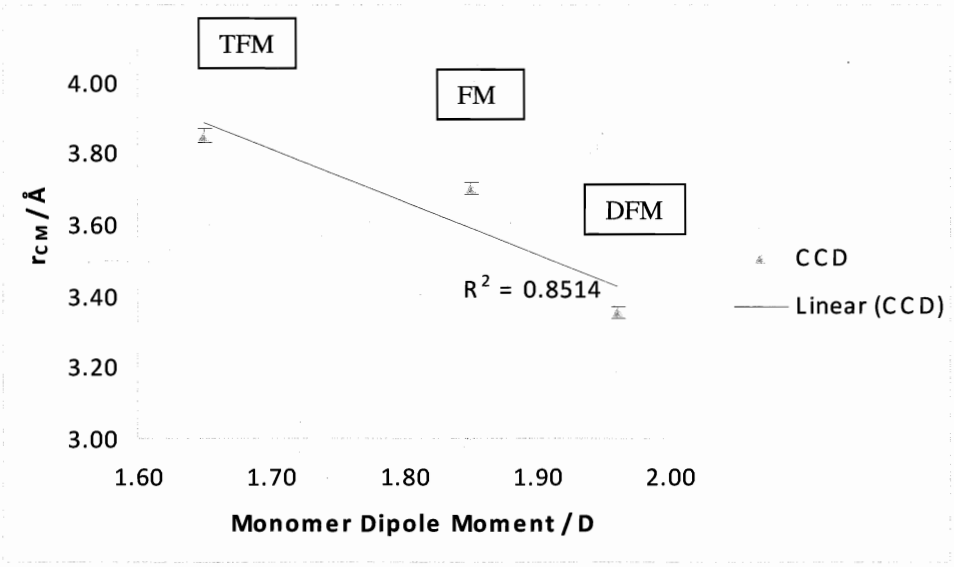

Figure 6.11: Linear correlation observed of monomer dipole moments with respect to crude theoretically determined (CCD) center of mass separations for TFM-OCS, DFM–OCS, and FM–OCS.

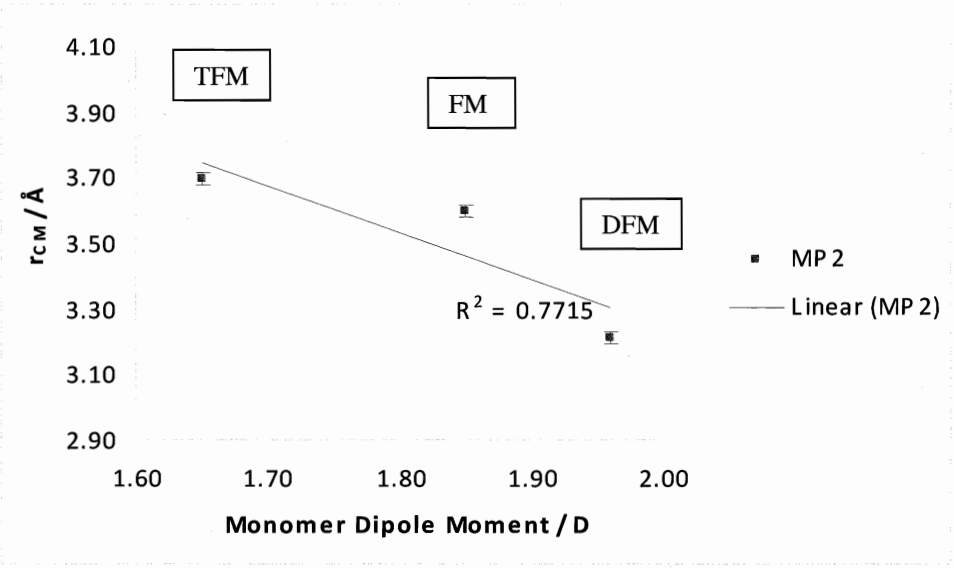

Figure 6.12: Linear correlation observed of monomer dipole moments with respect to crude theoretically determined (MP2) center of mass separations for TFM-OCS, DFM–OCS, and FM–OCS.

The linear relationship between the experimental centers of mass and the monomer dipole moments deteriorates when comparing the true values with crude predicted r_{CM} parameters obtained with CCD theory, with a further deterioration in predictions when going from CCD theory to MP2 theory. [Note that the r_{CM} bond distance for TFM–CO_2 is 3.65 (5) Å, (MP2 / SBS and CCD / *cc-pVTZ* r_{CM} values were 3.538 and 3.617 Å respectively) and a similar plot can be performed once calculations of DFM–CO_2 and FM–CO_2 are obtained].

After the linear correlation was observed in Figures 6.11-6.13, the exact center of mass separations were calculated for each complex in order to improve on the crude approximations performed above. The centers of mass were then calculated separately for each monomer subunit obtained from their respective CCD and MP2 calculations. Table 6.3 contains the r_{CM} values obtained for the MP2 and CCD calculations of the three minimum energy conformations for TFM–OCS, DFM–OCS, and FM–OCS. Figure 6.14

shows the linear trend of the monomer dipole moment as a function of the center of mass separations obtained from CCD calculations, and Figure 6.15 reproduces that trend from the values obtained in the MP2 calculations. It can be seen that a considerable improvement is obtained relative to the crude values (Figures 6.12 and 6.13).

Table 6.3: The center of mass separations after the centers of mass were individually calculated for MP2 and CCD levels of theory with their respective relative errors, and the experimental center of mass separations.

Species	r_{CM} expt.	r_{CM} MP2	% Rel. Error	r_{CM} CCD	% Rel. Error
TFM–OCS	3.97 (3)	3.83	3.4	4.01	1.1
DFM–OCS	3.41 (2)	3.31	3.0	3.42	0.1
FM–OCS	3.60 (3)	3.51	0.4	3.58	2.6

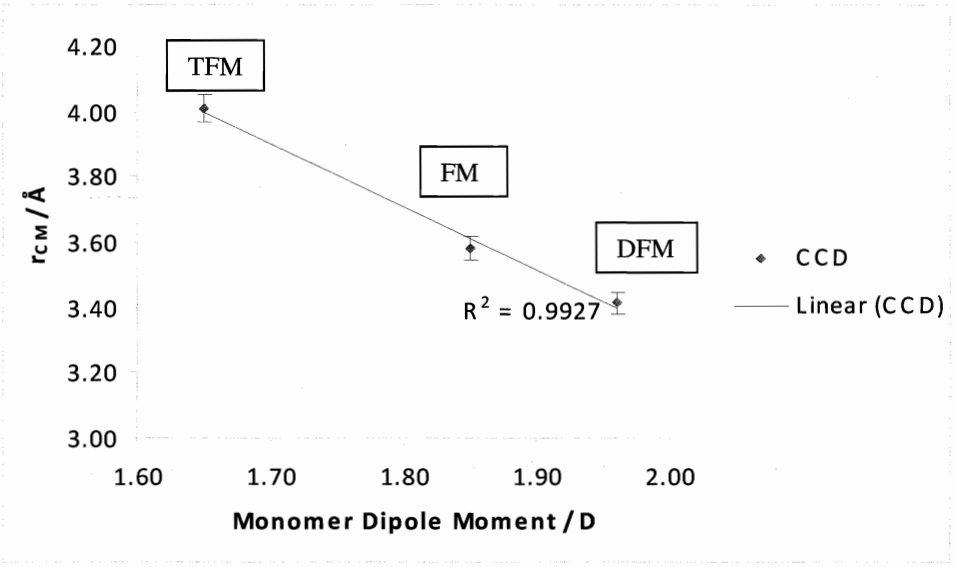

Figure 6.13: Linear correlation observed of monomer dipole moments with respect to exact theoretically determined (CCD) center of mass separations for TFM-OCS, DFM–OCS, and FM–OCS.

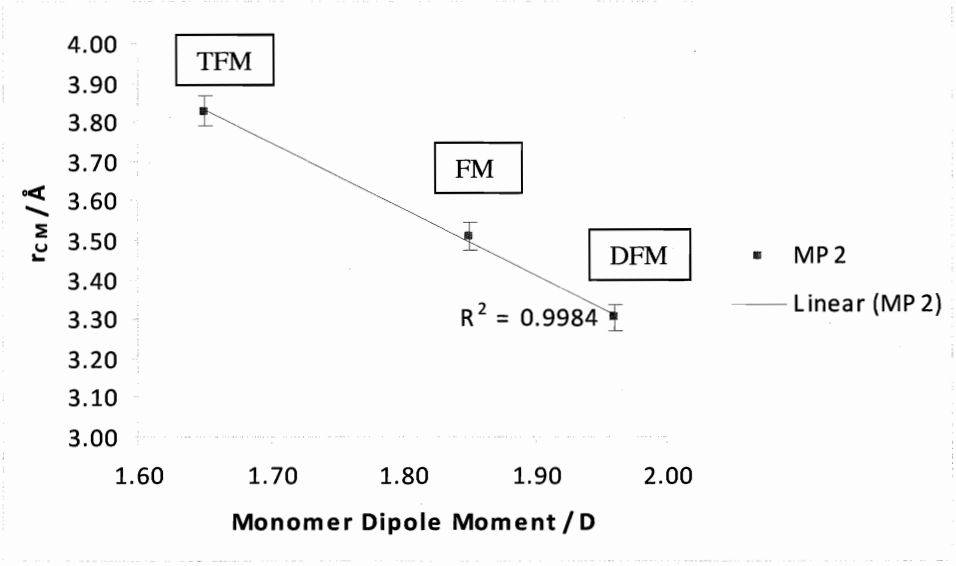

Figure 6.14: Linear correlation observed of monomer dipole moments with respect to exact theoretically determined (MP2) center of mass separations for TFM-OCS, DFM–OCS, and FM–OCS.

These plots show that both the CCD and MP2 calculations reproduce the linear correlation to within 1.0% error bars for the worst point. Both MP2 and CCD levels of theory performed exceptionally well in predicting the center of mass separations for these three complexes. The MP2 calculations provide a slightly better correlation than the CCD calculations in this case, but the difference in correlation (R^2) is minor, as shown in Figures 6.14 and 6.15. Bond distances are indicative of the strength of binding, so as the monomer dipole of the fluorinated methane subunit is increased, the binding energy should increase pulling the monomers closer together (decreasing r_{CM}).

6.5. Basis set Dependence of *Ab Initio* Calculations

Up to this point, the effects of the level of theory on theoretical values have been explored, but the level of theory is not the sole factor influencing the performance of *ab initio* calculations. The basis set is the second factor that influences how well theoretical calculations perform. The number of basis functions included in any basis set directly affects the complexity and the computational resources required to run a calculation.

Structural and electronic parameters are compared to existing experimental values for the four systems thus described for two levels of theory (namely MP2 and CCD) with a variety of basis sets to determine how basis sets may be systematically improved to obtain better theoretically determined values. For most of the calculations, the level of theory was maintained at MP2; four CCD calculations were also performed. By addition of the "Restricted" model, the electrons can also be forced to be spin paired in an orbital, which reduces the computational intensity of the calculation because paired electrons can be approximated in the Hamiltonian. A restricted model can only be used for species that are in the singlet state, while species that exist in the triplet state have to be treated with an "Unrestricted" model because there is an electron that cannot be spin paired in an orbital. It should be noted that a "Restricted" or "closed-shell" MP2 (RMP2) method was used for the calculations (except for those which used CCD).

Systematic variation in basis sets might lead to the refinement of theoretical techniques and may be employed in future use for better structural predictions. Basis sets, consisting of Dunning's correlation consistent basis functions[7] that are specifically used for high quality calculations using electron correlation methods, have been selected because the number of excitations per function can be systematically increased from double to triple excitations, and they can also be augmented. This design of the *cc-pVXZ* basis sets should enable them to perform more efficiently than the SBS. To allow for flexibility of molecular orbitals, the basis sets are expanded by inclusion of multiple polarization functions (p) for the valence orbitals (V). The polarization functions can have double, triple, quadruple, etc. functions in each basis set, which allows for systematic variability in the basis sets ($D < T < Q$ etc. respectively). The multiple

polarization functions are zeta (ζ) functions (denoted with a *Z*) and are utilized to scale core and valence orbitals to size. An example of the notation for a typical basis set used for the calculations employing a *cc-* basis is: *cc-pVTZ*, or correlation consistent, polarizable valence orbitals with tripled ζ-functions (three functions per orbital). These basis sets can also be augmented (*aug-*) to include diffuse functions for each type of orbital thereby enlarging the region accessible by the electrons. Table 6.4 displays all the computational methods and basis sets employed including the orbitals that are described with polarization functions for the various atoms. The *cc-* methods are particularity useful for making predictions in circumstances where electron clouds may be distorted, such as the induced dipole for CO_2 when it interacts with TFM. It should be noted that an *aug-* basis sets includes diffuse functions for the same orbitals that are classified as polarizable orbitals. Table 6.4 also includes the number of basis functions for each calculation performed for TFM–OCS with the SBS for comparison. Of course, we need to exercise some care when increasing basis set size because time scaling is an issue. MP2 calculations scale with a N^5 factor (where N is the number of basis functions), so if the number of basis functions is doubled, the calculation could take up to 32 times longer ($2^5 = 32$).

Table 6.4: Polarization and diffuse functions[8] that are added to the corresponding basis sets for each atom, number of primitive Gaussian functions, and the number of basis functions per basis set for TFM–OCS.

Basis Set	H atom	C, O atoms	S atom	Primitive Gausians[a)]	Total No. of Basis Functions[b)]
MP2/*cc-pVDZ*	2s, 1p	3s, 2p, 1d	4s, 3p, 1d	278	107
MP2/*aug-cc-pVDZ*	2s, 1p	3s, 2p, 1d	4s, 3p, 1d	352	174
Diffuse Functions[d)]	1s, 1p	1s, 1p, 1d	1s, 1p, 1d		
MP2/6-311++G(2d,2p)[c)]	2s, 2p	2p, 2d	2p, 2d	320	207
MP2 or CCD / *cc-pVTZ*	3s, 2p, 1d	4s, 3p, 2d, 1f	5s, 4p, 2d, 1f	434	228
MP2/*aug-cc-pVTZ*	3s, 2p, 1d	4s, 3p, 2d, 1f	5s, 4p, 2d, 1f	584	349
Diffuse Functions[d)]	1s, 1p, 1d	1s, 1p, 1d, 1f	1s, 1p, 1d, 1f		

[a)] Total number of primitive Gaussian functions in each basis set calculated for TFM–OCS. [b)] Number of basis functions in each basis set for TFM–OCS. This number of functions governs the computational resources required to run the calculation. [c)] SBS, showing orbitals described by polarization functions. [d)] Diffuse functions are included in augmented basis sets (*aug-*).

Table 6.4 is used to illustrate how quickly the number of basis functions increases as a result of increasing orbital flexibility. The same relationship can be observed in Table A1 of Appendix I, where the number of basis functions for a variety of basis sets is compared for each complex. Augmenting the basis set significantly raises the number of basis functions utilized in the calculation, but the greatest gains in the number of basis functions are obtained by including three ζ-functions. The *aug-cc-pVTZ* basis set actually contains more basis functions than the SBS or any other basis set, therefore it is the most computationally intensive of the series.

6.6. Relative Energies

In the four complexes investigated, the relative energy between Structures I and II was obtained, and this parameter provides a crude estimation for the barrier of rotation of the fluorinated methane subunit. In each complex, calculations confirmed a higher relative energy for Structure II relative to Structure I, and these relative energies (for each

basis set) are tabulated in Table 6.5. The relative energies obtained with different basis sets for any particular structure (e.g. Structure I of TFM–OCS) are then compared to one another graphically in Figure 6.16. A theoretical relative energy can only be obtained by comparing the energies obtained for two different structural configurations on the potential energy surface, which have been calculated at the same level of theory employing exactly the same basis sets (e.g. Structure I energy relative to Structure II energy using MP2/*cc-pVTZ*). Since the CCD calculations were only performed for the minimum energy configurations, they were not included in this plot. It should noted that, in Figure 6.16, a general trend in the relative energies can be observed which does give an indication of whether a particular complex might be expected to display internal rotation effects; i.e. the FM–OCS relative energies are all very small which may indicate a possibility for a low barrier internal rotation (as supported by experimental results[4]). Looking at how the calculations performed with regards to relative energies in Figure 6.16, a random distribution for these values is observed. The systematic addition of basis functions does not clearly improve the relative energies calculated by MP2.

Table 6.5: The relative energies (cm^{-1}) between Structures I and II calculated for different basis sets.

Level	TFM-OCS	DFM-OCS	FM-OCS	TFM-CO_2
MP2/*cc-pVDZ*	7	178	25	19
MP2/*cc-pVTZ*	79	119	4	61
MP2/*aug-cc-pVDZ*	117	115	23	93
MP2/*aug-cc-pVTZ*	78	109	12	49
MP2/SBS	90	76	0.5	75

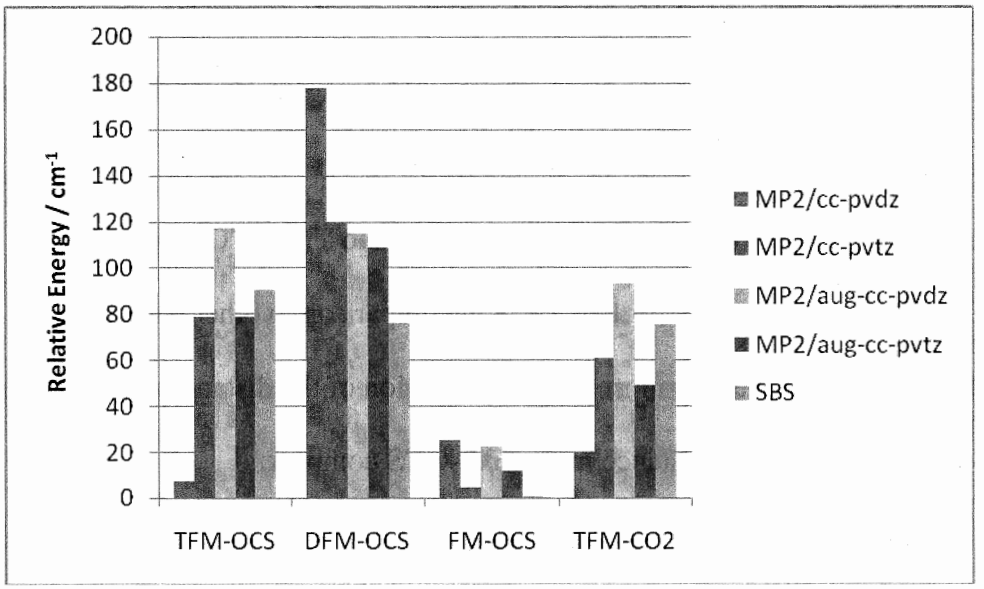

Figure 6.15: Comparison of the relative energies (in cm^{-1}) as a function of basis set for each respective complex.

The structural parameters can also be compared among the basis sets to determine whether an improvement is observed as orbital flexibility is increased. Tables A2 and A3, in Appendix I, contain the O···H intermolecular distances for Structures I and II respectively. Experimentally, the r_{OH} distance for Structure I of TFM–CO_2 is determined to be 2.83(2) Å, with calculated values varying between 2.65 Å and 2.78 Å. Interestingly, the CCD level of theory with a *cc-pVTZ* basis set provides the most precise value for this complex (see Figure 6.7), utilizing 121 less basis functions than the calculation of highest orbital description (MP2/*aug-cc-pVTZ*), but is performed at a higher level of theory. It also performs with the highest precision when calculating r_{OH} values for Structure I of TFM–OCS and DFM–OCS. Strangely, however, the r_{OH} value obtained with the CCD level of theory with a *cc- pVTZ* basis set provides the worst agreement in the FM–OCS complex in comparison to other basis sets. Similarly, Tables A4 and A5 in Appendix I, contain the C···C intermolecular distances for Structures I and

II respectively and show precision of predicted distances between the two carbon atoms for the varied levels of calculation and basis sets. Once again, the CCD level of theory with a *cc- pVTZ* basis set provides the most precise values in comparison to the experimental r_{CC} values of TFM–OCS, DFM–OCS, and TFM–CO_2, and the worst approximation of this distance for FM–OCS in comparison to other basis sets utilized. The SBS actually provides the most precise prediction of the distances between the two carbon atoms and the O···H distance in the FM–OCS complex.

The O– C···C and C···C–H intermolecular angles (represented by θ and ϕ respectively) have also been predicted at the same levels of theory and basis sets as the intermolecular distances. Note, in Figures 6.4 and 6.6, the second bond angle (ϕ) in the C_{2V} plane is a C···C–F angle and not a C···C–H angle as observed in all other structures. Tables A6 and A7 (in Appendix I) display all the O– C···C bond angles obtained for the various levels of calculation with the same basis sets as described above. Tables A8 and A9 (in Appendix I) contain predictions of either the C···C–H or C···C–F bond angles (ϕ). There is no obvious correlation between the number of basis functions and the experimentally determined angles, but all the calculations do show some agreement of the angles. The bond angles of floppy complexes are difficult to determine experimentally to within 1-2° due to low energy molecular vibrations, so fluctuations in the precision of bond angle predictions are expected.

The rotational constants of Structure I of the four complexes have been calculated and are displayed in Table A10 of Appendix I. Apparently, the CCD level of theory with a *cc- pVTZ* basis set is unsurpassed in its ability to calculate rotational constants. All calculated values fell within 2.5% of experimentally measured rotational constants,

except in one instance where the B rotational constant of FM–OCS was calculated with a 3.8% relative error. In several instances the predicted rotational constants had a 0.2-0.4% relative error, such as in the predicted value of A for TFM–CO_2. It was predicted to be 5.8027157 GHz and experimentally determined to be 5.8179605 (19) GHz, having a 0.26% relative error. Once again, this level of calculation (and corresponding basis set) do not give as precise a prediction of theoretical structural parameters for FM–OCS (i.e. bond lengths and angles), however, the predicted rotational constants were more precise than any other level or basis set. It is likely that the Coupled Cluster (CCD) level of theory was unable to correctly approximate the structure of FM–OCS due to complex motions experimentally observed in this complex.

6.7. Conclusions

The structures of four weakly bound complexes have been computed with *ab initio* techniques. Studies involved a systematic improvement of basis sets in order to determine whether the theoretical structures (i.e. Structures I and II of each complex) could be closely approximated to the experimentally determined structures. All the calculations were performed at relatively high levels of theory that include electron correlation, namely with MP2 and CCD. Structure I was computed to be the structural conformation of lowest energy and corresponds to the experimental structure for any given complex. The four minimum energy configurations are all similar in structure, displaying an approximate antiparallel interaction of the monomer dipole moments, causing weak complexation. A linear correlation was discovered between the monomer dipole moments of the fluorinated subunit and the center of mass separation between complexes containing OCS. An increase in the dipole moment for a given fluorinated

methane subunit corresponds to a reduction in the distance between the monomer centers of mass. To a first approximation, the decrease in the center of mass separation corresponds to an increase of binding strength, and this result supports the fact that very weak dipole-dipole interactions are largely responsible for the dimerization of these complexes. Calculated values for the intermolecular bond angles and bond distances were compared to previously optimized structures which were generated using MP2 theory and the Standard Basis Set (6-311++G(2d,2p) or SBS), and displayed relatively good agreement for all models utilized. It was determined that the CCD level of theory with a *cc- pVTZ* basis set performs better than the MP2 level and using a basis set (*cc-pVTZ*) that is only moderately larger than the SBS (21-25 more basis functions than the SBS depending on the molecule). It could be argued that this level of theory should be utilized in future calculations because it is more precise in determining theoretical structural parameters; however, it is accompanied by an increase in required computational resources. The predicted bond angles showed a wider scatter but given the difficulty of determining these parameters accurately in floppy complexes makes it more difficult to judge the performance of these calculations.

Improving the level of correlated models to higher levels of theory, such as higher coupled cluster methods or configuration interaction models, could be employed to expand on this study. New and different functionals could be implemented into density functional theory calculations. DFT is usually less computationally intensive than correlated models and may still provide precise parameters, so this avenue should still be explored. Anharmonic frequency calculations should also improve the rotational constants, allowing calculation of the ground vibrational state rotational constants rather

than the equilibrium rotational constants (that is, we could obtain A_0, B_0, and C_0 rather than A_e, B_e, and C_e respectively). Finally it would also be useful to calculate Structure II for each complex at the CCD / *cc-pVTZ* level and basis set in order to obtain the CCD relative energies.

References

[1] Serafin, M.M.; Peebles, S.A., (in preparation)

[2] Serafin, M.M.; Peebles, S.A. *J. Phys. Chem. A*. **2008**,*112*, 1473.

[3] Serafin, M.M.; Peebles, S.A., *J. Phys. Chem. A.* **2006**, *110*, 11938.

[4] Serafin, M.M.; Peebles, R.A., Peebles, S.A. *J. Mol. Spectrosc.*, (submitted)

[5] J. Foresman, Æ. Frisch, *Exploring Chemistry with Electronic Structure Methods*, 2nd ed. Gaussian Inc. Pittsburgh, PA, **1996**, pp. 9-10, 98-102.

[6] Nelson, R.D.Jr., Lide, D.R.Jr., Maryott, A.A. *NSRDS-NBS.***1967**, *10*, 49.

[7] T.H. Dunning, Jr. *J. Chem. Phys.* **1989**, *90*, 1007.

[8] EMSL basis set order form, *located at*; http://www.emsl.pnl.gov/forms/basisform.html.

Appendix I

Table A1: Number of basis functions combined in various basis sets to approximate the wavefunction of each system. The total numbers of basis functions in calculations performed at the same level with the same basis sets are equal for Structures I and II of a given complex. This is due to the fact that the number of atoms and types of atoms do not vary between Structure I to Structure II. Restricted MP2 denoted by RMP2.

Level / Basis Set	TFM-OCS	DFM-OCS	FM-OCS	TFM-CO_2
MP2/*cc- pVTZ*	107	98	89	103
MP2/*cc- pVTZ*	228	212	196	224
MP2/*aug-cc-pVDZ*	174	160	146	170
MP2/*aug-cc-pVTZ*	349	326	303	345
MP2/6-311++G(2d,2p)	207	190	173	199
CCD/*cc-pVTZ* [a)]	228	212	196	224

[a)] CCD only performed for Structure I of each complex

Table A2: Theoretical H···O separation in Angstroms obtained from various computational methods employed for minimum energy configurations compared to experimental values (Structure I of each system).

Level / Basis Set	TFM-OCS	DFM-OCS	FM-OCS	TFM-CO_2
MP2/*cc- pVDZ*	2.727	2.758	2.634	2.766
MP2/*cc- pVTZ*	2.677	2.729	2.655	2.701
MP2/*aug-cc-pVDZ*	2.608	2.630	2.624	2.653
MP2/*aug-cc-pVTZ*	2.623	2.649	2.606	2.695
MP2/6-311++G(2d,2p)	2.625	2.651	2.653	2.699
CCD/*cc-pVTZ*	2.743	2.803	2.747	2.775
Experimental	2.90(5)	2.88(3)	2.65(6)	2.83(5)

Table A3: Theoretical H···O separation in Angstroms obtained from various computational methods employed for next highest energy configurations compared to experimental values (Structure II of each system).

Level / Basis Set	TFM-OCS	DFM-OCS	FM-OCS	TFM-CO_2
MP2/*cc- pVDZ*	2.558	2.901	2.969	2.547
MP2/*cc- pVTZ*	2.567	2.860	2.997	2.594
MP2/*aug-cc-pVDZ*	2.493	2.868	2.972	2.524
MP2/*aug-cc-pVTZ*	2.509	2.858	2.957	2.565
MP2/6-311++G(2d,2p)	2.511	2.858	2.972	2.571
Experimental	2.90(5)	2.88(3)	2.65(6)	2.83(5)

Table A4: Theoretical C···C separation in Angstroms obtained from various computational methods employed for minimum energy configurations compared to experimental values (Structure I of each system).

Level / Basis Set	TFM-OCS	DFM-OCS	FM-OCS	TFM-CO_2
MP2/*cc- pVDZ*	3.514	3.426	3.698	3.379
MP2/*cc- pVTZ*	3.520	3.471	3.750	3.446
MP2/*aug-cc-pVDZ*	3.463	3.442	3.737	3.381
MP2/*aug-cc-pVTZ*	3.477	3.444	3.708	3.443
MP2/6-311++G(2d,2p)	3.478	3.450	3.755	3.445
CCD/*cc-pVTZ*	3.633	3.560	3.826	3.525
Experimental	3.642 (17)	3.58(2)	3.75(3)	3.57(5)

Table A5: Theoretical C···C separation in Angstroms obtained from various computational methods employed for next highest energy configurations compared to experimental values (Structure II of each system).

Level / Basis Set	TFM-OCS	DFM-OCS	FM-OCS	TFM-CO_2
MP2/*cc- pVDZ*	3.764	3.617	3.604	3.626
MP2/*cc- pVTZ*	3.805	3.611	3.640	3.710
MP2/*aug-cc-pVDZ*	3.739	3.593	3.630	3.635
MP2/*aug-cc-pVTZ*	3.751	3.574	3.605	3.681
MP2/6-311++G(2d,2p)	3.753	3.610	3.636	3.684
Experimental	3.642 (17)	3.58(2)	3.75(3)	3.57(5)

Table A6: Theoretical C···C–O bond angle (θ in °) obtained from various computational methods employed for minimum energy configurations compared to experimental values (Structure I of each system).

Level	TFM-OCS	DFM-OCS	FM-OCS	TFM-CO_2
MP2/*cc- pVDZ*	60.1	64.3	61.2	66.4
MP2/*cc- pVTZ*	61.3	65.0	61.3	63.5
MP2/*aug-cc-pVDZ*	60.6	64.1	61.4	64.9
MP2/*aug-cc-pVTZ*	60.9	64.1	61.3	63.4
MP2/6-311++G(2d,2p)	60.9	63.8	61.3	63.3
CCD/*cc-pVTZ*	57.4	62.9	60.6	63.0
Experimental	60.2 (1)	64.7(6)	61(2)	62(3)

Table A7: Theoretical C···C–O bond angle (θ in °) obtained from various computational methods employed for next highest energy configurations compared to experimental values (Structure II of each system).

Level	TFM-OCS	DFM-OCS	FM-OCS	TFM-CO_2
MP2/*cc- pVDZ*	56.2	54.5	57.7	62.0
MP2/*cc- pVTZ*	56.1	53.7	58.7	60.6
MP2/*aug-cc-pVDZ*	56.1	54.7	58.4	61.4
MP2/*aug-cc-pVTZ*	55.9	55.2	58.6	60.4
MP2/6-311++G(2d,2p)	55.8	53.4	58.0	60.4
Experimental	60.2(1)	64.7(6)	61(2)	62 (3)

Table A8: Theoretical C···C–H bond angle (ϕ in °) obtained from various computational methods employed for minimum energy configurations compared to experimental values (Structure I of each system).

Level	TFM-OCS	DFM-OCS	FM-OCS[a)]	TFM-CO_2
MP2/*cc- pVDZ*	79.4	81.8	63.1	82.5
MP2/*cc- pVTZ*	75.0	76.9	60.5	78.2
MP2/*aug-cc-pVDZ*	75.4	74.3	60.0	78.1
MP2/*aug-cc-pVTZ*	74.8	74.8	60.1	78.1
MP2/6-311++G(2d,2p)	74.8	74.9	60.1	78.2
CCD/*aug-cc-pvdz*	75.6	77.7	61.8	78.1
Experimental	81.1(26)	79(2)	50(2)	80(7)

[a)] The angle described is the C···C–F bond angle.

Table A9: Theoretical C···C–H (revised as C···C–F for DFM–OCS and FM–OCS) bond angle (ϕ in °) obtained from various computational methods employed for next highest energy configurations compared to experimental values (Structure II of each system).

Level	TFM-OCS	DFM-OCS[a)]	FM-OCS[b)]	TFM-CO_2
MP2/*cc- pVDZ*	59.8	54.8	50.7	61.3
MP2/*cc- pVTZ*	57.3	58.3	53.0	60.0
MP2/*aug-cc-pVDZ*	57.6	58.0	52.9	60.1
MP2/*aug-cc-pVTZ*	57.3	57.9	53.2	60.3
MP2/6-311++G(2d,2p)	57.3	58.5	53.4	60.3
Experimental	81.1(26)	79(2)	50(2)	80(7)

[a)] The angle is the C···C–F bond angle in DFM–OCS. [b)] The bond angle is the C···C–F bond angle in FM–OCS.

Table 10: Theoretical rotational constants in GHz obtained from various computational methods employed for minimum energy configurations compared to experimental results (Structure I).

Level and Rot. Const. in GHz	TFM-OCS	DFM-OCS	FM-OCS	TFM-CO_2
RMP2/*cc-pVDZ*				
A	4.6771854	4.5349928	7.2580036	5.6082304
B	0.8506461	1.3608269	1.6989436	1.220921
C	0.8253361	1.2958795	1.3890365	1.219933
RMP2/*cc-pVTZ*				
A	4.6396901	4.4704478	7.1383515	5.7044784
B	0.8492375	1.3351858	1.6584172	1.1743148
C	0.821712	1.2645645	1.3572895	1.1733427
RMP2/*aug-cc-pVDZ*				
A	4.5744287	4.3885211	7.0020012	5.5133378
B	0.861573	1.3355349	1.6731677	1.2025793
C	0.8341598	1.2660267	1.3624371	1.2010955
RMP2/*aug-cc-pVTZ*				
A	4.644545875	4.481572602	7.121861278	5.689350604
B	0.863061784	1.340452417	1.69923967	1.174610977
C	0.83503423	1.270853095	1.383948707	1.173769203
MP2/6-311++G(2d,2p)				
A	4.6374691	4.4803482	7.1218002	5.6836091
B	0.8617958	1.3325485	1.6609692	1.1737135
C	0.8341352	1.265831	1.35841	1.172213
CCD/*cc-pVTZ*				
A	4.9026055	4.6199583	7.3481808	5.8027157
B	0.7956939	1.2624793	1.5929028	1.1375571
C	0.7773895	1.2067748	1.3200512	1.135122
Experimental				
A	4.7457148 (25)	4.5056740 (27)	7.3225753 (15)	5.8179605 (19)
B	0.8139228 (27)	1.2770710 (27)	1.6556314 (34)	1.1196036 (3)
C	0.7909234 (27)	1.2120064 (27)	1.3487426 (33)	1.1119296 (4)